ISSN 1810-648X

ACADEMY OF SCIENCES
OF MOLDOVA

PHYSICAL SOCIETY OF MOLDOVA

STATE UNIVERSITY OF MOLDOVA

Moldavian Journal of the Physical Sciences

Issue dedicated to the memory of academician Sergiu Radautsan
(1926-1998)

Chisinau
2016

Volume 15
No. 3-4

Scientific journal **Moldavian Journal of the Physical Sciences** includes original scientific articles, communications and reviews concerning various problems of modern physics. The journal is published in English, its periodicity is 4 numbers a year, with circulation of 200 copies.

web: http://sfm.asm.md/moldphys/

GUIDELINES FOR AUTHORS

The "Moldavian Journal of Physical Sciences" appears quarterly and publishes in English papers referring to original scientific research in physics and related fields, including applications in electronics and technology, material engineering and device physics. A review paper for every issue is planned and short communications with hot news are encouraged.

Papers must be prefaced by a brief abstract in English up to 100 words. Single space of the rows in the manuscript is required.

Authors are invited to send two printed copies of their papers, as well as an electronic record on a $3^{1/4}$ inches diskette, or by e-mail, in English. The articles will be edited by using WORD for Windows. Chapters must be numbered by using Arabic figures, as follows:

3. Experimental results.
3.1. Results analysis.
3.2. Methods of calculus.

Formulae must be written very clearly and easy-to-read. Do not use non-explained abbreviations. Illustrations and diagrams must be realized on computer drafts (on images). All graphic and text objects must be of very good quality and easy to read. Figures included in the text are preferable.

Reference citations will be presented as follows: author's forename initial and last name, journal name, volume, page number, year (in parentheses), for example: F.A. Moldovan, S.P. Russu, Phys. Rev. Let. 85, 357, (2000). Complete title, publisher, city and year will be written for book's author's name and forename initial, for example: M. Teodorescu, Cooperation in science and technology with Eastern and European countries, Editura Tehnica, Bucuresti, vol. 1, 1992. References into the text will be made within square brackets, for example [7]; reference citation numbers must be made successively, as they appear into the text.

Manuscripts of regular papers should be limited up to 10 pages and will be signed by authors; they also must be marked "Ready to print". Reviews are limited up to 20 pages. Maximum 4 pages are admitted for short communications. One full page of the journal (size A4) contains 54 rows with 95 characters/row; font size - 12. Page set up: top, left, right – 2,5; bottom – 3,5 cm. The very manuscript which is marked "Ready to print" will be published within 6 months from sending.

The submitted papers must be reviewed, if possible, by two independent reviewers. The papers must contain original work and have not submitted for publication to any other journal. The papers which have been published previously, as well those accepted to be published in other reviews, will be not be admitted by Editorial Board; the authors have to mention this situation.

Proofs will be sent to authors for checking. Corrections must be restricted to errors since modifications to the text may be charged to the author. The publishers reserve the right to adapt the presentation of an article to conform to our style. After their publishing in our journal, the manuscripts and corresponding illustrations become the property of Editorial Board and will not be returned to the authors. The same for the papers, which have not been admitted for publication. The publishing in our journal is made free of charge.

The papers sent for publishing are considered not secret. The authors only are responsible for this in front of their own institutes or employers. Authors have to mention their complete address and telephone, fax number and e-mail.

Papers from around the world can be sent to be published to the following address:

Department of Mathematical, Physical and Technical Sciences, 5 Academy St., MD 2028 Kishinev, the Republic of Moldova, tel. (+37322) 72-71-57, 73-81-66; E-mail: kantser@nano.asm.md, E-mail of responsible secretary: sofiadonu@yahoo.com

THE NEUTRON DIFFRACTION STUDIES OF A CRYSTAL STRUCTURE OF $NaFe(W_xMo_{1-x}O_4)_2$ (x = 0.5; 0.75) AT LOW TEMPERATURE

V.M. Thanh[1, 2, a], D.P. Kozlenko[1], D. Sangaa[3], S.E. Kichanov[1], E.V. Lukin[1], L.H. Khiem[2], L.Nyam-Ochir[4], O. Gerelmaa[4], B.N. Savenko[1]

[1]Frank Laboratory of Neutron Physics, JINR, 141980 Dubna, Moscow Reg., Russia
[2]Institute of Physics, Vietnam Academy of Science and Technology, 100000 Hanoi, Vietnam
[a]Joint Institute for Nuclear Research, FLNP, 141980 Dubna, Moscow reg., Russia
[3]Institute of Physics and Technology, MAS, Ulaanbaatar - 13330, Mongolia
[4]Department of Physics, National University of Mongolia, Ulaanbaatar -14201, Mongolia
E-mail: vmthanh@iop.vast.ac.vn

(Received November 9, 2016)

Abstract

The crystal structure of the double tungstates $NaFe(W_{0.5}Mo_{0.5}O_4)_2$ and $NaFe(W_{0.75}Mo_{0.25}O_4)_2$ has been studied by means of a neutron diffraction method in temperature range 5-24 K. No evidence for long range magnetic order was found in both compounds down to 5 K. The unit cell parameters, atomic coordinates, bond lengths and angles for the studied compounds have been obtained. An absence of magnetic ordering is explained by reduction of super-exchange coupling due to a disordering of a Fe-O-O-Fe trapeze-like crystal unit.

1. Introduction

Materials based on double tungstates family are most promising ones for laser diode industry and luminescent phosphors, as well as widely studied due to their distinguished physical properties [1 – 6]. The double tungstates compounds with general formula $MX^{3+}(WO_4)_2$ (where M – alkali earth metal and X^{3+} – triple valence ions) depending on the M and X elements exhibit structural polymorphism, rich magnetic and structural phase diagrams, complex coexisting of exchange, dipole–dipole and Jahn–Teller (electron–phonon) interactions and, as result, the unusual magnetic ordering [7]. The tens of different structural types of $M^+X^{3+}(AO_4)_2$ compounds, where M^+ = Li-Cs, Ag and Tl^+, X^{3+} = lanthanides, Y, Bi, In, Sc, Ga, Fe, Cr and A = Mo or W, were found [8]. The crystal structures of the most types have been determined, but the structural details of many compounds remain unknown [9].

Among the double tungstates, the compound $NaFe(WO_4)_2$ crystallizes in the monoclinic structure with P2/c space group [10]. In this structure, the crystal layers of Na–O polyhedra alternate with zigzag-chains of FeO_6 and WO_4 octahedra [11, 12]. Due to those structural features, the $NaFe(WO_4)_2$ materials are suitable model compounds with complex magnetic interactions based on double super-exchange couplings Fe–O–O–Fe [13]. The magnetization measurements and neutron diffraction studies reveal antiferromagnetic ordering with a commensurate propagation vector k = [½, ½, ½], where magnetic moments of iron ions oriented along the *a*-axis. It was known, the magnetic interactions between Fe^{3+} ions are realized through oxygens and very sensitive to changes in the oxygen crystallographic environment. As an

example, a substitution of Fe^{3+} ions to chromium ones leads to suppression of magnetic ordering in $NaFe_xCr_{1-x}(WO_4)_2$ compounds [10]. Another way to modify the magnetic interactions through Fe-O-O-Fe chains is doping inside of tungsten sublattice. The W^{6+} and Mo^{6+} ions have similar ionic radius and mutual substitution should not greatly effect on structural parameters of $NaFe(W_xMo_{1-x}O_4)_2$, but can vary an oxygen environment indirectly. In this work, the searching for expected magnetic phases of $NaFe(W_xMo_{1-x}O_4)_2$ for x = 0.5; 0.75 and detailed crystal structure studies by means of neutron diffraction at low temperature range 4 – 24 K have been performed.

2. Experimental

The samples of $NaFe(W_{0.5}Mo_{0.5}O_4)_2$ and $NaFe(W_{0.75}Mo_{0.25}O_4)_2$ were prepared from corresponding stoichiometric mixtures of Na_2WO_4, WO_3 , MoO_3, and Fe_2O_3 at temperature 800^oC for 48h, as described in detail in Ref. [10].

The crystal structure of $NaFe(W_xMo_{1-x}O_4)_2$ (x = 0.5; 0.75) compounds was investigated using a DN-6 neutron diffractometer [14] at the IBR-2 high-flux pulsed reactor (Frank Laboratory of Neutron Physics, JINR, Dubna, Russia). A sample with a volume about 5 mm^3 was placed inside a cryostat based on a closed-cycle refrigerator. The neutron powder diffraction data was collected at scattering angle of $2\theta = 90°$. The measurements were performed in the temperature range 5–24 K. The diffraction data for the crystal structure was analyzed by the Rietveld method using FullProf program [15].

3. Results and discussions

Neutron diffraction patterns of $NaFe(W_{0.5}Mo_{0.5}O_4)_2$ and $NaFe(W_{0.75}Mo_{0.25}O_4)_2$ measured at low temperatures are shown in Fig. 1. Both of the samples have the monoclinic structure of the P2/c symmetry. The obtained from neutron diffraction data structural parameters at temperature T = 4 K are a = 9.845(5), b = 5.691(2), c = 4.947(2) Å and $\beta = 90.6(2)^o$ for $NaFe(W_{0.5}Mo_{0.5}O_4)_2$; a = 9.878(1), b = 5.719(6), c = 4.956(7) Å and $\beta = 90.5(3)^o$ for $NaFe(W_{0.75}Mo_{0.25}O_4)_2$. These values are comparable well with previously obtained for $NaFe(WO_4)_2$ [10].

At temperature decreasing, there are no additional magnetic reflections or additional magnetic contribution to nuclear peaks. This fact indicates an absence of magnetic ordering in $NaFe(W_{0.5}Mo_{0.5}O_4)_2$ and $NaFe(W_{0.75}Mo_{0.25}O_4)_2$ down to 5 K.

In monoclinic structure of $NaFe(W_xMo_{1-x}O_4)_2$ (x = 0.5; 0.75) the atoms Na, Fe and W/Mo locate at octahedral oxygen coordination (Fig. 2). The atoms Na are surrounded by a group of atoms O_2 and O_3, which forms variable distances Na – O_{21}, Na – O_{22} and Na – O_3; while the atoms Fe, which are octahedrally coordinated with atoms O_1 and O_4, are characterized by bond lengths Fe – O_{11}, Fe – O_{12} and Fe – O_4. The atoms W/Mo consist of six different bonds: W/Mo – O_1, W/Mo – O_2, W/Mo – O_{31}, W/Mo – O_{32}, W/Mo – O_{41} and W/Mo – O_{42}. In this kind of structure, each W/MoO_6 octahedral shares the edges O_3 – O_4 with two other W/MoO_6 and forms zigzag-like chains, those repeated in the whole crystal structure. The NaO_6 and FeO_6 octahedra also have similar configuration of zigzag chains themselves and link with the W/MoO_6 chains by sharing corners of oxygen. The obtained from experimental data atomic coordinates for compounds $NaFe(W_xMo_{1-x}O_4)_2$ (x = 0.5; 0.75) are listed in Table 1. The calculated values of selected bonds lengths and angles are presented in Table 2. The super-exchange interactions are mediated

through a Fe – O – O – Fe chain and strongly depend on Fe-O-O angles, which also listed in Fig. 2.

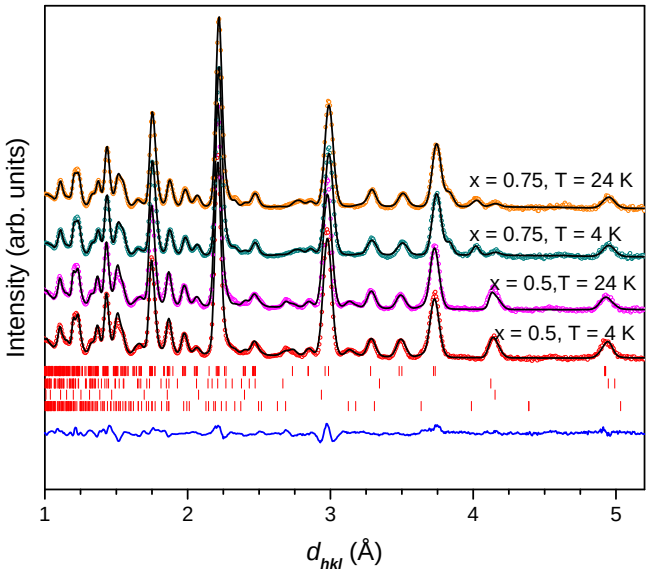

Fig 1. Neutron diffraction patterns at low temperatures of $NaFe(W_xMo_{1-x}O_4)_2$ (x = 0.5; 0.75). The experimental points and the calculated profiles by the Rietveld method are shown.

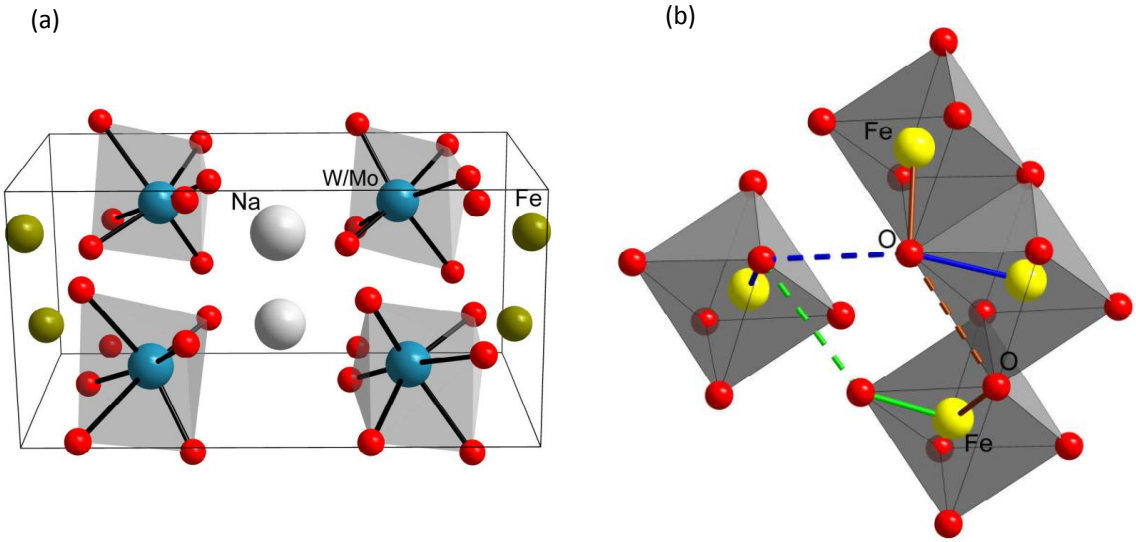

Fig 2. Schematic representation of the crystal structure of $NaFe(W_xMo_{1-x}O_4)_2$ (x = 0.5; 0.75) at low temperature (a) and the enlarged part of crystal structure with directions of super-super-exchange interactions (b).

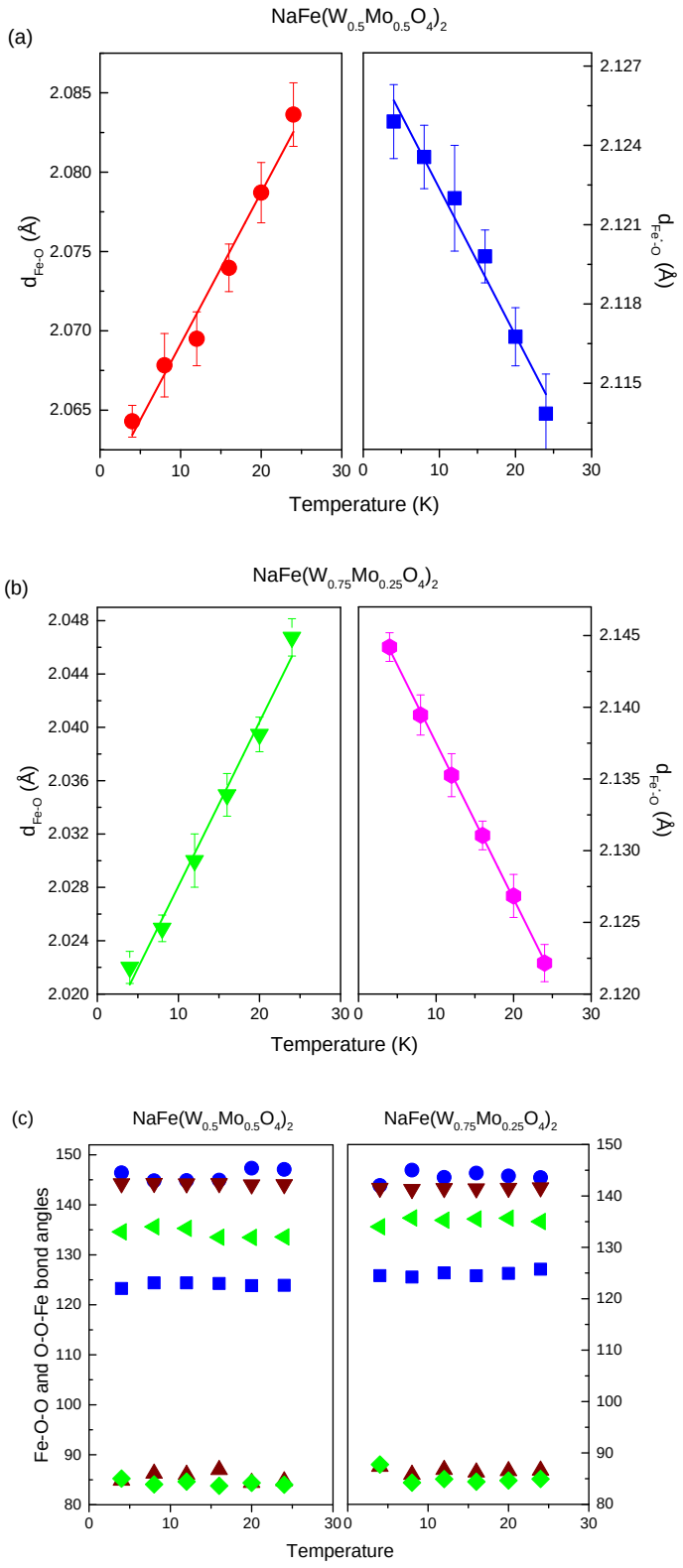

Fig 3. Temperature dependences of Fe – O bond lengths and the linear fit of experimental points of $NaFe(W_xMo_{1-x}O_4)_2$ (x = 0.5; 0.75) (a), (b). The temperature dependences of Fe – O – O and O – O – Fe bond angles (c), each kind of color dots in picture (c) provides a super-super-exchange interaction which has already showed in Fig. 2

The thermal expansion coefficient $\alpha = \frac{1}{V}\left(\frac{dV}{dT}\right)_p$ was calculated for both compounds. The obtained values are 1.23(8) × 10^{-6} K^{-1} for $NaFe(W_{0.5}Mo_{0.5}O_4)_2$ and 1.4(5) × 10^{-5} K^{-1} for $NaFe(W_{0.75}Mo_{0.25}O_4)_2$.

Table 1. Structural parameters of $NaFe(W_xMo_{1-x}O_4)_2$ (x = 0.5; 0.75) at low temperature 5 K. In the monoclinic phase with space group *P2/c* atomic positions are: Na – 2(f) (0.5, y, 0.25), Fe – 2(e) (0, y, 0.25), W/Mo – 4(g) (x, y, z) and for atoms O – 4(g) (x, y, z).

	$NaFe(W_{0.5}Mo_{0.5}O_4)_2$			$NaFe(W_{0.75}Mo_{0.25}O_4)_2$		
	x	*y*	*z*	*x*	*y*	*z*
Na	0.5	0.677(8)	0.25	0.5	0.692(9)	0.25
Fe	0	0.676(1)	0.25	0	0.666(5)	0.25
W/Mo	0.245(8)	0.205(6)	0.247(4)	0.239(1)	0.193(6)	0.250(7)
O_1	0.107(3)	0.621(4)	0.605(2)	0.112(4)	0.621(4)	0.589(3)
O_2	0.357(6)	0.383(5)	0.382(1)	0.356(6)	0.385(5)	0.368(1)
O_3	0.328(3)	0.081(3)	0.944(8)	0.327(5)	0.089(1)	0.950(4)
O_4	0.121(9)	0.131	0.583(1)	0.124(7)	0.143(4)	0.590(1)

Table 2. Bond lengths (Å) and bond angles (deg) for compounds $NaFe(W_xMo_{1-x}O_4)_2$ (x = 0.5; 0.75) at low temperature *T* = 5 K.

		x = 0.5	x = 0.75
Bond lengths of NaO_6 octahedral (Å)	$Na – O_{21}$	2.284(3)	2.336(6)
	$Na – O_{22}$	2.311(7)	2.395(1)
	$Na – O_3$	2.387(7)	2.340(3)
Bond lengths of FeO_6 octahedral (Å)	$Fe – O_{11}$	2.064(3)	2.022(1)
	$Fe – O_{12}$	2.124(9)	2.144(2)
	$Fe – O_4$	1.830(4)	1.830(1)
Bond lengths of WO_6/ MoO_6 octahedral (Å)	$W/Mo – O_1$	1.814(9)	1.817(8)
	$W/Mo – O_2$	1.633(8)	1.696(4)
	$W/Mo – O_{31}$	1.852(3)	1.834(3)
	$W/Mo – O_{32}$	2.065(4)	2.083(6)
	$W/Mo – O_{41}$	2.112(8)	2.055(3)
	$W/Mo – O_{42}$	2.406(2)	2.367(5)
Bond angles (^{o})	Fe – O – O	146.4(2)	142.1(1)
		144.2(7)	141.5(4)
		134.6(1)	134.1(2)
	O – O – Fe	123.2(6)	124.4(8)
		84.8(5)	87.3(2)
		85.2(3)	87.7(5)

The temperature dependences of Fe-O bonds and valence angles Fe-O-O and O-O-Fe are shown in Fig. 3. In complex magnetic interactions balance for both compounds $NaFe(W_xMo_{1-x}O_4)_2$ (x = 0.5; 0.75) the superexchange interactions Fe-O-Fe inside Fe-O chains are dominant, and intra-chains ones with the largest Fe–Fe distance are mediated by super-exchange Fe–O–O–Fe [16]. Recently, it was shown, that maximal super-exchange coupling via Fe–O–O–Fe is achieved when the structural angles Fe-O-O and O-O-Fe are close to each other [17]. The doping by Mo^{6+} ions leads to significant distortion of the Fe-O-O-Fe trapeze and, consequently, the weak interlayer super-exchange interaction is greatly reduced. Besides the

thermal effect, the heating provokes an increase in the disorder degree, which promotes additional destabilization of the long-range three-dimensional magnetic order [17]. However, one cannot exclude that magnetic ordering can be formed at temperature less than 5 K.

4. Conclusion

The detailed studies of crystal structure of the double tungstates $NaFe(W_{0.5}Mo_{0.5}O_4)_2$ and $NaFe(W_{0.75}Mo_{0.25}O_4)_2$ have been performed by means of a neutron diffraction method in temperature range 5-24 K. The long-range magnetic ordering is not detected in both compounds. This fact can be explained by the reduction of weak Fe-O-O-Fe interaction due a structural distortion of corresponding structural units.

Acknowledgements. The authors acknowledge useful discussions with Dr. S.E. Kichanov and Dr. N.T. Dang (JINR, Dubna, Russia), the authors also thank Mr. A.V. Rutkauskas for supporting of experimental setting.

References

[1] Z. L. Wang, H. B. Liang, L. Y. Zhou, H. Wu, M.L. Gong, Q. Su, Chem. Phys. Lett. 412, 313, (2005).
[2] J. G. Wang, X. P. Jing, C. H. Yan, J. H. Lin, F. H. Liao, J. Lumin. 121, 57, (2006).
[3] C. H. Chiu, M. F. Wang, C. S. Lee, T. M. Chen, J. Solid State Chem. 180, 619, (2007).
[4] C. H. Chiu, C. H. Liu, S. B. Huang, T. M. Chen, J. Electrchem. Soc. 154, j181 (2007).
[5] K. S. Hwang, S. Hwangbo, J. T. Kin, Ceram. Int. 35, 2517, (2009).
[6] X. H. He, M. Y. Guan, J. H. Sun, N. Liang, T.M. Shang, J. Mater. Sci. 45, 118, (2010).
[7] M. D. Kaplan and B. G. Vekhter 1995 Cooperative Phenomena in Jahn–Teller Crystals (New York: Plenum) Gehring G A and Gehring K A Rep. Prog. Phys. 38 1, 1974.
[8] P. V. Klevtsov, R. F. Klevtsova, Zh. Strukt. Khimi 18, 419, (1977).
[9] J. M. Postema et al. / Journal of Solid State Chemistry 184, 2004, (2011).
[10] L. Nyam-Ochir, H. Ehrenberg, A. Buchsteiner, A. Senyshyn, H. Fuess, D. Sangaa, Journal of Magnetism and Magnetic Materials 320, 3251, (2008).
[11] P. V. Klevtsov, R. F. Klevtsova, J. Solid State Chem. 2, 278, (1970).
[12] R. F. Klevtsova, N. V. Belov, Sov. Phys.—Crystallogr. 15 (1), 32, (1970).
[13] H. Ehrenberg, K. G. Bramnik, E. Muessig, T. Buhrmester, H. Weitzel, C. Ritter, J. Magn. Magn. Mater. 261, 353, (2003).
[14] B. N. Savenko, D. P. Kozlenko, A. V. Belushkin, E. V. Lukin, S. E. Kichanov, E. S. Kichanov, E. S. Kuz'min, A. P. Bulkin, and A. P. Sirotin, in Proceedings of the XXII International Workshop on Neutron Scattering in Condensed Matter Investigations (NSCMI-2012), Gatchina, Leningrad oblast, October 15–20, 184, 2012.
[15] J. Rodriguez-Carvajal, Physica B (Amsterdam) 192, 55, (1993).
[16] Hyun Woo Bae and Hyun-Joo Koo, Bull. Korean Chem. Soc.Vol. 29, No. 1, (2008).
[17] Y. S. Hou, H. J. Xiang and X. G. Gong, Scientific Reports 5:13159, (2015) DOi: 10.1038/srep13159.

SYNTHESIS, CRYSTAL STRUCTURE, AND MAGNETIC PROPERTIES OF $MnCr_2S_4$ SPINEL

L. Prodan

Institute of Applied Physics, Academy of Sciences of Moldova, Chisinau, MD-2028
Republic of Moldova
**E-mail: lilian.prodan@gmail.com*

(Received October 17, 2016)

Abstract

A detailed study of the preparation of poly and single crystals of the $MnCr_2S_4$ ternary spinel and their structural and magnetic characterisation are reported. X-ray diffraction data for the polycrystals show a nearly stoichiometric chemical composition and a normal spinel structure of the main phase with an additional reflection (1%) of the minor phase MnS. From the temperature dependence of susceptibility measured in field-cooled (FC) and zero-field cooled (ZFC) sequences, the Curie temperature of T_C = 65 K is determined; it coresponds to a transition from the paramagnetic to ferrimagnetically ordered state. The second magnetic transition is detected at T_{YK} = 5 K; it coresponds to a transition from a coliniar to triangular spin configuration of the Yafet–Kittel type.

1. Introduction

Magnetic semiconductor compounds with general formula AB_2X_4 have attracted much attention of scientific community due to a number of new physical phenomena, such as multiferroicity [1, 2] and colossal magnetoresistance [3], which present high interest from both the fundamental and applied point of view. A particular case represents the $MnCr_2S_4$ ternary magnetic compound which crystallizes in a spinel structure with *Fd-3m* cubic symmetry. In this structure, the *A*-site cations (Mn^{2+}) occupy 1/8 of the tetrahedral positions, the *B*-site cations (Cr^{3+}) occupy ½ of the octahedral positions, and anions X (S^{2-}) form a compact cubic packing. It was previously reported for polycrystalline samples that, below 5 K, the ferrimagnetic $MnCr_2S_4$ spinel has the magnetic structure of the Yafet–Kittel (YK) type due to *AA* antiferromagnetic interactions [4, 5]. Above 5 K up to the Curie temperature, which varies from 66 to 80 K for polycrystals prepared by different authors, the magnetic structure is of the Néel-type due to strong ferromagnetic *BB* interactions [5–7].

In this paper, the results of preparation of polycrystalline and single-crystal samples of $MnCr_2S_4$ by the conventional solid state method and chemical transport reactions, respectively, are reported. A detailed structural and magnetic study of the samples is presented.

2. Experimental

Using the conventional solid state method of synthesis in evacuated quartz ampoules, polycrystalline samples of the $MnCr_2S_4$ ternary compound were prepared. High-purity metals Mn

and Cr (99.99%) and elemental S (99.999%) were used. To provide a full chemical reaction and obtain a ternary phase, three consecutive sintering cycles were required. After the first cycle, the samples were powdered, homogenized, pressed into pellets for a better diffusion, and annealed at 900°C. Single crystals were prepared by chemical transport reactions in evacuated quarts ampoules at a source temperature of about 1000°C using a polycrystalline material obtained as described above. Chromium chloride was used as a source of the transport agent (Cl). X-ray powder diffraction analysis of crashed polycrystalline pellets and single crystals was performed at room temperature. A STADI-P (STOE&CIE) diffractometer with CuK_α monochromatic radiation was used. A Quantum Design MPMS 5 SQUID magnetometer was used to study the magnetic properties of the $MnCr_2S_4$ compound in a temperature range of 2–400 K and magnetic fields of up to 50 kOe.

3. Results and discussion

X-ray diffraction of the polycrystalline $MnCr_2S_4$ samples revealed a nearly single-phase ternary compound with an additional reflection of the minor phase of MnS of about 1% (see Fig. 1). X-ray data were fitted by the Rietveld refinement method using FULLPROF program [8].

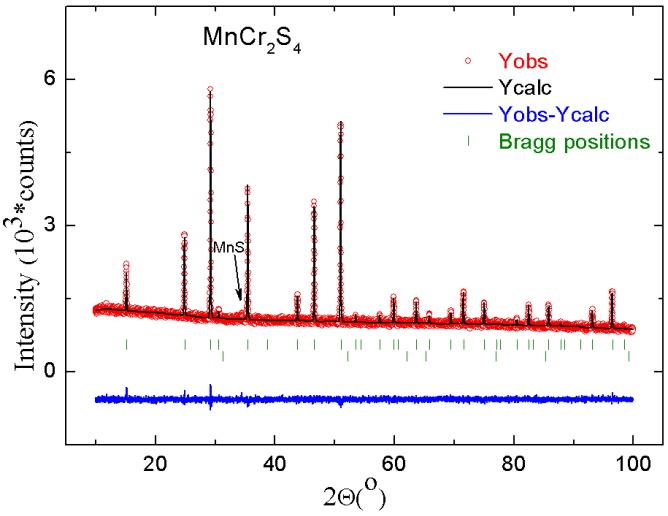

Fig. 1. X-ray diffraction profiles of the $MnCr_2S_4$ polycrystalline sample. The measured intensities (open circles) are compared with the calculated profile using Rietveld refinement (solid line). Bragg positions of the normal cubic spinel structure are indicated by vertical bars; the difference pattern is shown by the lower thin solid line.

Figure 2 shows the temperature dependence of magnetic susceptibility $\chi(T)$ for (a) the polycrystalline and (b) single-crystal $MnCr_2S_4$ samples measured after cooling in a magnetic field (FC) of 100 Oe and after cooling in a zero magnetic field (ZFC). For the single crystal, the field was applied in the <111> direction. For both samples, a strong step-like increase in magnetizations below 65 K was observed. This behavior corresponds to a transition from the paramagnetic to ferrimagnetically ordered state

For the polycrystalline sample, a splitting of the FC–ZFC susceptibility curves just below T_C was observed; the effect is related to the magnetic domain behavior. At low temperatures, these dependences revealed a second magnetic transition, which occurs at T_{YK} = 5 K.

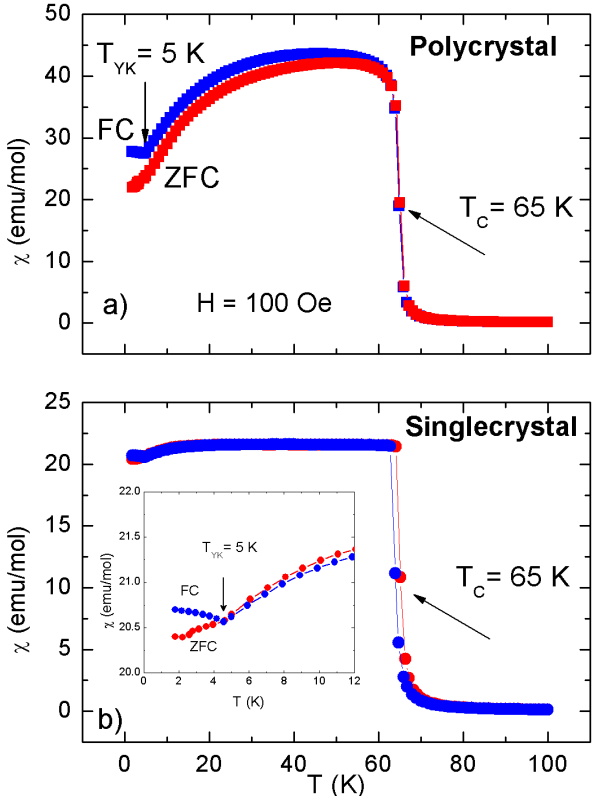

Fig. 2. Temperature dependence of magnetic susceptibility $\chi(T)$ for (a) the polycrystalline and (b) single-crystal $MnCr_2S_4$samples measured according to the FC and ZFC sequences.

It was previously reported for polycrystalline samples [5, 6] that this behavior is attributed to a transition from the collinear Néel spin configuration to the triangular YK-type configuration. For temperatures T above 5 K, the slope of the $\chi(T)$ curve was suggested to be caused by a change in the value of moments of the Mn^{2+} and Cr^{3+} ions with H in the collinear structure, while for T below T_{YK}, the slope of the $\chi(T)$ curve is caused by a change in the canting angle between two magnetic sublattices (Mn and Cr) in the external magnetic field [5].

Figure 3 presents the magnetic field dependences of magnetization $M(H)$ for the single-crystal $MnCr_2S_4$ sample measured in a low-temperature range (2–20 K). These data show the absence of the saturation of magnetization in high magnetic fields. This behavior in the YK phase can be attributed to a decrease in the angle between the Mn and Cr spins. Above the YK transition, an increase in the net moment might be attributed to the rotation of the Mn moments by the field. In addition, an increase in the net magnetization (from 1.29 to 2.00 μ_B per formula unit) with increasing temperature indicates a decrease in the angle between the Mn spins. It was found that for, the single-crystal sample below T_{YK}, the net magnetization remain almost constant and independent on temperature. From the $M(H)$ dependence for the polycrystalline $MnCr_2S_4$ sample measured at 2 K, the net magnetization value (1.15 μ_B) was determined.

Figure 4 shows the temperature dependence of the reciprocal of magnetic susceptibility *1/χ(T)* for the single-crystal sample measured in a magnetic field of 10 kOe. For the polycrystalline sample, a nearly similar behavior was observed. From these dependences, using the Curie–Weiss (CW) fit at high temperatures (in a range of 300–400 K), the CW temperature of Θ_{CW} = +23.8 K for the polycrystalline sample and Θ_{CW} = +12 K for the single-crystal sample was determined.

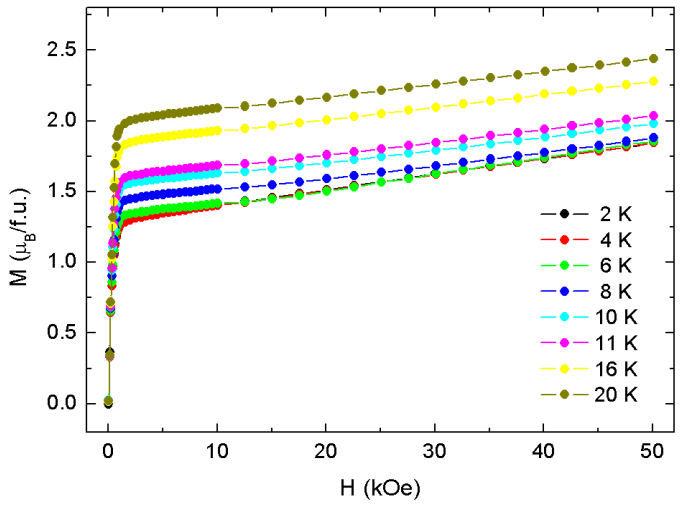

Fig. 3. Magnetic-field dependences of magnetization *M(H)* for single-crystal $MnCr_2S_4$ measured at the different temperatures.

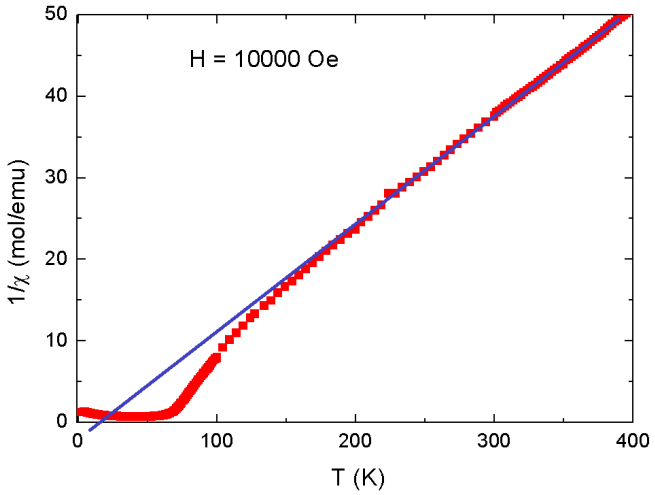

Fig. 4. Temperature dependence of the reciprocal of magnetic susceptibility *1/χ(T)* for single-crystal $MnCr_2S_4$ measured in a magnetic field of 10 kOe.

These values indicate the dominance of the ferromagnetic interactions; however, the low Θ_{CW} value suggests bond frustration in this compound related to a strong competition of the ferromagnetic and antiferromagnetic interactions. From the CW fit to the experimental data, the CW constant of C_m = 6.8 for the polycrystalline sample and C_m = 7.7 for the single-crystal

sample was determined. The C_m value for the single-crystal sample is in good agreement with the theoretical single-ion value of $C_m = 8.119$ for Mn^{2+} and two Cr^{3+} ions, while the C_m value for the polycrystal is significantly lower. This discrepancy between the experimental data and the theoretical values of C_m can be attributed either to the deviation of the states of the Mn^{2+} and Cr^{3+} ions from their single-ion values or, more probably, to the departure from the real paramagnetic temperature range. The measurements of susceptibility above 400 K can clarify the cause of the observed reduced C_m values.

4. Conclusions

To summarize, polycrystalline and single-crystal samples of ternary $MnCr_2S_4$ have been prepared. X-ray powder diffration data show a normal spinel structure and a nearly stoichiometric chemical composition for the main phase and an additional reflection of the minor phase of MnS (about 1%). From the temperature dependence of susceptibility for both samples measured in the FC and ZFC sequences, the Curie temperature of $T_C = 65$ K has been determined; it coresponds to a transition from the paramagnetic to collinear ferrimagnetic state. The second magnetic transition has been detected at $T_{YK} = 5$ K; it coresponds to a transition from the coliniar Néel spin configuration to a triangular YK structure. A positive value of CW temperature Θ_{CW} indicates the dominance of ferromagnetic interactions; however, a low Θ_{CW} value suggests bond frustration in the $MnCr_2S_4$ compound.

Acknowledgments. The author acknowledges the support of Dr. hab. V. Tsurkan and enlightening discussions with Dr. I. Filippova and Dr. V. Felea. The support by Institutional Project 15.817.02.06F and Young research project 16.80012.02.03F is acknowledged.

References

[1] J. Hemberger et al., Nature (London) 434, 364, (2005).
[2] Y. Yamasaki et al., Phys. Rev. Lett. 96, 207204, (2006).
[3] A. P. Ramirez et al., Nature (London) 386, 156, (1997).
[4] Y. Yafet and C. Kittel, Phys. Rev. 87, 290, (1952).
[5] F. K. Lotgering, J. Phys. Chem. Solids 29, 2193, (1968).
[6] N. Menyuk, K. Dwight, and A. Wold, J. Appl. Phys. 36, 1088, (1965).
[7] L. Darcy, P. K. Baltzer, and E. Lopatin, Appl. Phys. 39, 898, (1968).
[8] Rodriguez-Carvajal J., Physica B 192, 55, (1993).

GROWTH OF FeTe SINGLE CRYSTALS AND INVESTIGATION OF THEIR STRUCTURE AND MAGNETIC PROPERTIES

D. Croitori

Institute of Applied Physics, Academy of Sciences of Moldova, Chisinau, MD-2028 Republic of Moldova
E-mail: dorinacroitori@gmail.com

(Received October 31, 2016)

Abstract

In the present work, the growth of $Fe_{1+x}Te$ single crystals by the Bridgman method, their structure and magnetic properties are reported. The chemical composition of the $Fe_{1.06}Te$ crystals is determined from the X-ray diffraction pattern. The magnetic measurements reveal a phase transition from the paramagnetic into the antiferromagnetic state at 64 K. The calculated asymptotic Curie–Weiss temperature Θ_{CW} =-203 K indicates the dominance of antiferromagnetic interactions.

1. Introduction

The discovery of superconductivity in layered $LaAsO_{1-x}F_x$ with transition temperature T_C = 26 K in 2008 [1] has captured the imaginations of physicists worldwide. The crystal structure of this material is tetragonal and contains FeAs layers alternating along the *c*-axis with arrangement of the Fe atoms in a square planar lattice. In a short time, other Fe-based superconductors with a similar crystal structure were discovered with T_C of up to 56 K. These materials are of interest because of high critical temperatures and extremely large critical fields, which are promising for modern electronics and power applications. The present study addresses the FeTe compound, which can be transformed into a superconductor by doping with Rb or Se ions. The FeTe structure contains a square lattice of Fe atoms at high temperatures that can be distorted at low temperatures. This compound crystallizes in the tetragonal structure within the P4/nmm space group. Each Fe ion is tetrahedrally coordinated by four Te ions [2].

2. Experimental

FeTe single crystals were grown by the Bridgman method. Pieces of elemental Fe and Te with a purity of 99.99 % for Fe and 99.999% for Te were used. Tellurium was additionally purified by zone melting to remove the residual oxide impurity. The starting materials in the $Fe_{1.1}Te$ stoichiometry were loaded in a double quartz ampoule evacuated to 10^{-2} mbar. The ampoule was sealed and heated to 1100^{o}C at a rate of 300 ^{o}C/h, soaked at this temperature for 5 h, and then slowly pulled at a rate of 3mm/h through a temperature gradient of 350^{o}C at a rotation speed of 5 rpm. The final cooling rate below 750^{o}C was 60 ^{o}C/h. The solidified ingot had a clear sign of phase separation with a non-crystallized upper part and a shiny mirror-like single-

crystal bottom part. The bottom part was easily cleaved; the samples from this part were used for the studies. The crystal structure of the FeTe samples was analyzed using a conventional X-ray powder diffractometer (STADI-P, STOE&CIE). The composition of the sample was also measured by wave-length-dispersive X-ray electron-probe microanalysis (Cameca SX50). Magnetic measurements were performed in a temperature range of 2–400 K and magnetic fields up to 50 kOe using a MPMS 5 SQUID magnetometer.

3. Results and discussion

Figure 1 shows the X-ray diffraction pattern of the crushed FeTe single crystals. The experimentally observed pattern was processed by the Rietveld refinement program using FULLPROF SUITE [3]. X-ray analysis revealed the $Fe_{1.06}Te$ stoichiometry, which indicates the deviation from the starting stoichiometry in agreement with the observed phase separation. No additional reflections related to possible impurity phases were detected. From the refined pattern, the main structural parameters, such as lattice constants ($a = b = 3.823(3)$ Å and $c = 6.286(2)$ Å), were determined.

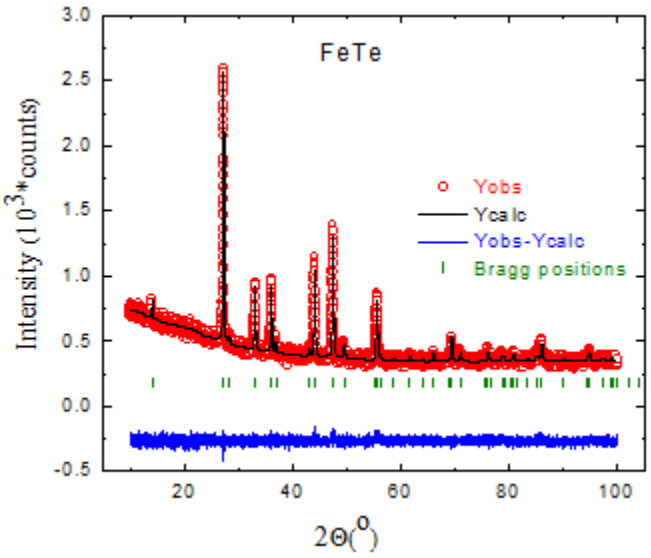

Fig. 1. Room temperature X-ray powder difraction pattern for the $Fe_{1.06}Te$ sample. Red circles show the observed intensity; black solid line is the calculated pattern; blue line shows the difference between the observed and calculated patterns; and green vertical lines show the Bragg reflections.

The magnetic field dependence of the magnetization measured at a temperature of 2 K is shown in Fig. 2. The linear behavior of this dependence indicates the antiferromagnetic type of ordering.

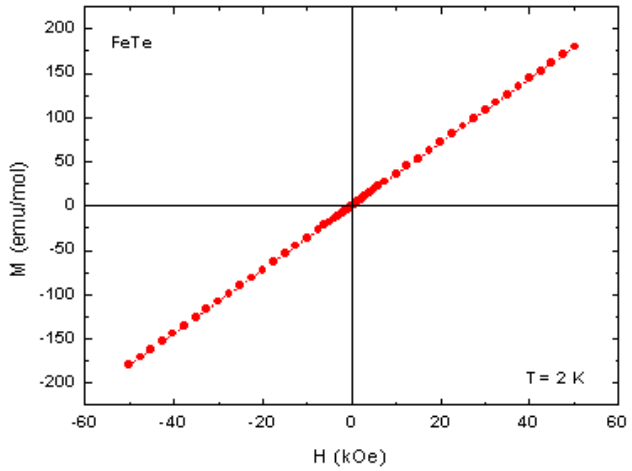

Fig. 2. Magnetization *M* versus applied magnetic field *H* for the $Fe_{1.06}Te$ single-crystaline sample measured at 2 K.

Figure 3 shows the temperature dependence of the magnetic susceptibility (upper panel) and the reciprocal of susceptibility (lower panel) for the $Fe_{1.06}Te$ single-crystal sample. The magnetic field of 10 kOe was applied parallel to the *c* axis of the sample. The magnetic susceptibility of $Fe_{1.06}Te$ continuously increases with decreasing temperature to 64 K and then undergoes a sharp decrease below this temperature. At this temperature, the phase transition from the paramagnetic state into the antiferromagnetically ordered state occurs. At high temperatures, the susceptibility follows the Curie–Weiss law. From the linear part of the temperature dependence of the reciprocal of susceptibility at high temperatures (300–400 K), the Curie–Weiss temperature of Θ_{CW} = –203 K was determined which indicates the dominance of the antiferromagnetic interactions in this compound. The calculated effective magnetic moment is 3.70 μ_B. This value is significantly reduced compared to the value of 4.9 μ_B expected for the localized Fe^{2+} ions in the high-spin state and indicates the presence of itinerant magnetic moments in this compound.

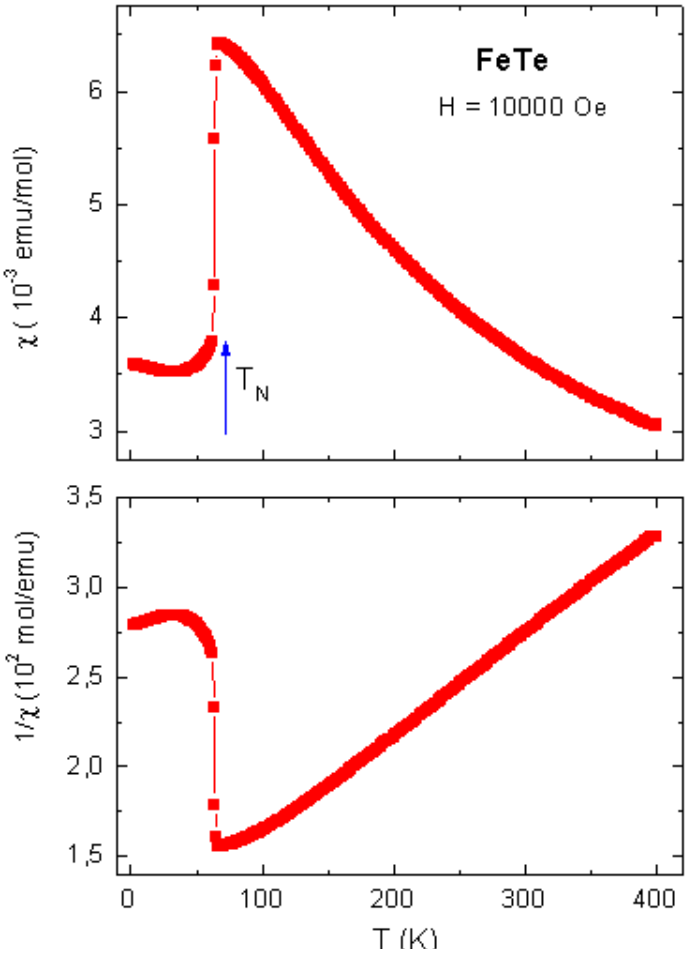

Fig. 3. Temperature dependence of magnetic susceptibility (upper panel) and reciprocal of susceptibility (lower panel) for the $Fe_{1.06}Te$ single crystal measured in a field of 10 kOe applied along the *c*-axis. The arrow marks the transition temperature.

4. Conclusions

Using the Bridgman method, perfect bulk single crystals of $Fe_{1.06}Te$ have been grown. The structural analysis by conventional X-ray powder diffraction has revealed a tetragonal crystal structure and the absence of impurity phases. The basic magnetic parameters, such as transition temperature T_N = 64 K and the Curie–Weiss temperature of Θ_{CW} = –203 K, have been determined from magnetic susceptibility measurements. The results of this study have shown that the magnetic ground state of $Fe_{1.06}Te$ is antiferromagnetic.

Acknowledgments. The author would like to thank Dr. hab. V. Tsurkan for supervision of this work and Dr. I. Filippova, Dr. V. Felea, and L. Prodan for assistance with the data processing and discussion of the results.

References

[1] Y. Kamihara and T. Watanabe, J. Am. Chem. Soc. 130, 3296, (2008).
[2] J. W. Lynn and P. Dai, Physica C 469, 469, (2009).
[3] J. Rodriguez-Carvajal, Physica B 192, 55, (1993).

EXPERIMENTAL AND THEORETICAL TEMPERATURE DEPENDENCES OF THE KINETIC COEFFICIENTS OF $Pb_{0.82}Sn_{0.18}Te$

D. Meglei and S. Alekseeva

Gitsu Institute of Electronic Engineering and Nanotechnologies, Academy of Sciences of Moldova, Academiei str. 3/3, Chisinau, MD-2028 Republic of Moldova

E-mail: meglei@nano.asm.md

(Received November 25, 2016)

Abstract

A special technology for gas-phase growth of single crystals using high-purity Pb, Sn, and Te of the OSCh-0000 grade as initial materials has been developed. Microstructural and spectral studies and Hall-effect measurements have confirmed the high quality of the prepared $Pb_{1-x}Sn_xTe$ (x = 0.18) single crystals.

1. Introduction

Significant interest in studying the properties of narrow-gap semiconductors, particularly lead telluride–tin telluride single crystals, is attributed to broad possibilities of the practical use of these materials as detectors and radiation sources in the infrared spectrum, thermocouples, strain gauges, etc. At the same time, scientific interest in these materials is primarily associated with their unusual galvanomagnetic, thermomagnetic, and magneto-optical properties.

Calculation of kinetic coefficients in semimetals and narrow-gap semiconductors in general is an extremely difficult problem because it is impossible to strictly take into account all the factors related to charge transfer in the crystal owing to the strong nonparabolicity of the bands and the complex mechanism of carrier scattering.

However, an experimental study of transport phenomena in these semiconductors provides the most complete information on the kinetics and energy spectrum of charge carriers over a wide range of variation in the charge carrier concentration, impurities, and temperature.

2. Results and discussion

The quality requirements for the samples under study are very high in order to obtain reliable experimental results: the volume distribution of the components must be uniform, and mechanical defects must be reduced to minimum. The most effective technique for preparing homogeneous $Pb_{1-x}Sn_xTe$ single crystals is the gas-phase growth method. We have developed a special technology for gas-phase growth of single crystals using high-purity Pb, Sn, and Te of the OSCh-0000 grade as initial materials (Te was purified by multiple zone recrystallization).

Microstructural and spectral studies and Hall-effect measurements have confirmed the high quality of the prepared $Pb_{1-x}Sn_xTe$ (x = 0.18) single crystals.

Temperature studies of conductivity σ and Hall coefficient were conducted according to standard procedures in a temperature range of 77–400 K.

A comprehensive study of the temperature dependence of thermopower, electric conductivity, and Hall effect and the dependence of thermopower on the magnetic field induction, which was conducted using the same samples, provided the calculation of a number of kinetic parameters of five $Pb_{1-x}Sn_xTe$ (x = 0.18) samples with different charge carrier concentrations.

In our previous studies [1–3], the Shubnikov–de Haas oscillations, the temperature dependence of thermopower, and the dependence of thermopower on the magnetic field induction were examined using $Pb_{0.82}Sn_{0.18}Te$ samples with identical carrier concentrations. The experimental temperature dependences of the Hall effect, electric conductivity, and carrier mobility of $Pb_{1-x}Sn_xTe$ with different carrier concentrations are shown in Figs. 1–3.

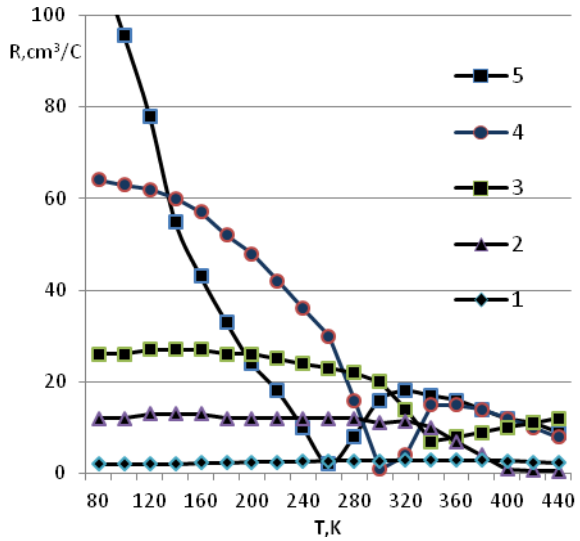

Fig.1. Temperature dependences of the Hall coefficient of five $Pb_{0.82}Sn_{0.18}Te$ samples with a carrier concentration of (*1*) 200, (*2*) 15, (*3*) 5.2, (*4*) 2.6, and (*5*) 0.52×10^{17} cm^{-3}.

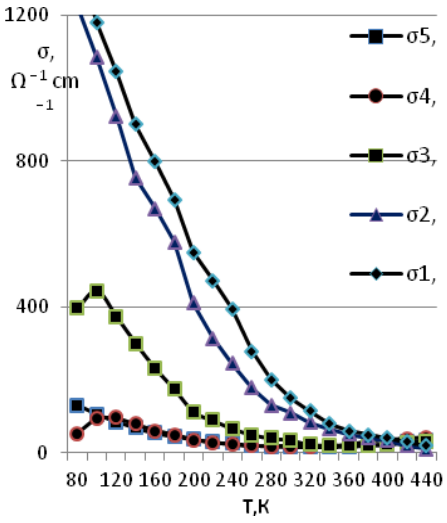

Fig.2. Temperature dependences of the electric conductivity of five $Pb_{0.82}Sn_{0.18}Te$ samples with a carrier concentration of (*1*) 200, (*2*) 15, (*3*) 5.2, (*4*) 2.6, and (*5*) 0.52×10^{17} cm^{-3}.

The temperature dependences of the electric conductivity and carrier mobility of $Pb_{0.82}Sn_{0.18}Te$ in a region of T < 280 K for the fourth sample are shown in Figs. 4 and 5. The temperature dependence of the carrier mobility for this sample, in common with the third sample (Fig. 3), can be quite accurately described by the following expressions: $\mu = \alpha \times T^{1.5}$, 80 K < T < 120 K and $\mu = \beta \times T^{-1.8}$, 120 K < T < 280 K (α and β are fitting parameters). The calculation results are shown in Figs. 6 and 7.

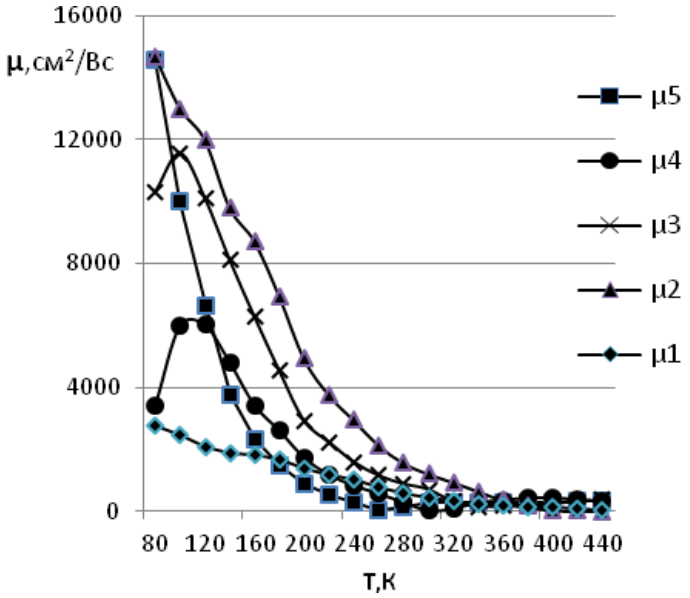

Fig. 3. Temperature dependences of the carrier mobility of five $Pb_{0.82}Sn_{0.18}Te$ samples with a carrier concentration of (*1*) 200, (*2*) 15, (*3*) 5.2, (*4*) 2.6, and (*5*) 0.52×10^{17} cm^{-3}.

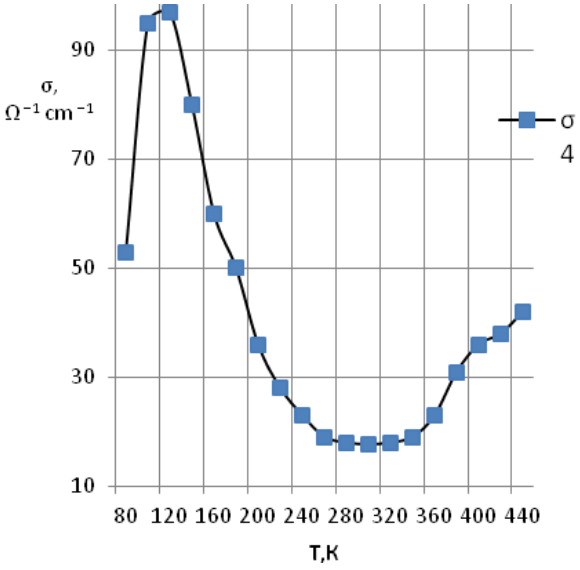

Fig. 4. Temperature dependence of the electric conductivity of $Pb_{0.82}Sn_{0.18}Te$ with a carrier concentration of 2.6×10^{17} cm^{-3}.

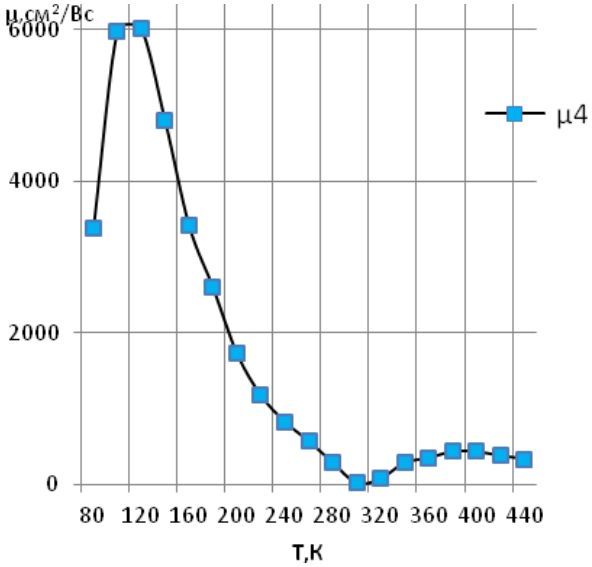

Fig. 5. Temperature dependence of the carrier mobility of $Pb_{0.82}Sn_{0.18}Te$ with a carrier concentration of 2.6×10^{17} cm^{-3}.

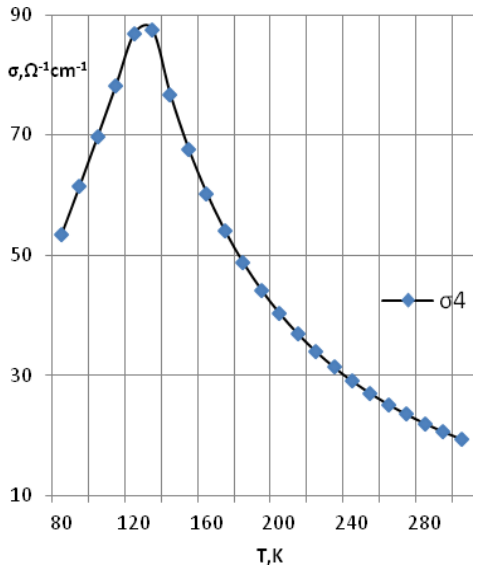

Fig. 6. Calculated temperature dependence of the electric conductivity of $Pb_{0.82}Sn_{0.18}Te$ with a carrier concentration of 2.6×10^{17} cm^{-3}.

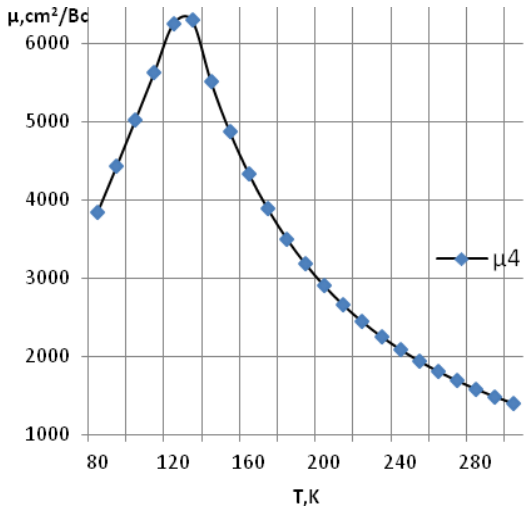

Fig. 7. Calculated temperature dependence of the carrier mobility of $Pb_{0.82}Sn_{0.18}Te$ with a carrier concentration of 2.6×10^{17} cm^{-3}.

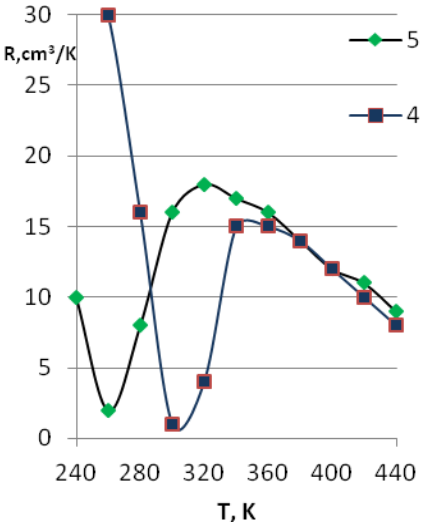

Fig. 8. Temperature dependences of the Hall coefficient of the fourth and fifth $Pb_{0.82}Sn_{0.18}Te$ samples.

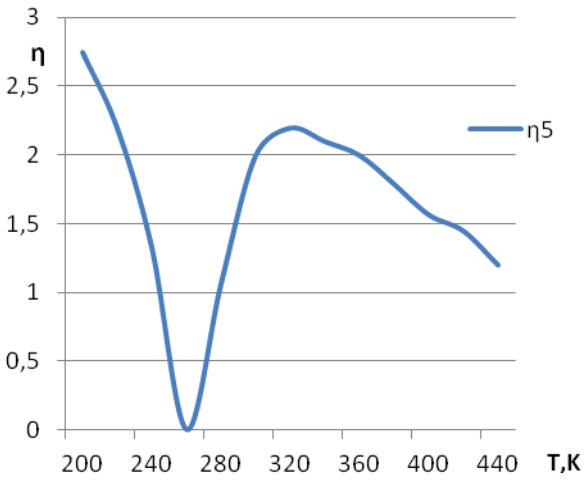

Fig. 9. Calculated temperature dependence of $\eta = \frac{p_1}{p_2}$ of the fifth $Pb_{0.82}Sn_{0.18}Te$ sample.

The temperature dependence of the Hall coefficient of $Pb_{0.82}Sn_{0.18}Te$ at $T > 280$ K (Fig. 8) can be attributed to the presence of two types of holes, i.e., light and heavy holes [4–9]. In this

case, the kinetic coefficients of conductivity (σ) and Hall coefficient (R) are determined by contributions of current carriers of both extremes according to the following expressions [6]:

$\sigma = \sigma_1 + \sigma_2$, $R = (\frac{\sigma_1}{\sigma})^2 + (\frac{\sigma_2}{\sigma})^2$, or

$1 = \frac{\eta b}{1+\eta b} + \frac{1}{1+\eta b}$, $\quad R = R_1(\frac{\eta b}{1+\eta b})^2 + R_2(\frac{1}{1+\eta b})^2$, where $\eta = \frac{p_1}{p_2}, a\ b = \frac{\mu_1}{\mu_2}$.

The maximum Hall coefficient value corresponds to the condition $\sigma_1 = \sigma_2$, or $\eta b = 1$; hence, $\frac{R_{max}}{R_0} = \frac{(b+1)^2}{4b}$; therefore, the b value for the fourth and fifth samples can be calculated according to the curves in Fig. 8: $b_5 = 6.85$ and $b_4 = 12.9$. According to the determined b values, using the experimental temperature dependences of the Hall coefficient, it is possible to calculate the temperature dependence of $\eta = \frac{p_1}{p_2}$, which is shown in Fig. 9.

References

[1] D. Meglei and S. Alekseeva, Proc. of IV Int. Conf. "Telecomunicatii, Electronica si Informatica", Chisinau, 2012.
[2] D. Meglei and S. Alekseeva, Mold. J. Phys. Sci. 13 (1–2), 153, (2014).
[3] D. Meglei and S. Alekseeva, Mold. J. Phys. Sci. 14 (3–4), 154, (2015).
[4] G. Lashkarev, D. Meglei, A. Shevchenko and K.Tovstyuk, Phys. Stat. Sol. (b) 63, 663, (1974).
[5] G. Lashkarev and M. Radchenko, Ukr. J. Phys. 27, 747, (1982).
[6] S. Nemov, N. Blagih, and M. Jafarov, Phys. Eng. Semicond. 48, 1027, (2014).
[7] P. Konstantinov, L. Prokofiev, M. Fedorov, D. Pshenay-Severin, Y. Ravitch,V. Kompaniets, and V. Chistyakov, Phys. Eng. Semicond. 39, 1059, (2005).
[8] A. Vaganean, V. Arutyunean, E. Bagiean, A. Epremean, and V. Abrahamean Proc. of National Academy of Sciences of Armenia, Physics, 42, 96, (2007).
[9] Y. Grekov, N. Semikolenova, and T. Shlyakhov, Phys. Eng. Semicond. 31, 990, (1997)

SERIES AND PARALLEL CONNECTION OF INDIVIDUAL Pd-MODIFIED ZnO NANOWIRES FOR GAS SENSING APPLICATIONS

O. Lupan[1,2,3*], V. Postica[1], V. Cretu[1], T. Pauporte[3], and R. Adelung[2]

[1]Department of Microelectronics and Biomedical Engineering, Technical University of Moldova, Stefan cel Mare Av. 168, Chisinau, MD-2004 Republic of Moldova,
Email: oleg.lupan@mib.utm.md
[2]Faculty of Engineering, Institute for Materials Science, Christian-Albrechts Universität zu Kiel, Kaiser Str. 2, Kiel, D-24143 Germany
E-mail: ollu@tf.uni-kiel.de
[3]PSL Research University, Chimie ParisTech-CNRS, Institut de Recherche de Chimie Paris, UMR8247, 11 rue Pierre et Marie Curie, Paris, 75005 France
E-mail: thierry.pauporte@chimie-paristech.fr

(Received September 5, 2016)

Abstract

The hydrogen gas sensing properties of nanodevices based on two ZnO nanowires (NWs) functionalized/modified with palladium (Pd/ZnO) at room temperature are studied. The main goal of the study is to find which of the connections—in series or in parallel—is more favorable to improve the properties of a double NW nanodevice in comparison with a single Pd/ZnO NW-based nanosensor. An enhancement in gas response is observed in both cases. In the case of connection in series of two NWs, it is attributed to an increased number of Schottky barriers, which are directly related to sensor response to gases. In the case of parallel connection of two NWs, higher electrical currents can flow through the device; it improves the sensor response too; in addition, this type of device can be more easily integrated in electronics due to higher currents in passive regime (in air) and is more stable.

1. Introduction

The extraordinary properties of nanostructures are quite attractive for the development of novel analytical nanodevices that have advantages over traditional microelectronic devices, such as lower-cost, simpler design, higher performance, selectivity, and sensitivity [1, 2]. In the past decade, scientists have paid a lot of attention to the integration of semiconducting oxide into nanodevice applications, in particular, miniature gas sensors and biosensors [2–8]. Nanosensors exhibit the following main advantages.

(i) Compared to devices based on metal oxide nano- and microstructures which need a high operating temperature for efficient performance (150–500ºC) [9], the nanosensors based on individual nanostructures can operate properly even at room temperature [2, 3, 5, 6]. This feature eliminates the necessity to produce and integrate microheaters; as a consequence, it is possible to reduce the cost and power consumption of the final device [4]. There are publications that describe efficient gas detection at room temperature of individual nanostructures down to ppb

level [2, 6]. In addition, it provides the possibility of using organic materials as a sensing structure for sensor applications [10, 11].

(ii) Due to operation at room temperature, the physical and chemical properties of the sensing material (e.g., NWs, nanobelts) do not change over time [5]; this feature is strategically important for long-term stability of gas sensors [12].

(iii) Ultra-low power consumption in a passive state. Due to low currents that pass through a nanostructure, the power consumption of nanodevices is in the nW range [2–4]. Since portable devices, e.g., smartphones, are in a rapid progress and extensively used due to commodity and time saving, the necessity of low-power electronics has become of vital importance [4]. Thus, the development of nanoelectronic devices can solve this problem.

(iv) Possibility of fabricating miniature low-weight devices. Nanometer sizes of the sensitive material provide a possibility of designing nanoelectronic systems, such as an electronic nose (e-nose) with high yield [13]. This is very important for wearable sensors, biomedical and biological sensors for continuous monitoring of different human body biosignals (glucose, oxygen saturation, etc.) and quality of environment (fast detection of toxic gases, such as CO and H_2S, or highly inflammable gases, such as H_2). Another important example is photodetectors of ultraviolet (UV) light, especially UV-B (λ = 280–315 nm), which can prevent risk factor of harmful effect of long exposure to dangerous sun rays.

In the past decades, miniaturization of electronic devices has been successfully implemented using "bottom–up" approaches, which have been extensively used to assembly semiconductor nanostructures into different devices, such as logic gates [14], gas sensors and biosensors [2, 15], photodetectors [4], etc. The next step of progress was combination and integration of several nanostructures in the same device; it has significantly extended the application domain [1, 14]. In the case of gas sensors, only comparison of gas sensing properties between single and multiple randomly oriented NWs has been reported [11, 16] and no comparison of series and parallel connected NWs has yet been made. Zhang *et al*. [6] have shown that multiple In_2O_3 NWs have higher reliability, sensitivity, and fabrication simplicity than those of single NWs. Khan *et al*. [16] have reported a higher gas response of multiple ZnO NWs compared to single NWs. In both cases, the effects can be related to the nanojunctions between NWs. The formed potential barriers in the nanojunctions are highly sensitive to gas species, and a higher modulation of device resistance can be obtained [16]. However, to date, there have been no reports on comparison of the gas sensing properties of NWs connected in parallel and series, which is very interesting from the fundamental point of view too. Insight into this idea can create a new paradigm in gas sensor science and engineering for fabrication of novel nanodevices with improved gas sensing properties and rational assembly/design of sensing devices.

In this study, we describe the gas sensing properties of nanodevices based on two Pd/ZnO NWs connected in series and parallel in order to find which of the connections is more favorable for improving the nanodevice performance in comparison with individual Pd/ZnO NWs (reported in Ref [17]). Our experimental results have shown that connection in series can significantly—about 2 times—improve the sensing properties of the nanodevice, while connection in parallel is less effective. The mechanism responsible for gas sensing of both types of devices has been discussed in detail. The enhancement in response in the case of connection in series can be attributed to an increased number of Schottky barriers (SBs).

2. Experimental

The Pd/ZnO NWs were grown by one-step electrochemical deposition (ECD) in a classical three-electrode electrochemical cell at 90 °C as described in Ref [17, 18]. The F-doped SnO_2 (FTO, 10 Ω/sq) films were used as substrates and as a working electrode for electrodepositon [17, 18]. The substrate cleaning procedure was described in Ref [17, 18]. The dependence of the morphological, structural, optical, and chemical properties on the concentration of the $PdCl_2$ solution added in the electrolyte solution was studied in detail in Ref [17]. TEM measurements showed the growth of Pd nanoparticles (NPs) onto the ZnO NW surface [17]. In addition, it was reported by Yang *et al*. [19] that Pd deposition occurs at high current efficiency and the process of Pd NP growth can be described by the following equation [19, 20]:

$$PdCl_4^{2-}(aq) + 2e^- \rightarrow Pd(s) + 4Cl^- \quad (1)$$

In this study, NWs from samples grown with the addition of 1 μM $PdCl_2$ (Alfa Aesar) into an electrolyte solution were examined. This concentration leads to a 0.6 at% Pd content in Pd/ZnO samples [17]. Morphological, structural, and chemical studies were performed by SEM, XRD and EDX techniques as described in [17, 18]. The gas sensing studies were conducted at room temperature at a 30% relative humidity as described in [3, 4]. Electrical measurements were continuously recorded using a Keithley 2400 source meter controlled through Lab View software (National Instruments). The nanosensor was prepared using a FIB/SEM system as described in Ref [3, 4]. All sensors exhibited a typical *n*-type behavior; that is, the resistance of the nanodevices decreased during exposure to H_2. Gas response (S) was defined as $S = R_{air}/R_{gas}$, where R_{air} and R_{gas} are the resistances of the nanodevice in air and under H_2.

3. Results and discussion

3.1. Characterization of Pd/ZnO NW arrays

Figures 1a–1c show SEM images of Pd/ZnO NW arrays at different magnifications (from lower (Fig. 1a) to higher magnification (Fig. 1c)). The NWs are vertically aligned on an FTO substrate and show a homogenous and uniform coverage. The preferential anisotropic growth is known to result from differences in growth rates of the different crystal faces of ZnO, i.e., much higher growth rate of the (0001) surface than that of the $\{10\bar{1}0\}$ faces [21].

Details of pristine ZnO NW array morphology and the effect of various parameters of ECD can be found in Ref [18, 22]. The diameter (D) of NWs is in a range of 100–200 nm (measured using top view images, Fig. 1c), while the length (L) is in a range of 1–3 μm (from cross-sectional images, not shown here). The density of NWs is ≈10 NW/μm^2. Figure 1d shows the XRD pattern of the Pd/ZnO NW arrays recorded in a range of 10°–80° with a scanning step of 0.02°. All detected diffraction peaks can be attributed to the ZnO crystal phase with a hexagonal wurtzite structure (PDF#00-036-1451) and the SnO_2 crystal phase with a tetragonal structure (PDF#01-088-0297) originated from the FTO (SnO_2 : F) substrate [17, 18]. Peaks attributed to Pd, Pd-oxide phase (PdO), or impurities were not observed in the measured XRD spectra of investigated sample [12]. Higher intensity of the XRD peak corresponding to the (002)

plane (Fig. 1d) confirms SEM data on the preferential growth of NWs along the *c*-axis normal to the substrate (Figs. 1a–1c).

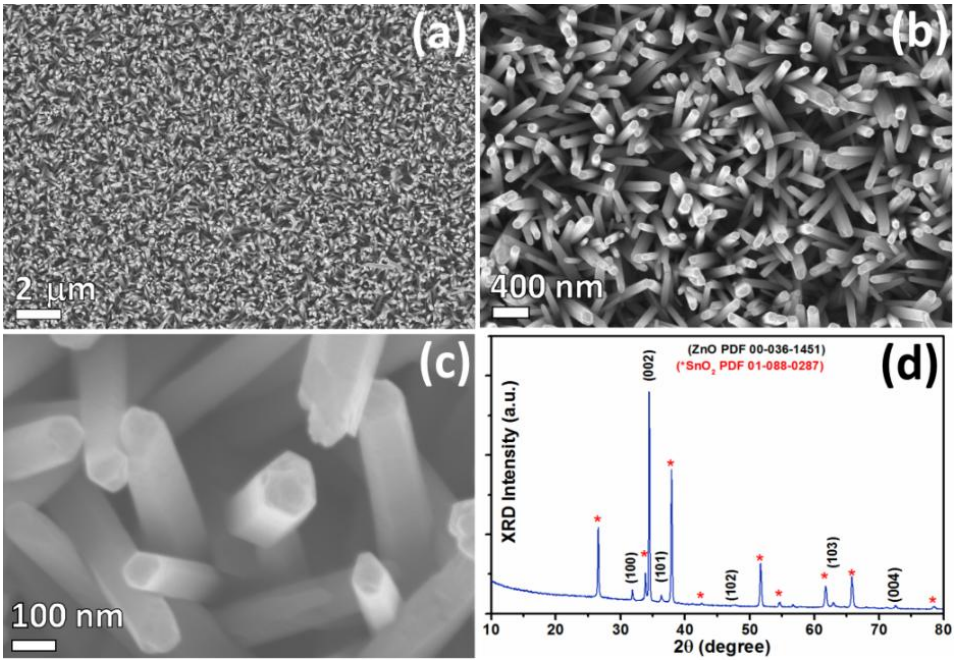

Fig. 1. (a–c) SEM images of Pd/ZnO nanowire arrays grown by ECD method on an FTO substrate at different magnifications (from low (a) to high (c)). (d) XRD spectrum of Pd/ZnO nanowire arrays and FTO (SnO_2 : F) substrate.

Figure 2 shows the EDX-line scan profile of Zn, O, and Pd taken along (Fig. 2b) and across (Fig. 2c) the Pd/ZnO NW agglomeration. It was observed that the Zn and O profiles properly follow the position of Pd/ZnO NWs, which is more clear in the case of line data 3 (Fig. 2c). However, due to the low content of Pd (0.6 at%) on the Pd/ZnO NWs surface, no detectable changes of Pd profile are observed (see Fig. 2).

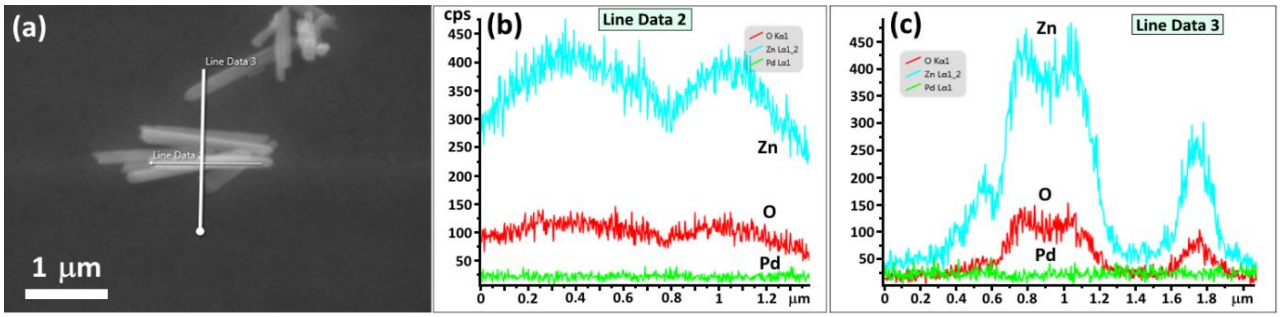

Fig. 2. (a) SEM image of EDX-scanned regions. EDX-line scan profile of Zn, O, and Pd taken: (b) along; and (c) across the Pd/ZnO NWs.

3.2. Series and parallel connection of individual Pd/ZnO NWs for nanodevices in gas sensing applications

Figure 3a shows a device based on two Pd/ZnO NWs connected in series to pre-patterned Au pads of a SiO_2/Si chip by Pt contacts (Device 1). Each NW was designated as NW1 and NW2. The *D* and *L* values of both NWs are in the same range (diameter $D \approx 160$ nm and length $L \approx 1$ μm). Zoomed views of each of the NWs are shown in Figures 3b and 3c. The current–voltage curves show the formation of double Schottky contacts at the Pt/ZnO interfaces (Fig. 3d). Since electron affinity (χ) of ZnO is 4.5 eV and the work function (ϕ_m) of Pt is 6.1 eV, a SB at the Pt/ZnO interface was formed (Fig. 3e) [23]. Thus, the schematic structure of Device 1 connected to the measurement unit was represented in Fig. 3f, where R_{NW1} and R_{NW2} denote the resistance of NW1 and NW2, respectively, and Schottky diodes represents the SBs formed at the Pd/ZnO interface. Device2 consists of two Pd/ZnO NWs connected in parallel (see Fig. 3g). As in the case of Device1, the NWs are designated as NW1 and NW2. The *D* and *L* values of both NWs are in the same range ($D \approx 190$ nm and $L \approx 1.3$ μm). Zoomed views of each of the NWs are shown in Fig. 3h and Fig. 3i. The same double-Schottky characteristic was observed for Device2 (see Fig. 3j). The respective schematic structure of Device2 connected to the measurement unit is shown in Fig. 3k.

Next, the gas sensing studies of the fabricated devices (Devices 1 and 2) will be described. Figure 4a shows the gas response of a single NW nanosensor (curve *1*) and two individual Pd/ZnO NWs connected in series (curve 2) to 100 ppm H_2 gas at room temperature. All NWs integrated in the devices are from the same sample (SEM image for the device based on a single NW is not shown here) and have approximately the same geometrical dimensions ($D \approx 160 \pm 5$ nm and $L \approx 1 \pm 0.5$ μm). It is evident that the gas response increases about 2 times in the case of connection of two individual Pd/ZnO NWs in series compared to a single NW ($S \approx 105$ for a single NW and $S \approx 206$ for double NWs connected in series, see Fig. 4a). Only a slight difference in response time τ_r and recovery time τ_d (defined as necessary times for reaching and recovering 90% of full response, respectively) was observed. Thus, for the single NW, $\tau_r \approx 28$ s and $\tau_d \approx 31$ s, while for the NWs connected in series, $\tau_r \approx 24$ s and $\tau_d \approx 30$ s.

In the case of Device 2, an enhancement in gas response by about 1.3 times was obtained in the case of connection of two individual Pd/ZnO NWs in parallel compared to a single NW-based nanosensor ($S \approx 95$ for a single NW and $S \approx 120$ for NWs connected in series, see Fig. 4b). As in the case of connection in series (Device 1, Fig. 4a), the parallel NWs integrated in devices (Device 2, Fig. 4b) have approximately the same geometric dimensions ($D \approx 190 \pm 5$ nm and $L \approx 1.3 \pm 0.5$ μm). It is evident that the response and recovery times are not quite different and lie in a range of ≈20 s and ≈30 s, respectively (see Fig. 4b).

The sensitivity obtained for Device 1 and Device 2 is ≈200%/ppm and ≈120%/ppm, respectively. These values are lower than those reported for Pd/InP and Pd/SiO_2/AlGaN diode-based sensors [24, 25]; however, the metal–semiconductor–metal (double Schottky) structure described in this study can be more easily fabricated to the diode-based device reported previously (since the Ohmic contact is not needed and technological processing steps are reduced) [26, 27]. In addition, in the case of a double Schottky structure, it is not necessary to study the optimal reverse bias voltage for higher sensitivity, since it exhibits bi-directional sensing capabilities and is more suitable for long-term detection for reverse and forward applied bias voltages [26, 27]. Figure 5 shows the proposed mechanism of the SB height (SBH) variation

for the Pt/ZnO NW/Pt sensor structure (double Schottky) at equilibrium in vacuum (Fig. 5a), at an applied bias voltage in vacuum (Fig. 5b), during exposure to ambient air with adsorption of oxygen ions at the Pt/ZnO interface (Fig. 5c), and during exposure to hydrogen gas with the formation of a dipole layer at the Pt/ZnO interface (Fig. 5d).

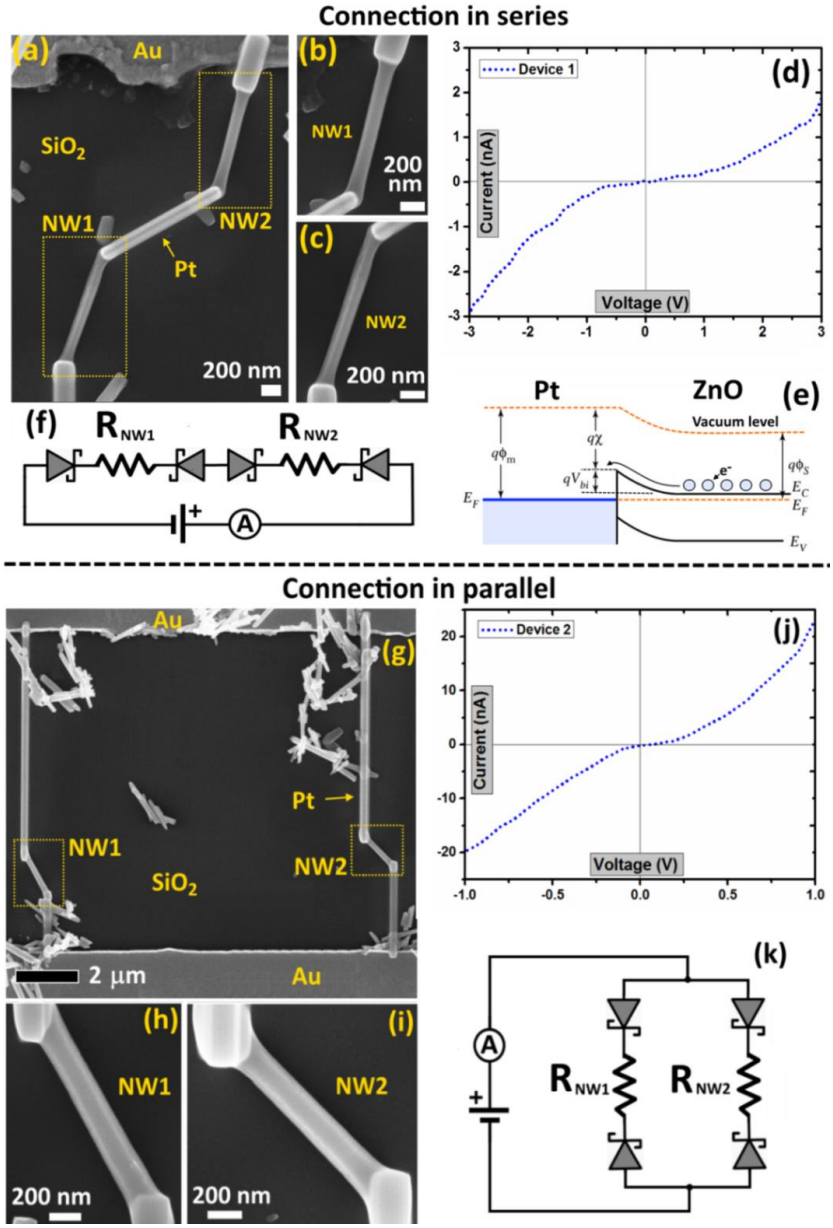

Fig. 3. (a) SEM image of Device 1 based on two Pd/ZnO NWs connected in series and zoomed-in regions of NW1 (b); and NW2 (c). (d) Current–voltage characteristic of Device 1 in the dark at room temperature. (e) Schematic structure of Device 1 connected to the measurement unit. (f) Energy band diagram of the Pt/ZnO contact. (g) SEM image of Device 2 based on two Pd/ZnO NWs connected in parallel and zoomed-in regions of NW1 (h); and NW2 (i). (j) Current–voltage characteristic of Device 2 in the dark at room temperature. (k) Schematic structure of Device 2 connected to the measurement unit.

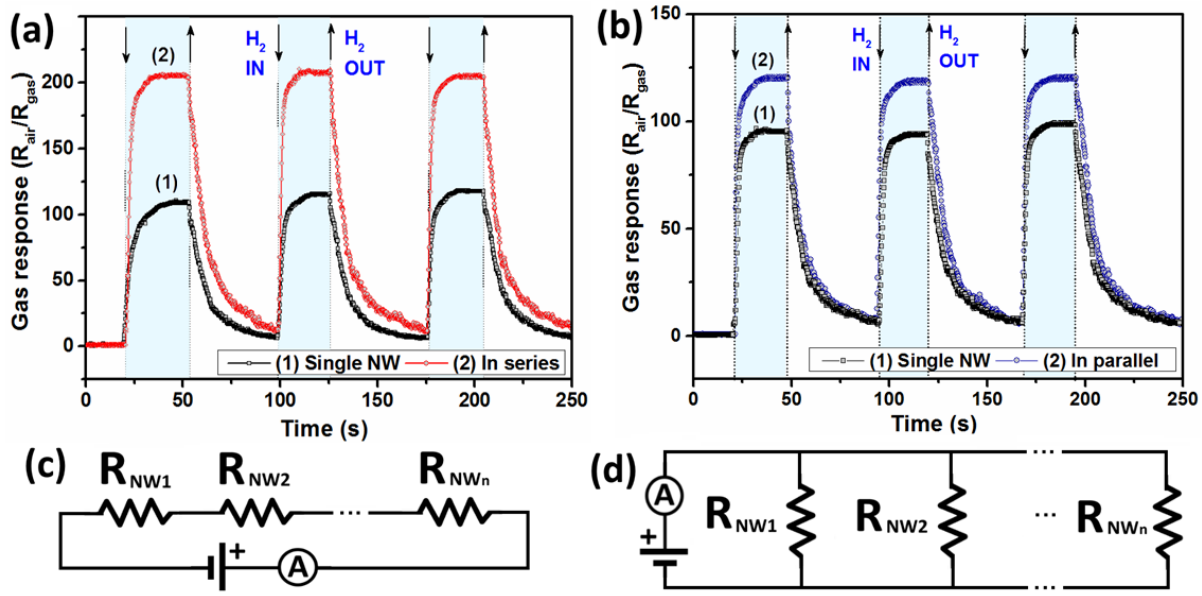

Fig. 4. (a) Gas response of a single NW and two Pd/ZnO NWs connected in series to 100 ppm H_2 gas (diameter $D \approx 160$ nm and length L ≈ 1 μm). (b) Gas response of a single NW and two Pd/ZnO NWs connected in parallel to 100 ppm H_2 gas ($D \approx 190$ nm and $L \approx 1.3$ μm). Schematics of the sensor structure based on individual Pd/ZnO NWs connected: (c) in series; and (d) in parallel.

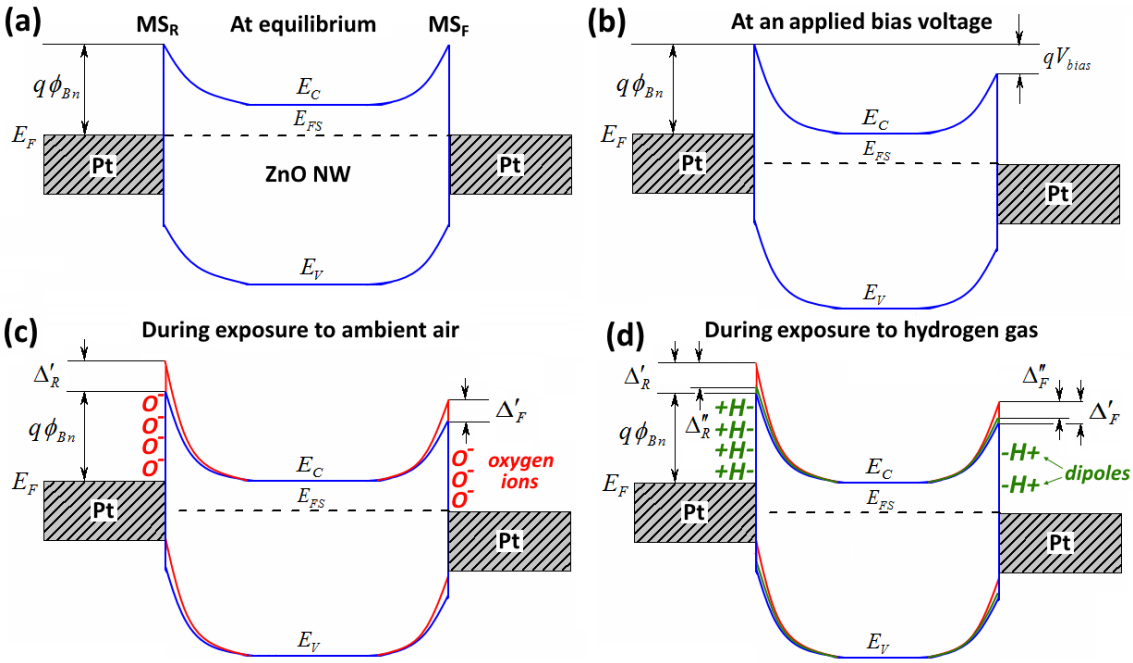

Fig. 5. Proposed mechanism of the SBH variation for the Pt/ZnO-NW/Pt sensor structure based on energy band diagrams: (a) at equilibrium in vacuum; (b) at an applied bias voltage in vacuum; (c) during exposure to ambient air with the adsorption of oxygen ions at the Pt/ZnO interface; and (d) during exposure to hydrogen gas with the formation of a dipole layer at the Pt/ZnO interface.

According to theoretical studies, the current density magnitude of the double Schottky structure at V_{bias} is dominated by the metal/semiconductor contact at a reverse bias voltage (MS_R). Taking into account that the voltage drop across the metal/semiconductor contact at a forward bias (MS_F) is low and the voltage drop across the MS_R is close to V_{bias}, the current density through the structure exposed to ambient air (J_{air}) can be expressed as follows [27, 28]:

$$J_{air} \approx A^* T^2 \exp\left(\frac{-\phi_{Bn} - \Delta'_R}{V_T}\right) \tag{2}$$

where A^* is the Richardson's constant, T is the absolute temperature, ϕ_{Bn} is the effective barrier height (EBH), Δ'_R is the change in EBH of MS_R associated with the adsorption of oxygen species [28] and V_T is the thermal voltage. In the case of exposure of the sensor structure to H_2 gas mixed with air, the current density magnitude (J_{gas}) is still determined by MS_R [27, 28]:

$$J_{gas} \approx A^* T^2 \exp\left(\frac{-\phi_{Bn} - \Delta'_R + \Delta''_R}{V_T}\right) \tag{3}$$

where Δ''_R is the change in EBH induced by the dipole layer of MS_R as a result of dissociation and diffusion of hydrogen molecules [27]. At a fixed temperature, the variation in SBH of MS_R ($\Delta\phi_{BR}$) due to H_2 gas adsorption in the Schottky contact region can be expressed as follows [26, 29]:

$$\Delta\phi_{BR} = V_T \ln\left(\frac{J_{air}}{J_{gas}}\right) = V_p \ln\left(F\frac{[H_2]}{[H_2]_0}\right) \tag{4}$$

where V_p is a fitting parameter, F is an equilibrium constant associated with the H^+ ion coverage at the Pt/ZnO interface, $[H_2]$ is the H_2 gas concentration (in our case, 100 ppm), and $[H_2]_0$ is the intrinsic H_2 gas concentration in ambient air used for measurements (≈0.5 ppm) [26]. Accordingly, the sensor response can be expressed as follows [27]:

$$S = \frac{R_{air}}{R_{gas}} = \frac{J_{gas}}{J_{air}} = \exp\left(\frac{\Delta''}{V_T}\right) \tag{5}$$

The role of Pd NPs in the improvement of hydrogen gas sensing abilities was discussed in previous work [17]; it was attributed to an electrical sensitization mechanism (formation of a space charge region around the Pd, i.e., nano-SBs that narrow the conduction channel) and chemical sensitization mechanism (catalytic dissociation of molecular oxygen by Pd NPs, i.e., "spillover effect" which contributes to electron withdrawal from the ZnO NW) [30, 31]. Such properties of Pd as work function and conductivity are known to be efficiently modulated by the adsorption of H_2 gas. For details, see [17].

Next, the main causes of gas response enhancement in the case of series and parallel connection of two individual Pd/ZnO NWs will be analyzed. First, consider the case where SBs are excluded from the electrical circuit; that is, Ohmic contacts are formed at both ends of NWs. Since the nanostructures have approximately equal geometric dimensions in the two cases, on the assumption that n NWs are connected in series (see Fig. 4c), the following condition can be true: $R_{NW1(air)} \approx R_{NW2(air)} \approx \ldots \approx R_{NWn(air)}$ and $R_{NW1(gas)} \approx R_{NW2(gas)} \approx \ldots \approx R_{NWn(gas)}$, where $R_{NW(air)}$ and $R_{NW(gas)}$ are the resistances of NWs exposed to the air and H_2 gas, respectively. Thus, in the case

of series connection, the total resistance of the device exposed to the air ($R_{T(air),series}$) and H_2 gas ($R_{T(air),series}$) is as follows [32]:

$$R_{T(air),parallel} = \sum_{i=1}^{n} R_{NWi(air)} = nR_{NW(air)} \quad (6)$$

$$R_{T(gas),parallel} = \sum_{i=1}^{n} R_{NWi(gas)} = nR_{NW(gas)} \quad (7)$$

Hence, the gas response can be defined as follows [32]:

$$S = \frac{R_{T(air),series}}{R_{T(gas),series}} = \frac{R_{NW(air)}}{R_{NW(gas)}} \quad (8)$$

In the case of connection in parallel, on the assumption that *n* NWs are connected in parallel (see Fig. 4d), the total resistance of the device exposed to the air ($R_{T(air),parallel}$) and H_2 gas ($R_{T(gas),parallel}$) is as follows [32]:

$$\frac{1}{R_{T(air),series}} = \sum_{i=1}^{n} \frac{1}{R_{NWi(air)}} = \frac{1}{R_{NW(air)}} \cdot n \quad (9)$$

$$\frac{1}{R_{T(gas),series}} = \sum_{i=1}^{n} \frac{1}{R_{NWi(gas)}} = \frac{1}{R_{NW(gas)}} \cdot n \quad (10)$$

hence, the gas response can be defined as follows [32]:

$$S = \frac{R_{T(air),parallel}}{R_{T(gas),parallel}} = \frac{R_{NW(air)}}{R_{NW(gas)}} \quad (11)$$

In conclusion, the addition of *n* number of NWs in series or parallel does not lead to a significant enhancement in gas response; it is equal to the *S* value of a single NW. Thus, it is reasonable to expect that the enhanced response of connected NWs is due to the increased number of SBs, especially in the case of connection in series. Hu *et al*. showed that the formed SB to a single nanostructure can considerably increase gas response due to the higher sensitivity of the SBH (ϕ_{bi}) to adsorbed species in the Schottky contact region [15]. In addition, Katoch *et al*. [9] showed that a higher number of gas sensitive barriers in a nanomaterial enhance the gas response. Thus, we can speculate that, in our case, the enhanced response is attributed to an additional SB in series from the second NW.

However, in the case of connection in parallel, the SBs of NWs are in parallel and the number of SBs is the same in the two branches of current flow; thus, the slightly enhanced gas response can be attributed to another factor. Bai *et al*. [33] and Liu *et al*. [34] showed that an increased number of parallel ZnO NWs increase the detected photocurrent due to the increased number of channels for current flow. Thus, we believe that, in our case, for connection in parallel, the slight increase in gas response is due to possibility of higher current flow [34]. Further research is in progress.

4. Conclusions

The devices based on two individual Pd/ZnO NWs connected in series or in parallel have been successfully prepared using the Pt-deposition function of FIB/SEM scientific instrument and studied for gas sensing applications. An enhancement in gas response has been obtained in both cases. In the case of series connection of two Pd/ZnO NWs, the gas response has increased about two times, while in the case of connection in parallel, the gas response has increased only about 1.3 times. Thus, we can conclude that series connection is more efficient and better sensor performances are related to an increased number of SBs in the branch of current flow which are highly sensitive to adsorbed species in the contact regions. Thus, the described connection of nanostructures in series can be proposed as a promising method for rational fabrication of sensor devices with improved sensing properties.

Acknowledgments. The authors acknowledge professor dr. hab. Ion Tiginyanu, Institute of Electronic Engineering and Nanotechnologies, Academy of Sciences of Moldova, for discussions. The authors acknowledge the support from German Research Foundation (DFG) under scheme AD 183/12-1. This research was partly supported by project Institutional 45inst-15.817.02.29A funded by the Government of the Republic of Moldova and by the STCU within Grant 5989 at the Technical University of Moldova.

References

[1] Y. Cui and C.M. Lieber, Science 291, 851, (2001).
[2] Y. Cui, Q. Wei, H. Park, and C.M. Lieber, Science 293, 1289, (2001).
[3] O. Lupan, G. Chai, and L. Chow, Microelectron. Eng. 85, 2220, (2008).
[4] O. Lupan, V. Cretu, V. Postica, M. Ahmadi, B.R. Cuenya, L. Chow, I. Tiginyanu, B. Viana, T. Pauporté, and R. Adelung, Sens. Actuators B 223, 893, (2016).
[5] O. Lupan, V.V. Ursaki, G. Chai, L. Chow, G.A. Emelchenko, I.M. Tiginyanu, A.N. Gruzintsev, and A.N. Redkin, Sens. Actuators B 144, 56, (2010).
[6] D. Zhang, Z. Liu, C. Li, T. Tang, X. Liu, S. Han, B. Lei, and C. Zhou, Nano Lett. 4, 1919, (2004).
[7] O. Lupan, G. Chai, and L. Chow, Microelectron. J. 38, 1211, (2007).
[8] T. Shishiyanu, O. Lupan, L. Chow, S. Shishiyanu, and S. Railean, Mold. J. Phys. Sci. 7, 42, (2008).
[9] A. Katoch, Z.U. Abideen, H.W. Kim, and S.S. Kim, ACS Appl. Mater. Interfaces 8, 2486, (2016).
[10] Y.S. Jung, W. Jung, H.L. Tuller, and C.A. Ross, Nano Lett. 8, 3776, (2008).
[11] H.-H. Lu, C.-Y. Lin, T.-C. Hsiao, Y.-Y. Fang, K.-C. Ho, D. Yang, C.-K. Lee, S.-M. Hsu, and C.-W. Lin, Anal. Chim. Acta 640, 68 ,(2009).
[12] V. Postica, I. Hölken, V. Schneider, V. Kaidas, O. Polonskyi, V. Cretu, I. Tiginyanu, F. Faupel, R. Adelung, and O. Lupan, Mater. Sci. Semicon. Proc. 49, 20, (2016).
[13] F. Röck, N. Barsan, and U. Weimar, Chem. Rev. 108, 705, (2008).
[14] Y. Huang, X. Duan, Y. Cui, L.J. Lauhon, K.-H. Kim, and C.M. Lieber, Science 294, 1313, (2001).
[15] Y. Hu, J. Zhou, P.-H. Yeh, Z. Li, T.-Y. Wei, and Z.L. Wang, Adv. Mater 22, 3327, (2010).

[16] R. Khan, H.W. Ra, J.T. Kim, W.S. Jang, D. Sharma, and Y.H. Im, Sens. Actuators B 150, 389, (2010).
[17] O. Lupan, V. Postica, T. Pauporté, and R. Adelung, Sens. Actuators B in progres, (2017).
[18] T. Pauporté, O. Lupan, J. Zhang, T. Tugsuz, I. Ciofini, F. Labat, and B. Viana, ACS Appl. Mater. Interfaces 7, 11871, (2015).
[19] F. Yang, S.-C. Kung, M. Cheng, J.C. Hemminger, and R.M. Penner, ACS Nano 4, 5233, (2010).
[20] Y. Xiong, J. Chen, B. Wiley, Y. Xia, Y. Yin, and Z.-Y. Li, Nano Lett. 5, 1237, (2005).
[21] J.B. Baxter, A.M. Walker, K.v. Ommering, and E.S. Aydil, Nanotech. 17, S304, (2006).
[22] O. Lupan, T. Pauporté, B. Viana, P. Aschehoug, M. Ahmadi, B.R. Cuenya, Y. Rudzevich, Y. Lin,and L. Chow, Appl. Surf. Sci. 282, 782, (2013).
[23] Z.L. Wang and J. Song, Science 312, 242, (2006).
[24] Y.-I. Chou, C.-M. Chen, W.-C. Liu, and H.-I. Chen, IEEE Electron Device Lett. 26, 62, (2005).
[25] C.-F. Chang, T.-H. Tsai, H.-I. Chen, K.-W. Lin, T.-P. Chen, L.-Y. Chen, Y.-C. Liu, and W.-C. Liu, Electrochem. Commun. 11, 65, (2009).
[26] K. Skucha, Z. Fan, K. Jeon, A. Javey, and B. Boser, Sens. Actuators B 145, 232, (2010).
[27] S.-Y. Chiu, H.-W. Huang, T.-H. Huang, K.-C. Liang, K.-P. Liu, J.-H. Tsai, and W.-S. Lour, Int. J. Hydrogen Energy 34, 5604, (2009).
[28] T.-Y. Wei, P.-H. Yeh, S.-Y. Lu, and Z.L. Wang, J. Am. Chem. Soc. 131, 17690, (2009).
[29] Y.M. Wong, W.P. Kang, J.L. Davidson, A. Wisitsora-at, and K.L. Soh, Sens. Actuators B 93, 327, (2003).
[30] N. Yamazoe, Sens. Actuators B 5, 7, (1991).
[31] A. Kolmakov, D.O. Klenov, Y. Lilach, S. Stemmer, and M. Moskovits, Nano Lett. 5, 667, (2005).
[32] P. Scherz, Practical electronics for inventors, McGraw-Hill, Inc.; 2006.
[33] S. Bai, W. Wu, Y. Qin, N. Cui, D.J. Bayerl, and X. Wang, Adv. Funct. Mater. 21, 4464, (2011).
[34] X. Liu, L. Gu, Q. Zhang, J. Wu, Y. Long, and Z. Fan, Nature Commun, 5, (2014).

WATER AS A NANOSTRUCTURED MATERIAL

V. V. Sergentu[1], V. Prilepov[2], V. Zalamai[1], and P. Gashin[2]

[1]*Institute of Applied Physics, Academy of Sciences of Moldova, Academiei str. 5, Chisinau, MD-2028 Republic of Moldova;*
[2]*State University of Moldova, A. Mateevici str. 60, Chisinau, MD-2009 Republic of Moldova*
*E-mail: *vsergentu@yahoo.com*

(Received October 7, 2016)

Abstract

A nanostructured disordered ice *Ih* fraction in a water environment is theoretically investigated. The disordered ice fraction is taken into account as a nanocomposite consisting of a substance and a vacuum. The pattern of interaction between electrical charges considerably changes and thus leads to the formation of stable ice clusters that are consolidated by bound charges.

1. Introduction

Since ancient times, water has been one of the main resources of the mankind [1]. At the same time, the physical and biological properties of water should be the subject of further intensive scientific researches. There are a number of properties that are still poorly understood by modern science. Some of them refer to issues related to the existence of properties of "activated" water [2–5].

Paper [6] describes the method of obtaining nanostructured thin films based on vanadium. It was shown in [7] that these films exhibit specific physical and biophysical properties. Particularly, the effect of electrochemical transformation (activation) of distillated water during interaction with a thin nanostructured film (thickness of ~10 nm), which is a process similar to the contactless transformation of water in the high-frequency microwave range, was described [3].

Numerous experiments and theoretical investigations [4, 5] proved that water is not a homogeneous amorphous medium even in a standard environment. Together with the fraction which is usually identified as "ordinary water" H_2O, it contains a fraction which will be referred to as "liquid ice". At the microscopic level, it is similar to ice; however, it probably exhibits an amorphous disordered pattern (Figs. 8.7 in [4]).

We shall do our best to prove that, in liquid ice, the pattern of interaction between electric charges substantially changes; this effect leads to the existence of stable liquid ice clusters in the volume of ordinary water clusters having a special structure that is responsible for unusual physical and biophysical properties of the activated water containing these clusters.

The liquid ice medium in the form a system of structured elements of hydrogen and oxygen atoms dipped into a vacuum and arranged in a disordered amorphous system was considered. The average size of this element is a = 0.7 nm. Comparison of the thicknesses of ice

and water reveals that a portion of vacuum (intrinsic molar volume) in the liquid ice system is not smaller than $c \approx 0.09$. (916.7 vs. 999.8 kg/m^3 at $T = 0$°C). At the same time, in ordinary water, a portion of vacuum (c_W) can be assessed only indirectly on the basis of either theoretical or experimental data. For instance, it can be estimated on the magnitude of the parameter *b* from the van der Waals equation. However, these data are several times overvalued.

We believe that we should take into account the values of $c_W \approx 0.01 << c$ for water [8]. This estimate does not include the areas of empty spaces between the water molecules that cannot be reached by any experimental techniques. In our further evaluations, we consider that ordinary water, which incorporates these areas of empty spaces (unlike liquid ice), represents a nearly homogeneous medium.

In the conclusion of this section, we can note that all our last interpretations about space that cannot be reached by experimental techniques have respect only to physical particles of water (atoms). These conceptions involve electric fields for which the water volume is an ordinary nanocomposite of two dielectric media (vacuum and matter).

2. Results and discussion

2.1. Modified Coulomb law

We should take into account the space dispersion phenomenon in the systems including ice, while interpreting the processes involving electromagnetic waves [9]. In this section, we shall make use of a phenomenological approach based on the use of longitudinal dielectric function ε*(r)* of an inhomogeneous medium and try to make some conclusions on the basis of this approach. Equations (1)–(3) represent a reduced system of Maxwell's equations [10, 11] for an electric field that is constant in time and variable in space for a nonmagnetic medium with a spatial dispersion:

$$div(\vec{D}(\vec{r})) = \rho(\vec{r}), \tag{1}$$

$$rot(\vec{E}(\vec{r})) = 0, \tag{2}$$

$$\vec{D}(\vec{r}) = \varepsilon_0 \int d^3r' \varepsilon(\vec{r} - \vec{r}')\vec{E}(\vec{r}'), \tag{3}$$

where ρ(*r*) is the density of the external charges (free charges), $\vec{D}(\vec{r})$ is the induction, and $\vec{E}(\vec{r})$ is the electric field intensity. For simplicity, we shall assume that this description is appropriate if the characteristic length of the medium *L* is considered to be greater than or of the same order as structural elements $a \approx 0.7nm$. The longitudinal permittivity function is defined as

$$\varepsilon(\vec{r}) = \frac{1}{(2\pi)^{3/2}} \int d^3k \tilde{\varepsilon}(\vec{k}) \exp(i\vec{k}\vec{r}), \tag{4}$$

and the Fourier transform thereof is determined as follows:

$$\tilde{\varepsilon}(k) = (1/2\pi)^{3/2} \left[{\varepsilon_{eff}}^{-1} + \eta^{-1} k^2 / (k^2 - h^2) \right]^{-1}, \tag{5}$$

while regarding wave vector *h* of the ultrashort mode [12, 13] and dimensionless constants $\varepsilon_{eff} = \tilde{\varepsilon}(k \to 0)$ and η which depend on the type of the material as known magnitudes. The ultrashort modes can also be referred to as "dark modes" in accordance with the terminology used in [14].

With this choice of $\tilde{\varepsilon}(k)$ in (5), we must obey be the equality

$$\tilde{\varepsilon}(h_i) \equiv 0\,, \tag{6}$$

In fact, taking into account (2), we obtain the relationship

$$\vec{E}(\vec{r}) = -grad(\Phi(\vec{r}))\,, \tag{7}$$

which is afterwards substituted in (1). After having rewritten (1-3) in the form of (4) for Fourier transforms and on the basis of (5), we obtain

$$\varepsilon_0 \tilde{\Phi}(k) = \tilde{\rho}(k)\left[\varepsilon_{eff}{}^{-1}/k^2 + \eta^{-1}/(k^2 - h^2)\right]. \tag{8}$$

It follows from (8) that at $k = h$, a nontrivial solution for potential $\tilde{\varphi}(k) \neq 0$ of the electric field is possible even at zero values of $\tilde{\rho}(k) \equiv 0$ and this is a factual definition of ultra short mode *h*. The ε_{eff} magnitude can be determined employing the methods used in [15, 16]. As in our case, both components (the medium and the vacuum) penetrate the liquid ice medium without breaking down into isolated parts, we shall consider in our further estimations that

$$\varepsilon_{eff} = \varepsilon(1-c) + c\,, \tag{9}$$

where the magnitude of $\varepsilon \approx 90$ is almost equal to the relative dielectric constant of ice. The addition relationship

$$\eta^{-1} = \left[\varepsilon^{-1}(1-c) + c\right] - \varepsilon_{eff}^{-1} \tag{10}$$

makes it possible to obey the following condition: in the liquid ice medium, the Coulomb's law at utmost small distances, which are much smaller than the *a* magnitude, does not change in comparison with the ordinary ($G(r)_{r\to a} \to const/r$). Assuming that

$$\rho(\vec{r}) = \delta(\vec{r} - \vec{r}')\,, \tag{11}$$

we shall obtain the equation of the Green's function for system ($\delta(r)$–delta function). The Green's function for potential $G(\vec{r} - \vec{r}')$ is in fact an altered Coulomb law for the nanostructured medium

$$G(\vec{r} - \vec{r}') = \frac{1}{4\pi\varepsilon_0}\left[\frac{1}{\varepsilon_{eff}\,|\vec{r} - \vec{r}'|} + \frac{\cos(h\,|\vec{r} - \vec{r}'|)}{\eta\,|\vec{r} - \vec{r}'|}\right]. \tag{12}$$

To obtain the numerical value of *h*, it is necessary to carry out a separate investigation. The ordinary Coulomb law excludes the existence of mechanically stable states for any configurations and signs of electrical charges [17]. However, if the modified Coulomb law (12) is obeyed, a stable mechanical configuration is possible even for two classical particles regardless of the sign of their charges (see Fig. 1).

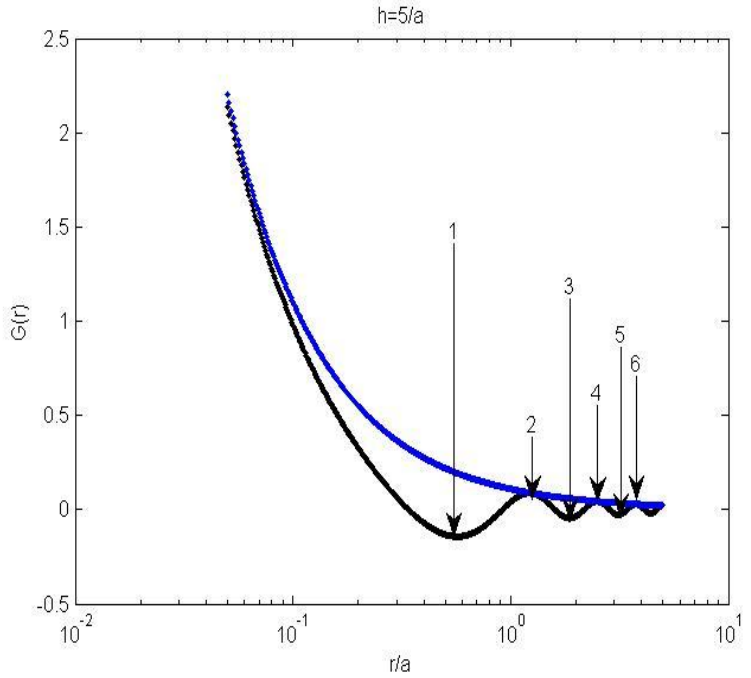

Fig. 1. Usual Coulomb law (blue) versus modified Coulomb law (black) for the potential of point charge. Arrows 1, 3, and 5 show equilibrium points for charges with the same sign. Arrows 2, 4, and 6 show equilibrium points for charges of different signs

The modified Coulomb law (12) consists of two components. They are independent of one another; each of the components makes a contribution in the formation of the general electric field

$$\Phi(\mathrm{r}) = \Phi^{(0)}(r) + \Phi^{(h)}(r)\,. \tag{13}$$

The first component is usual modes corresponding to solutions k≡0 from (8). An equation in coordinate representation can be written for this mode as follows:

$$\Delta\Phi^{(0)}(r) = 0\,. \tag{14}$$

The second component is “dark” modes with wave vector k=h≠0. Another equation can be written for these “dark” modes:

$$\Delta\Phi^{(h)}(r) + h^2\Phi^{(h)}(r) = 0\,. \tag{15}$$

At the same time, each mode has its own dielectric constant ($\varepsilon_{\mathrm{eff}}$, η).

2.2. Evaluation of the h magnitude

Let us try to estimate the *h* magnitude making use of the results of the study of bidimensional periodical structures [12, 13]. Ultrashort modes have a form of one-dimensional structure; therefore, we shall make use of the idea of “channeling.” The gist of the matter is that, in three-dimensional crystals, the channeling of radiation, which is a directed movement of radiation along certain directions in crystalline structures, takes place [18]. Actually, in a three-dimensional system, modes of smaller dimension appear. Thus, under certain conditions, a three-dimensional crystal may behave as a two-dimensional pore system with cylindrical "channels" (or pores) along which the channeling process takes place. The quantity of directions (channels) along which channeling takes place depends on the type of crystalline structure. We shall

estimate the h magnitude for three-dimensional spatial structures assuming that a three-dimensional ultra short mode can be represented in the form of an ultrashort (dark) mode of the type [12, 13]. Then the wave vector of the ultrashort mode can be evaluated making use of formula (22) from [12] where a portion of the vacuum is determined from formula $c = \pi R_{por}/a^2$. Now, the formula for c still has parameters which can be similarly applied both for the case of a bidimensional porous system from [12, 13] and for a three-dimensional porous structure, which is of particular interested to us. It is evident that the h magnitude changes within large limits as a portion of vacuum in the system c changes from 0 to 1. More precise numerical estimates can be done on the basis of graphs from [12, 13]. We can see that there are several branches with different numerical values. From (22) of [12], it is believed that

$$h \approx 5/a. \tag{16}$$

For other branches, $h >> 1/a$. Conditions for validity of the conception of medium homogeneity for dielectric materials, such as ice and water, are broken in this case for characteristic sizes $L = 2\pi/h$.

The ordinary water included regions of empty space $c_w \approx 0.01 << c$; according to (16), $h >> 1/a$ at $L << a$. Therefore, in further calculations, we believe that dark modes are absent in ordinary water in contrast to liquid ice.

2.3. Properties of the cluster

Taking into account a spherical cluster of radius R (volume $V = 4\pi R^3/3$) from liquid ice surrounded by ordinary water. A spherically symmetrical electrical field in liquid ice is described as (13). Usual boundary conditions should be resolved for the general solution including the modes of both types (13–15) in a cluster border.

Since the system as a whole is electrically neutral, the solution of equation (14) is trivial in ordinary water at $r > R$ and it is $\Phi(r) \equiv 0$.

The electric field configuration inside the neutral and spherically symmetric cluster of liquid ice at $r < R$ will be foliated and spherically symmetric with $\approx 2\pi/h$-thick layers; it will be given by formula

$$\Phi(r) = \Phi_0[1-(J_{0.5}(rh)\sqrt{R})/(J_{0.5}(Rh)\sqrt{r})], \tag{17}$$

where $R = x/h$ ($x = \pi(0.5+N) + 1/(\pi(0.5+N)) + O(1/N^2)$ is a nonzero root of the equation $d[J_{0.5}(x)/\sqrt{x}]/dx = 0$, $N = 1,2,3...$). For convenience, we shall write out the average intensity of the squared electrical field in the cluster with an accuracy up to members on the order of $1/hR$:

$$< \vec{E}^2 >= \overline{E}^2 = \frac{1}{V}\int_V d^3r(\nabla\Phi)^2 = 3(\Phi_0 h)^2\left[1+O\left(\frac{1}{hR}\right)\right]. \tag{18}$$

The numerical value of Φ_0 can be estimated on the basis of simple consideration. Ice is a solid matter that exhibits piezoelectric properties. Liquid ice can be considered as an ordinary ice that has undergone a strong inhomogeneous deformation; therefore, the coefficient of relative deformation is on the order of $\overline{\xi} = 0.02$. The deformation transforms ice into a disordered state and simultaneously generates an electrical field (18). Since this deformation is accompanied by electrification, an average value of electrical field is as follows:

$$\overline{E} = \overline{\xi}K/\varepsilon\varepsilon_0 \ , \tag{19}$$

where K is the piezoelectric coefficient [19]. From (18) and (19), we obtain that

$$\Phi_0 = \frac{\bar{\xi} K}{\sqrt{3} h \varepsilon \varepsilon_0} = 8 \cdot 10^{-4} V < k_B T / e \,. \tag{20}$$

where $K = 0.5$ C/m^2, $\varepsilon = 100$.

Equation (25) suggests that the depth of the potential well cluster is less than Boltzmann energy $k_B T$ and can serve as a small trap for ions of different types.

Let us consider the mechanical stability of liquid ice clusters under the influence of pressure exerted by ordinary water. The density of the electric energy of the cluster that restrains the external pressure of the surrounding ordinary water is

$$U_c = (\varepsilon_0 / 2V) \int_V d^3 r d^3 r' \vec{E}(\vec{r}) \varepsilon(\vec{r} - \vec{r}') \vec{E}(\vec{r}') \,. \tag{21}$$

We shall represent (5) in the form of two summands:

$$\tilde{\varepsilon}(k) = \tilde{\varepsilon}^{(1)} + \tilde{\varepsilon}^{(2)}(k) \,. \tag{22}$$

Then

$$U_c = U_c^{(1)} + U_c^{(2)} \,, \tag{23}$$

where

$$\tilde{\varepsilon}^{(1)} = \tilde{\varepsilon}(k \to \infty) = (1/2\pi)^{3/2} \left[\varepsilon_{eff}^{-1} + \eta^{-1} \right]^{-1} , \tag{24}$$

$$U_c^{(1)} = (2\pi)^{3/2} (\varepsilon_0 / 2V) \tilde{\varepsilon}^{(1)} \int_V d^3 r \vec{E}(\vec{r})^2 = (\varepsilon_0 / 2) \left[\varepsilon_{eff}^{-1} + \eta^{-1} \right]^{-1} (\Phi_0 h)^2 \left[1 + O(1/hR) \right] . \tag{25}$$

The second summand from (23) can be presented in the form of:

$$U_c^{(2)} = (\varepsilon_0 / 2V) \int d^3 k \, | \vec{\mathrm{H}}(\vec{k}) |^2 \, \tilde{\varepsilon}^{(2)}(\vec{k}) \,, \tag{26}$$

where

$$\begin{aligned} &\tilde{\varepsilon}^{(2)}(k) = \tilde{\varepsilon}(k) - \tilde{\varepsilon}(k \to \infty) = \\ &= (1/2\pi)^{3/2} \left[\varepsilon_{eff}^{-1} + \eta^{-1} \right]^{-1} \{ \left[\varepsilon_{eff}^{-1} + \eta^{-1} \right]^{-1} - 1 \} \frac{h^2}{k^2 - h^2 \left[\varepsilon_{eff}^{-1} + \eta^{-1} \right]^{-1}} \,, \end{aligned} \tag{27}$$

$$\begin{aligned} &\vec{\mathrm{H}}(\vec{k}) = \frac{1}{(2\pi)^{3/4}} \int_V d^3 r \exp(i\vec{k}\vec{r}) \nabla \Phi(\vec{r}) = \\ &= -2(2\pi)^{1/4} i\vec{k} \Phi_0 \left[\frac{\sin(kR)}{k^3} - \frac{\cos(kR)}{k^2} R \pm \frac{R}{2k \sin(hR)} \frac{\sin[(k \pm h)R]}{(k \pm h)} \right] . \end{aligned} \tag{28}$$

The dependence of electric energy density of the cluster on the radius and other parameters should be determined from formulas (21)–(28). It follows from (21)–(28) that, if the cluster radius is $R \approx 5a$, then

$$U_c / \varepsilon_0 (\Phi_0 h)^2 \approx -3 \cdot 10^2 \,. \tag{29}$$

We obtain from (25) that

$$| U_c | V \approx 3 c p V \,, \tag{30}$$

where $p = 10^5$ Pa is the pressure of the ordinary water surrounding the cluster (1 atm at $T = 273$ K).

The right-hand side of (30) is equal to the work required for cluster elimination by squeezing external pressure. The left-hand side of Eq. (30) is equal to the potential electric energy of the cluster that provides its mechanical stability.

Thus, we can affirm that modified Coulomb law (12) provides the mechanical stability of the cluster due to electrical forces arisen between bounded charges. Estimates show that the resonance frequency of cluster vibrations can achieve the microwave frequency range [3].

3. Conclusions

The experimental and theoretical investigations suggest the following. Water can form stable nanoclusters of fraction *Ih* consolidated by bounded electric charges. Their existence can serve as the basis for the manifestation of unusual physical and biophysical properties of water.

References

[1] Water for People, Water for Life, The United Nations World Water Development Report, URL: http://unesdoc.unesco.org/images/0012/001295/129556e.pdf.
[2] I. V. Smirnov, V. I. Vysotskii, and A. A. Kornilova, Introduction to the Biophysics of Activated Water, Universal Publishers, Boca Raton, Florida, USA, 2005.
[3] V. G. Shironosov, Rezonans v fizike, himii i biologii, Izhevsk, Udmurt University, 2000, p. 92.
[4] Eugene A. Sharkov, Passive Microwave Remote Sensing of the Earth: Physical Foundations, Springer, Florida, USA, 2005.
[5] S. D. Zakharov and I. V. Mosyagina, Klasternaja struktura vody, (review), FIAN, Preprint, Moscow, 2011.
[6] V. Prilepov, P. Gasin, A. Chirita, V. Midoni, D. Spoiala, and P. Ketrush, Journal of Optoelectonics and Advansed Matherials, 16 (1–2) 227, (2014).
[7] V. Prilepov, P. Gasin, I. Prilepov, V. Midoni, A. Chirita, D. Spoiala, and P. Ketrush, Optoelectron, Adv. Mater. Rapid Commun, 8 (1–2), 164, (2014).
[8] Yizhak Marcus, Ions in Water and Biophysical Implications From Chaos to Cosmos, Springer, 2012.
[9] G. S. Bordonskii, Phys. Solid State, 47 (4), 715, (2005).
A. V. Klyuev, I. A. Ryzhkin, M.I.Ryzhkin, JETP Letters, 100(9), 604, (2015).
[10] J. D.Jackson, Classical Electrodynamics Wiley, New York, 1998.
[11] L. D. Landau, E. M. Lifshitz, and L. P. Pitaevski: Electrodynamics of Continuous Media, Pergamon, Oxvord, 1984.
[12] Vladimir V. Sergentu, Veaceslav Ursaki, and Lilian Sirbu, Phys. Status Solidi B, 1–6, (2013).
[13] V. V. Sergentu and M. Olednic, Proc. of the 2nd Int. Conf. on Nanotechnologies and Biomedical Engineering, Chisinau, April 18–20, 363, 2013.
[14] Mark I. Stockman, Sergey V. Faleev, and David J. Bergman, Phys. Rev. Lett. 87 (16), 167401, (2001).
[15] R. Landauer, AIP Conf. Proc. 40, 2, (1978).

[16] L. A. Golovan, V. Yu. Timoshenko, and P. K. Kashkarov, Usp. Fiz. Nauk, 177 (6), 619, (2007).
[17] W. Jones, Eur. J. Phys. l, 85, (1980).
[18] M. A. Kumakhov, Sov. Phys. Usp. 18, 203, (1975).
[19] Victor F. Petrenko, Electromechanical Phenomena in Ice, Hanover, 1996.

A COMPARATIVE STUDY OF PHOTOCONDUCTIVITY DECAY IN ZnO-BASED MSM STRUCTURES AND NANOWIRES

E. Rusu[1], V. Postolache[2], N. Curmei[1] and V. Ursaki[1]

[1]Institute of Electronic Engineering and Nanotechnologies "D. Ghiţu", Academy of Sciences of Moldova, Academiei str. 3, Chisinau, MD-2028 Republic of Moldova
E-mail: rusue@nano.asm.md
[2]National Center for Materials Study and Testing, Technical University of Moldova, bd. Stefan cel Mare 168, Chisinau, MD-2004 Republic of Moldova

(Received September 20, 2016)

Abstract

Comparative analysis of transient photoconductivity in ZnO-based MSM structures and nanowires is performed in this paper. The measurements are carried out at room temperature in ambient air. The mechanisms of photoconductivity decay are discussed taking into account the range of measured relaxation times. It is found that the photoconductivity decay is determined by bulk effects in MSM structures, while it is governed by surface states and surface band bending effects in networks of nanowires.

1. Introduction

The relaxation processes of photoconductivity (PC), especially the effects related to long-duration PC decay and persistent photoconductivity (PPC) can significantly affect the parameters of photodetectors, field effect transistors, gas sensors, and other devices in terms of their sensitivity, noise properties, dark level, and temporal characteristics. PPC effects can be caused by various factors, particularly defects with bistable character, such as DX [1, 2] or AX centers [3], microscopic inhomogeneity [4, 5], and other effects leading to the formation of potential barriers induced by random local potential fluctuations.

It is generally believed that the mechanism of PPC in moderately doped bulk semiconductors, such as III–V alloys, is due to the metastable behavior of DX centers with a large lattice relaxation following electron capture by the DX state.

The spatial separation of the photogenerated electrons and holes by macroscopic potential barriers can occur due to band bending around doping inhomogeneities, or at planar surfaces, interfaces, junctions, etc. Particularly, a microscopic inhomogeneity caused by impurity distribution is produced in highly doped compensated semiconductors. The mechanism with macroscopic potential barriers is also inherent in II–VI semiconductor alloys. In this case, the random local potential fluctuations are caused by compositional fluctuations.

It has been speculated that, in nanowires, for instance, in ZnO nanowires, PPC is caused by a strong surface band bending (SBB) effect instead of a bulk trap effect [6, 7]. ZnO has been shown to be a versatile material for sensor applications, particularly for a visible-blind ultraviolet (UV) sensor [8] suitable for both military and non-military applications [9]. ZnO nanowire-based photodetectors and optical switches are of particular interest [10, 11].

The goal of this paper is to perform a comparative study of PC decay in ZnO-based metal–semiconductor–metal (MSM) structures and nanowires and identify the mechanism of PC relaxation processes.

2. Sample preparation technique

To prepare MSM structures, ZnO films were deposited on *p*-type Si substrates by the spin-coating method. A chemical solution was prepared for these purposes by dissolving zinc acetate dihydrate [$Zn(CH3COO)_2$-H_2O] in 2-methoxyethanol at room temperature. Diethanolamine (DEA) was added to the initial mixture as a stabilizer. A solution composed of $InCl_3$ in 2-methoxyethanol was used for doping. The final mixture was subjected to ultrasound treatment at 50°C during 1 h until total homogenization.

The design of MSM optical sensors was produced by photolithography. The film was covered with a positive AZ5214E photoresist by spin coating and then exposed to radiation from a 250-W mercury lamp through masks for 60 s. In regions for metallic contacts, dissolution was performed in a NaOH solution with a concentration of 1% for 4 s.

Figure 1 shows the sequence of procedures for the production of MSM structures, including the deposition of a ZnO film on a Si substrate (Fig. 1a), a photoresist layer (Fig. 1b), the exposure of the photoresist through the mask with a required design (Fig. 1c), and the metallization of regions for electrical contacts in the inter-digital design of the device (Fig. 1d). Aluminum ohmic contacts were deposited on the surface of the ZnO layer by means of thermal vaporization in vacuum. The sample was heated to 100°C during metal deposition to improve the adhesion. The Al contacts were heated to 250°C for 30 min after removing the photoresist.

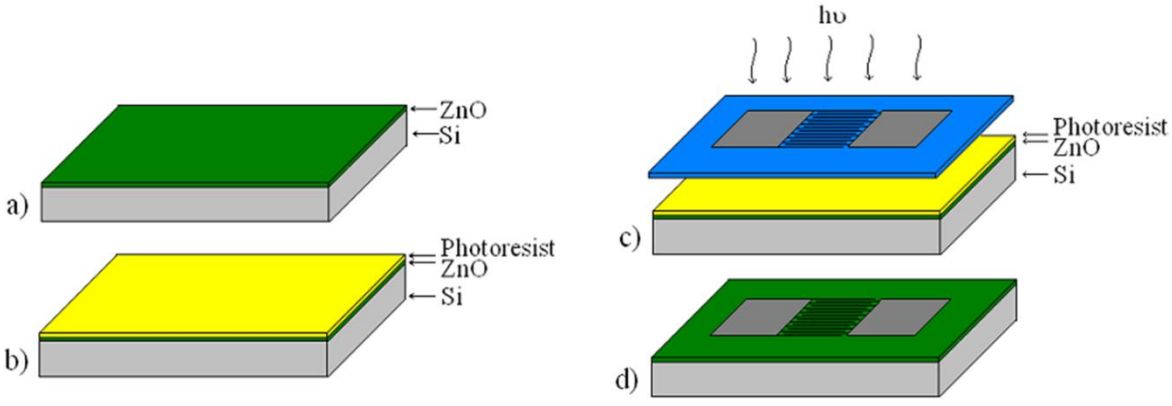

Fig. 1. Sequence of procedures for the production of MSM structures.

ZnO nanowires were prepared in a two-step technological route on the basis of Na-doped bulk ZnTe single crystals with a free hole concentration of 3×10^{18} cm^{-3}. A template of ZnTe nanowires with a mean diameter around 50 nm was produced in the first step by electrochemical treatment of ZnTe crystals as described elsewhere [12]. Anodic etching was conducted in an HNO_3 : HCl : H_2O electrolyte at a ratio of 5 : 20 : 100 at 25°C with the application of 0.3-s voltage pulses at a frequency of 1 Hz and an amplitude of 5 V. The ZnTe nanowires were

transformed into ZnO nanowires in the second step by thermal treatment. The morphology of the nanowires did not change during annealing at 500^{o}C, while the material was totally oxidized. Morphological and chemical composition microanalyses of the samples were conducted using a VEGA TESCAN TS 5130MM scanning electron microscope equipped with an Oxford Instruments INCA energy dispersive X-ray system. Figure 2 shows the design of the MSM structure and the morphology of the produced ZnO nanowires.

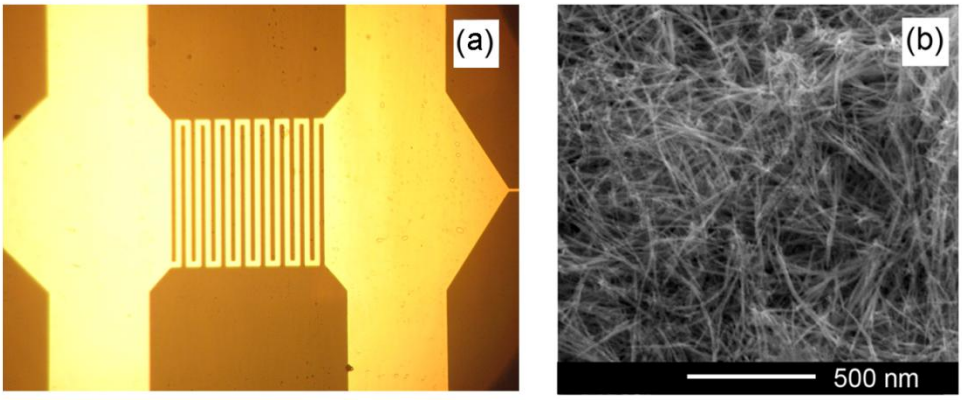

Fig. 2. Design of the MSM structure (a) and morphology of the produced ZnO nanowires (b).

3. PC relaxation in MSM structures and ZnO nanowires

The electrical contacts to samples for measuring PC were prepared using a conductive silver paste. Since the decay time is fairly long in a network of ZnO nanowires, a 366-nm excitation beam of an Hg arc lamp was mechanically shut in the PC relaxation experiments. The experiments were performed at room temperature in ambient air.

The current–voltage characteristics of the MSM structure exhibit an ohmic behavior (Fig. 3), which indicates that the contacts will have no effect on the current relaxation processes in MSM structures, the PC decay being related entirely to the bulk of the ZnO film.

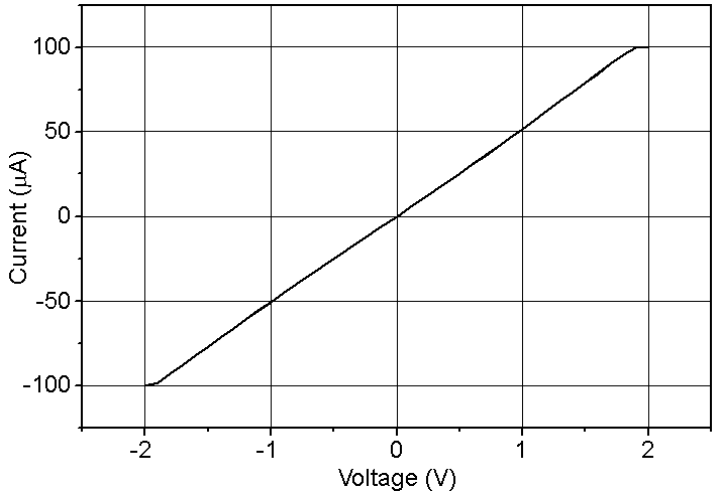

Fig. 3. Current–voltage characteristic of an MSM structure.

The PC decay in MSM structures is fairly fast (Fig. 4a); this feature indicates the predominance of bulk mechanisms, while the PC relaxation processes in nanowire samples have a different nature (Fig. 4b). First of all, the relaxation time is much longer than that for the SMS sample. This large relaxation time cannot be attributed to trapping effects of bulk centers. Models with microscopic (atomic) energy barriers at centers with large lattice relaxation, such as DX centers, have not been reported in ZnO either. On the other hand, the SBB effects are generally accepted as the origin for long relaxation times and PPC in ZnO nanowires [11, 13]. The fact that the shape of the relaxation curves in ZnO nanowires is not affected by a change in the applied bias and the polarity of the bias indicate that, similarly to MSM structures, there is no influence of contact effects.

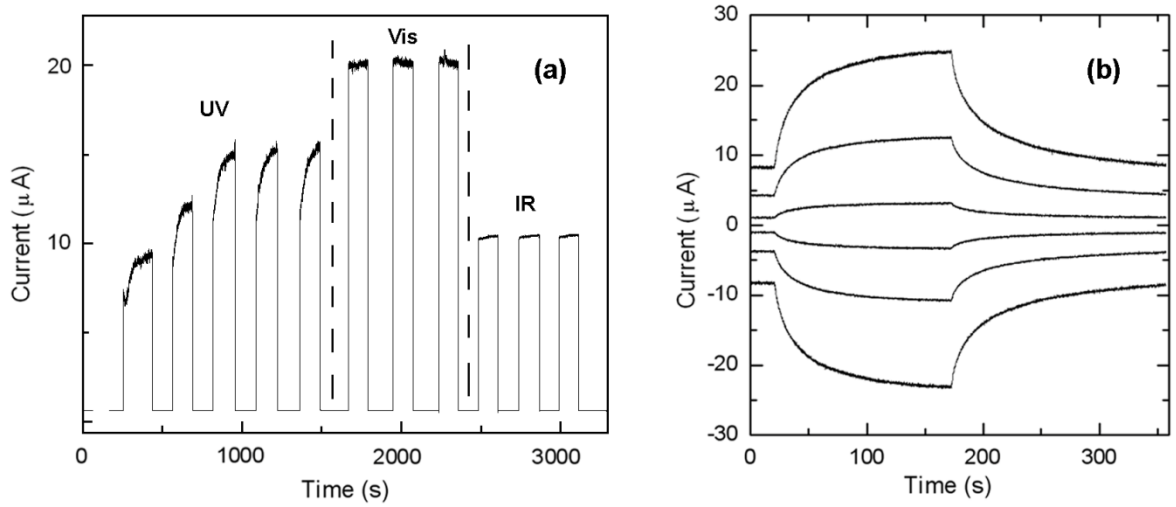

Fig. 4. PC build-up and decay measured at room temperature in a MSM photoconductor with excitation from different spectral ranges (a) and in ZnO nanowires (b) with UV radiation power density of 250 mW/cm^2 at different applied biases (from top to bottom, the curves were recorded at an applied external bias of 5, 3, 1, –1, –3, and –5 V, respectively).

Typically, wide bandgap metal oxide semiconductor nanostructures exhibit current sensitivity only in UV region [14, 15]. However, photodetection in a wide spectral range is of interest for many applications. The current switching behavior in Fig. 4a shows that the MSM structures exhibit strong photosensitivity in a wide spectral range from the UV to infrared (IR) wavelengths. ZnO nanomaterials typically exhibit photodetection in the range from UV to visible region. On the other hand, the prepared MSM structures show a switching behavior in the infrared region too. Therefore, they have a potential to be utilized as universal photodetector devices in contrast to common devices based on wide bandgap semiconductors. The fact that, in the prepared MSM samples, PC is induced not only by UV irradiation, but also by visible and near-infrared light irradiation can suggest the presence of a large amount of energy levels within the bandgap of ZnO films, and these energy levels can also form extended band-edge tails of the density of states, which generate electron–hole pairs by radiation with a large spectrum of wavelengths.

As concerns the ZnO nanowires, they are randomly oriented and the percolation, as deduced from Fig. 2b, provides a pathway of current through the nanowire network. The mechanisms of photoresponse in ZnO nanowires are commonly attributed to their huge surface-

to-volume ratio and to surface effects related to adsorption (in the dark) and desorption (under UV illumination) of oxygen molecules when measurements are performed in ambient air [16]. The adsorption of oxygen molecules to the ZnO nanowire surface in the dark results in capture of free electrons of the *n*-type semiconductor: $O_2(g) + e^- \rightarrow O_2^-(ad)$, which produces a depletion layer near the nanowire surface and upward band bending near the surface. The adsorption of oxygen molecules significantly reduces the conductivity of the nanowires due to the large surface-to-volume ratio. Electron–hole pairs are generated in ZnO under UV-light illumination with photon energy higher than the bandgap. Consequently, the holes migrate to the surface along the potential slope created by the band bending and recombine with O_2-trapped electrons. As a result of this recombination, oxygen is released from the surface according to the reaction $O_2^-(ad) + h+ \rightarrow O_2(g)$. On the other hand, the unpaired electrons contribute to the PC.

4. Conclusions

The results of this comparative study have shown different mechanisms of PC relaxation in ZnO-based MSM structures and nanowires. The PC relaxation is fairly fast in MSM structures, being determined by bulk effects in ZnO films. In ZnO nanowires, the PC relaxation is governed by surface effects, such as adsorption and desorption of oxygen molecules, SBB effect, recombination of photogenerated holes with electrons trapped at oxygen molecules, and contribution of photogenerated electrons to PC, which results in longer relaxation times and PPC. The spectral distribution of PC is also different in ZnO-based MSM structures and nanowires. In nanowires, PC is generated predominantly by the above bandgap radiation, while in MSM structures it is generated in a wider spectral range from UV to IR wavelengths, suggesting the presence of a large amount of energy levels within the bandgap of ZnO films which can also form extended band-edge tails of the density of states. Due to the wide spectral range of PC in ZnO-based MSM structures, they have a potential to be utilized as universal photodetector devices.

References

[1] D. V. Lang, R. A. Logan, and M. Jaros, Phys. Rev. B 19, 1015, (1979).
[2] J. Z. Li, J. Y. Lin, H. X. Jiang, M. A. Khan, and Q. Chen, J. Appl. Phys. 82, 1227, (1997).
[3] J. Z. Li, J. Y. Lin, H. X. Jiang, A. Salvador, A. Botchkarev, and H. Morkoc, Appl. Phys. Lett 69, 1474, (1996).
[4] H. J. Queisser, and D. E. Theodorou, Phys. Rev. B 33, 4027, (1986).
[5] H. X. Jiang, G. Brown, and J. Y. Lin, J. Appl. Phys. 69, 6701, (1991).
[6] H.-Y. Chen, R.-S. Chen, N. K. Rajan, F.-C. Chang, L.-C. Chen, K.-H. Chen, Y.-J. Yang, and M. A. Reed, Phys. Rev. B 84, 205443, (2011).
[7] C. Soci, A. Zhang, B. Xiang, S. A. Dayeh, D. P. R. Aplin, J. Park, X. Y. Bao, Y. H. Lo, and D. Wang, Nano Lett. 7, 1003, (2007).
[8] G. Goncalves, J. Non-Cryst. Solids 352, 1444, (2006).
[9] S. Hullavarad, N. Hullavarad, D. Look, and B. Claflin, Nanoscale Res Lett 4, 1421, (2009).
[10] J. B. K. Law, and J. T. L. Thong, Appl. Phys. Lett 88, 133114, (2006).
[11] C. Soci, A. Zhang, X.-Y. Bao, H. Kim, Y. Lo, and D. Wang, D., Nanotechnology 10, 1430, 2010.

[12] V. Zalamai, A. Burlacu, V. Postolache, E. V. Rusu, V. V. Ursaki, and I. M. Tiginyanu, Mold. J. Phys. Sci. 9, 308, (2010).
[13] D. Cammi, and C. Ronning, Adv. Cond. Matter Phys. 2014, 184120, (2014).
[14] D. Gedamu, D. et al., Adv. Mater. 26, 1541, (2014).
[15] H. Chen, L. Hu, X. Fang, and L. Wu, Adv. Funct. Mater. 22, 1229, (2012).
[16] Y. K. Mishra, Y. K. et al., ACS Appl. Mater. Interfaces **7,** 14303, (2015).

CONTROL OF MORPHOLOGY AND LUMINESCENSE OF NANOSTRUCTURED ZnO LAYERS FOR LASING APPLICATIONS

Alexandru Burlacu

Ghitu Institute of Electronic Engineering and Nanotechnology, Academy of Sciences of Moldova, str. Academiei 3/3, Chisinau, MD-2028 Republic of Moldova

E-mail: alexandru.burlacu@asm.md

(Received December 2, 2016)

Abstract

A comparative analysis of various technological methods for the preparation of nanostructured ZnO films is performed in this work to identify technologies suitable for the development of laser structures. It is shown that arrays of nanorods with a regular hexagonal geometry are readily produced by low-pressure chemical vapor deposition (CVD), chemical bath deposition (CBD), and electrochemical depositions (ECD) and these nanorods can play the role of resonators for guided modes. Irregular nanostructured layers with strong light scattering properties can be prepared by metal-organic chemical vapor deposition (MOCVD), aerosol spray pyrolysis, and by thermal treatment of ZnSe crystals. As concerns the optical quality necessary for stimulated emission and optical gain, low-pressure CVD and MOCVD are most suitable, while CBD and ECD can hardly provide the required quality for lasing action.

1. Introduction

There has been a steady increasing interest in optoelectronic applications of zinc oxide in the last decades [1–11] due to excellent semiconductor properties of this material, such as high electron mobility and thermal conductivity, good optical transparency, large bandgap (3.36 eV at room temperature), high exciton binding energy (60 meV), high optical gain, (320 cm^{-1} at room temperature), high damage threshold under strong excitations, and high resistance against radiation. These optoelectronic applications include photovoltaic cells, light emitting diodes, and lasers, detectors among others.

Another specific property of ZnO, which results from multiple changes in the growth directions of the wurtzite structure and high ionicity of polar surfaces [12, 13], is that it provides conditions for obtaining a large diversity of micro/nanostructures, such as nanowires, nanobelts, nanorings, nanospirals/nanobows, nanocombs, etc., many of which are suitable for designing lasers.

Therefore, nanostructured ZnO films produced by various technological methods provide conditions for lasing effects with different laser mode structures due to different resonator types, provided that the applied technologies ensure high optical quality of films in terms of optical gain, and high figure of merit of the produced resonators.

The goal of this paper is to perform a comparative analysis of the effect of technological conditions applied during the growth of nanostructured ZnO films by various technological

methods upon the morphology and luminescence properties of the produced films and identify which of them are most suitable for developing lasers.

2. Sample preparation and experimental details

Nanostructured ZnO films were produced by various technologies. Metal organic chemical vapor deposition (MOCVD) was performed in a horizontal double furnace set-up consisting of a source furnace and a main furnace as described elsewhere [14], with a zinc acetylacetonate material introduced into the source furnace. The vapors were transported into the main furnace by an Ar gas flow which was mixed with another flow of Ar and O_2 gases at the entrance of the main furnace. The morphology of ZnO structures produced by this method was determined by the ratio of the gas flow rates.

With chemical vapor deposition (CVD) procedure, ZnO nanowire films were grown on Si (100) substrates at a low pressure (a level of 5 Torr) in a two-zone quartz flow reactor [15, 16] with metallic zinc of high purity (99.999%) and an oxygen–argon mixture (15 vol % of oxygen) as starting reactants. In the first zone, zinc was evaporated; in the second zone, zinc vapors interacted with oxygen. An oxygen–argon mixture was fed to the reactor. The synthesis was conducted on substrates located in the second zone at different distances from the zinc source. ZnO nanowires were synthesized with high yield by controlling the flow rates and partial pressures of oxygen, argon, and zinc vapor. Growth of vertical nanowires started for a certain critical ratio of oxygen/zinc vapors. The shape and size of the ZnO nanowires/nanorods were found to depend on the position of the substrate in the growth zone.

With chemical bath deposition (CBD) method, the substrates were immersed in an aqueous solution bath comprising a mixture of saturated $ZnCl_2$ and concentrated NH_4OH [14, 17].

The reactions of the formation of complex Zn ions and their interaction with NH_4OH are as follows:

$$ZnCl_2{*}2H_2O+4H_2O \leftrightarrow Zn(H_2O)_6^{2+} + 2Cl^-$$
$$Zn(H_2O)_6^{2+} + 2NH_4OH \leftrightarrow Zn(OH)_2\downarrow + 2NH_4^+ + 6H_2O$$
$$Zn(OH)_2 + 4NH_4OH \leftrightarrow Zn(NH_3)_4^{2+} + 2OH^- + 4H_2O$$
$$Zn(NH_3)_4^{2+} + 2OH^- \leftrightarrow Zn(OH)_2\downarrow + 4NH_3\uparrow$$

The substrate with the deposited $Zn(OH)_2$ is calcinated at 250–300^{o}C for 2 h. ZnO nanorods are formed as a result of the reaction:

$$Zn(OH)_2 \rightarrow ZnO + H_2O.$$

Quasi-continuous and nanostructured ZnO layers were obtained by electrochemical deposition (ECD) using a zinc nitrate ($Zn(NO_3)_2$) solution with a concentration of 0.05–20 mM and hydrogen peroxide (H_2O_2) with a concentration of 0.1 M in an electrochemical cell with three electrodes: a metallic zinc or silicon working electrode, an Ag/AgCl reference electrode, and a platinum counter electrode. Aluminum nitrate ($Al(NO_3)_3$) was used for *n*-type doping. The following reactions occur with application of potential at the cathode:

$$NO_3^- + 2\ e^- + H_2O \rightarrow 2\ OH^- + NO_2^-$$
$$H_2O_2 + 2\ e^- \rightarrow 2\ OH^-$$
$$Zn^{2+} + 2\ OH^- \rightarrow Zn(OH)_2$$
$$Zn(OH)_2 \rightarrow ZnO + H_2O.$$

The conversion of zinc hydroxide to zinc oxide, which is deposited on the cathode (substrate), occurs at temperatures above 60°C.

Non-doped and In+N co-doped ZnO films were also prepared by aerosol spray pyrolysis with a special injector under the pressure of an oxygen flow with acetate dihydrate ($Zn(CH_3COO)_2{\cdot}2H_2O$) dissolved in ethylic alcohol. Doping with indium was performed by adding an indium nitrate ($In(NO_3)_3$) solution; doping with nitrogen was achieved by dissolution of ammonium acetate (CH_3COONH_4) stabilized by diethanolamine ($C_4H_{11}NO_2$).

Apart from that, a nanostructured ZnO material was prepared from bulk ZnSe single crystals by their transformation into ZnO by thermal treatment in oxygen ambient at different temperatures in a range of 600–800°C for 1 h.

The morphology and chemical composition microanalysis of samples were studied using a VEGA TESCAN TS 5130MM scanning electron microscope (SEM) equipped with an Oxford Instruments INCA energy dispersive X-ray (EDX) system.

The continuous wave (cw) photoluminescence (PL) was excited by the 351.1-nm line of an Ar^+ SpectraPhysics laser and analyzed with a double spectrometer providing a spectral resolution better than 0.5 meV. The samples were mounted on the cold station of a LTS-22-C-330 optical cryogenic system.

The lasing characteristics of the produced ZnO structures were measured at 10 K in a He-flow cryostat under the pumping by the third harmonic of a Q-switched Nd:YAG laser (355 nm, 10 ns, 10 Hz). The spectra were recorded by a CCD matrix covering a wavelength interval of 40 nm with the dispersion of about 0.04 nm/px.

3. Results and discussion

The MOCVD process usually produces a ZnO film consisting of nanorods with the morphology illustrated in Fig. 1a. The nanorods are arrow-headed with a mean diameter of 200–400 nm. On the other hand, hexagonal ZnO nanorods with a narrow size distribution centered at a diameter of 300 nm are produced with low pressure CVD growth as deduced from analysis of the SEM image in Fig. 1b. The array of nanorods is highly oriented perpendicular to the substrate surface. Arrays of hexagonal ZnO nanorods are also produced by CBD (Fig. 1c) and ECD (Fig. 1d) technologies. A film with a more complex structure consisting of large building blocks, which are nanostructured in turn, is usually produced by aerosol spray pyrolysis as shown in Fig. 1e. As mentioned above, a nanostructured ZnO material with the morphology illustrated in Fig. 1f is obtained by annealing bulk ZnSe single crystals in oxygen ambient.

Analysis of these morphologies in the context of possible laser resonators suggests that arrays of hexagonal nanorods shown in Figs. 1b–1d could sustain laser modes inherent in classical resonators, such as Fabry–Perot (FP) cavities satisfying the following relation [18]:

$$\Delta\lambda = \frac{1}{L}\left[\frac{\lambda^2}{2}\left(n - \lambda\frac{dn}{d\lambda}\right)^{-1}\right]$$

where $\Delta\lambda$ is the wavelength difference for two neighboring modes, L is the resonator length (nanorod length in our case), and n is the refraction index of ZnO, or guided modes resulting from solving the Helmholtz equation for the magnetic field eigenmodes **H**(x,y) and eigenvalues $n_{eff}k_0=\beta$:

$$\nabla\times(\nabla\times H) - n_{eff}^2 k_0^2 H = 0$$

where n_{eff} is the effective refractive index, k_0 is the vacuum wave vector, and β is the propagation constant [19]. On the other hand, the films with morphologies shown in Figs. 1a, 1e, and 1f can most probably sustain random lasing.

Conventional lasing due to FP cavities is unlikely to occur in ZnO nanorods illustrated in Fig. 1a due to the sharp top surface of the ZnO nanorods with large optical loss and an insufficient optical gain in short nanorod with a length of about 1 μm. The arrow-headed ZnO nanorods are not expected to support guided lasing modes either because of their geometrical shape and the wavy form of their surface, which leads to significant light scattering and large optical losses [20]. On the other hand, a random laser does not require a regular cavity; instead, it depends on the scattering properties of the material. It is also hardly expected to find classical regular resonators in layers with the morphology shown in Fig. 1e. On the other hand, strong light scattering is readily provided by this morphology, which is a mandatory condition for random lasing. Conditions for random lasing are most probably fulfilled also in structures produced by annealing of bulk single crystalline ZnSe, which leads to the formation of a uniform nanostructured material with the mean grain size of 100–200 nm as shown in Fig. 1f [21]. Therefore, random laser action is possible in all types of ZnO layers with the morphology shown in Figs. 1a, 1e, and 1f.

In nanorods with a regular hexagonal structure, guided modes can easily propagate and the mode structure can be controlled by changing the geometrical parameters of nanorods as demonstrated in Fig. 2 for ZnO films produced by low-pressure CVD. The size of nanowire/nanorods produced by this technology was found to depend on the O/Zn precursor ratio during growth, which in turn is determined by the position of the substrate in the growth zone [22]. Figure 2a shows that high densities of nanorods with a diameter of 300 nm grow over the ZnO seed layer on a Si substrate positioned at the entrance of the growth zone (higher O/Zn ratio). On the other hand, ZnO nanowires with a diameter of 50–100 nm grow on substrates placed at the exit of the zone (lower O/Zn ratio). The average length of the nanorods/nanowires is about 5 μm.

The morphology of ZnO films produced by ECD can also be controlled by the technological conditions as shown in Fig. 3. Particularly, the density of ZnO nanorods on the substrate depends on the supersaturation level with precursors and on the rates of their refreshing. At high supersaturation levels, a high density of nanorods is produced, which coalesce to form a quasi-continuous film (Fig. 3b). The shapes and sizes of nanorods are also affected by the voltage applied during ECD. Hexagonal nanorods are obtained at an applied voltage of 1.7 V with respect to the reference electrode (Fig. 3a), while arrow-headed nanorods similar to those grown by MOCVD are produced at an applied voltage of 1.8 V (Fig. 3c).

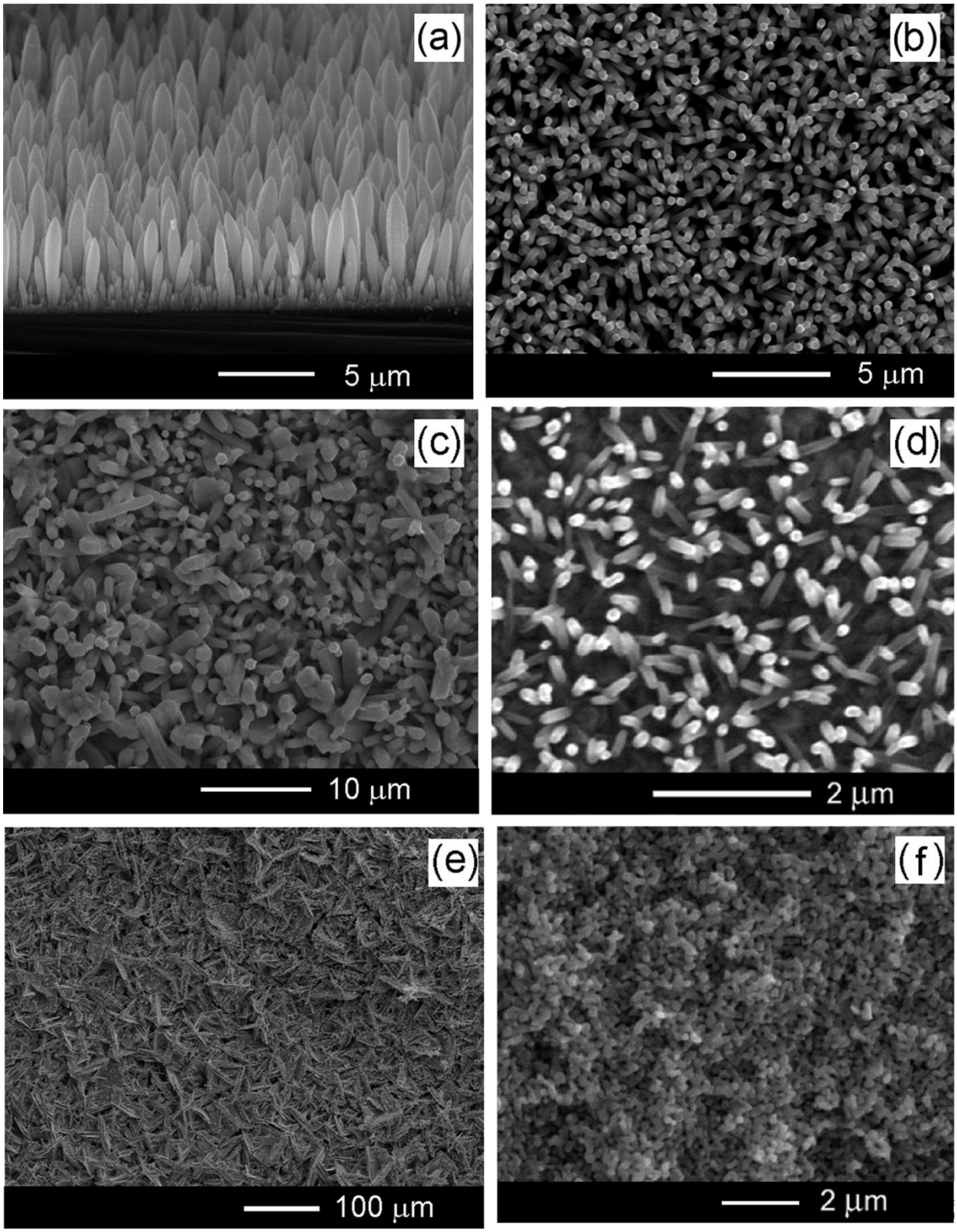

Fig. 1. SEM images of ZnO films produced by various technologies: (a) MOCVD, (b) low-pressure CVD, (c) CBD, (d) ECD, (e) aerosol spray pyrolysis, and (f) thermal treatment of bulk ZnSe.

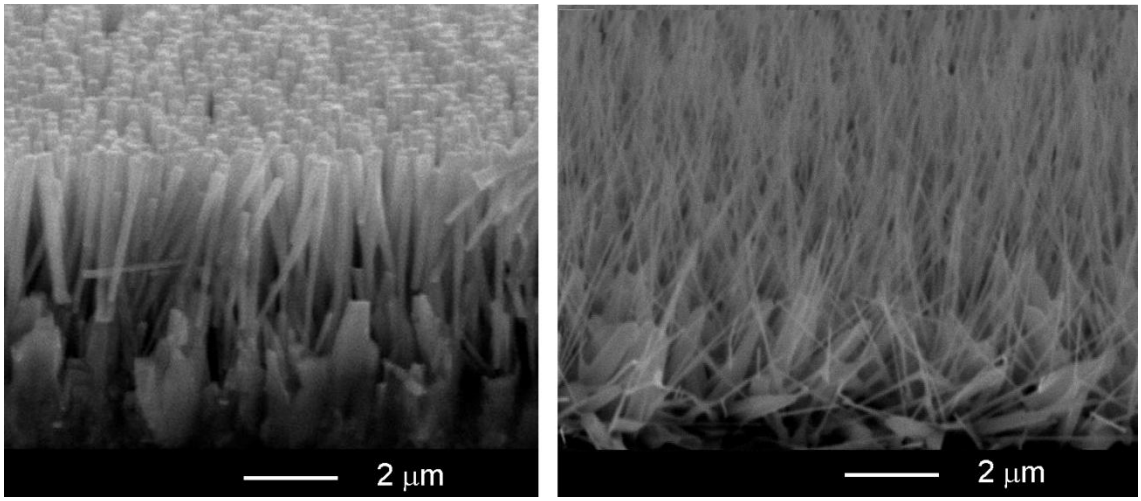

Fig. 2. Tilted SEM view of ZnO nanorods produced by low-pressure CVD with (left) a high and (right) low O/Zn ratio.

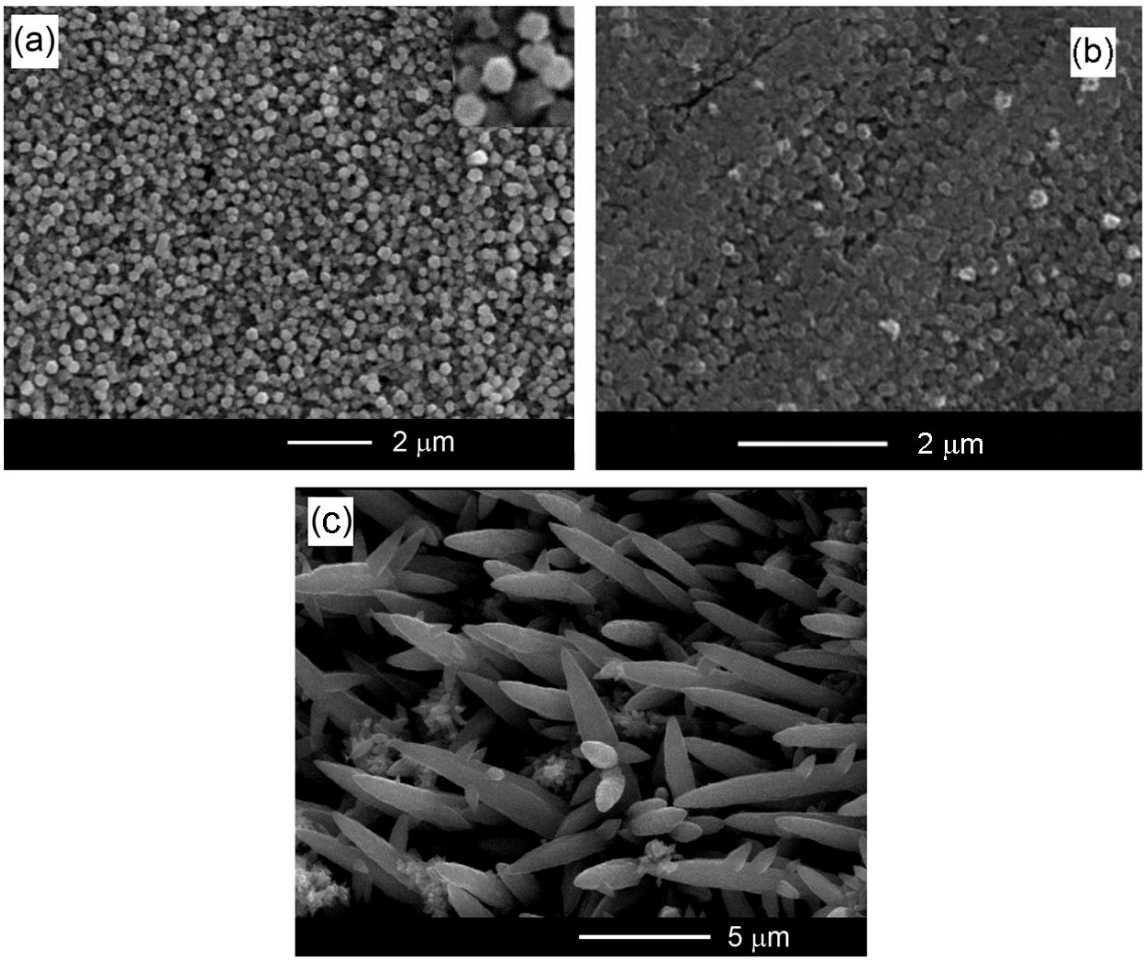

Fig. 3. SEM view of ZnO films produced by ECD with an applied voltage of (a, b) 1.7 and (c) 1.8 V (Ag/AgCl). The concentration of precursors is moderate in (a) and (c) and high in (b).

Apart from high figure of merit resonators, high optical quality of ZnO structures is necessary to provide stimulated emission and laser action. The cw PL characterization revealed the high optical quality of the ZnO structures produced by MOCVD (Fig. 4a) and low-pressure CVD (Fig. 4b). The PL spectrum is dominated by the recombination of donor bound excitons D^0X with phonon replica, along with free exciton FX emission and a band due to the donor acceptor pair recombination DA, the D^0X luminescence in films grown by low-pressure CVD being determined by the I_1, I_4, and I_6 lines [23]. The intensity of the DA luminescence is more than two orders of magnitude lower than the D^0X luminescence. The samples grown by aerosol spray pyrolysis and those produced by thermal treatment of bulk ZnSe also exhibit fairly high optical quality, the PL spectrum being dominated by the recombination of D^0X excitons in the case of the material produced from ZnSe crystals (Fig. 4f) and by the recombination of acceptor-bound excitons A^0X in films prepared by aerosol spray pyrolysis and co-doped by In and N (Fig. 4e).

The samples prepared by the CBD and ECD methods exhibit luminescence properties (Figs. 4c and 4d) different from those of the samples prepared by MOCVD and low-pressure CVD. The low-temperature luminescence intensity in these samples is three orders of magnitude lower, and the PL intensity decreases as little as by a factor of 5 with an increase in temperature to 300 K (not shown here), as compared to the three orders of magnitude decrease in the PL intensity with the same temperature increase in the samples prepared by MOCVD and low-pressure CVD. This observation is indicative of the different natures of electronic transitions responsible for near-band-edge luminescence in the samples prepared by MOCVD or low-pressure CVD on the one side and those prepared by CBD or ECD on the other side. A characteristic feature of the near-bandgap PL band in the samples prepared by CBD and ECD is the broadening towards the Stokes part of the emission. It has been previously shown that the broadening of the PL band involved can be accounted for by the broadening of the band edges due to the potential fluctuations induced by the high concentration of intrinsic defects or impurities [24, 25], and this broadening is a measure of sample doping with impurities.

Apart from the control of morphology by adjusting the technological parameters in the ECD process, the electrical parameters of the deposited films can be controlled by doping with donor impurities, for instance, with aluminum, as described above. The degree of doping with Al, and accordingly the electron concentration, can be monitored by investigating the width of the PL band. Figure 5a presents PL spectra of ZnO films doped with Al from solutions with various concentration of aluminum nitrate (increasing from 1 to 4). The width of the PL band increases from 28 to 155 meV with increasing degree of doping. By using the previously determined dependence of the PL band width on the free electron concentration in ZnO films [26] as a calibration curve, one can estimate that the electron concentration increases from 1.2×10^{19} cm^{-3} in sample #1 to 2.7×10^{20} cm^{-3} in sample #4.

Electrical parameters of the deposited films can also be controlled by doping in an aerosol spray pyrolysis process. The PL spectra presented in Fig. 5b suggest that p-type conductivity can be obtained in ZnO films doped with nitrogen as described above. It is evident that the PL spectrum of a specially undoped sample is dominated by the luminescence at 3.360 eV coming from the recombination of excitons bound to a residual donor impurity, while the spectrum of the sample doped with N is dominated by a PL band at 3.349 eV related to the recombination of acceptor bound excitons [1], most probably of excitons bound to the N acceptor. This assumption was also confirmed by thermoelectric voltage experiments. The possibilities of obtaining films with *p*-type conductivity are especially important for the development of an electrically pumped laser.

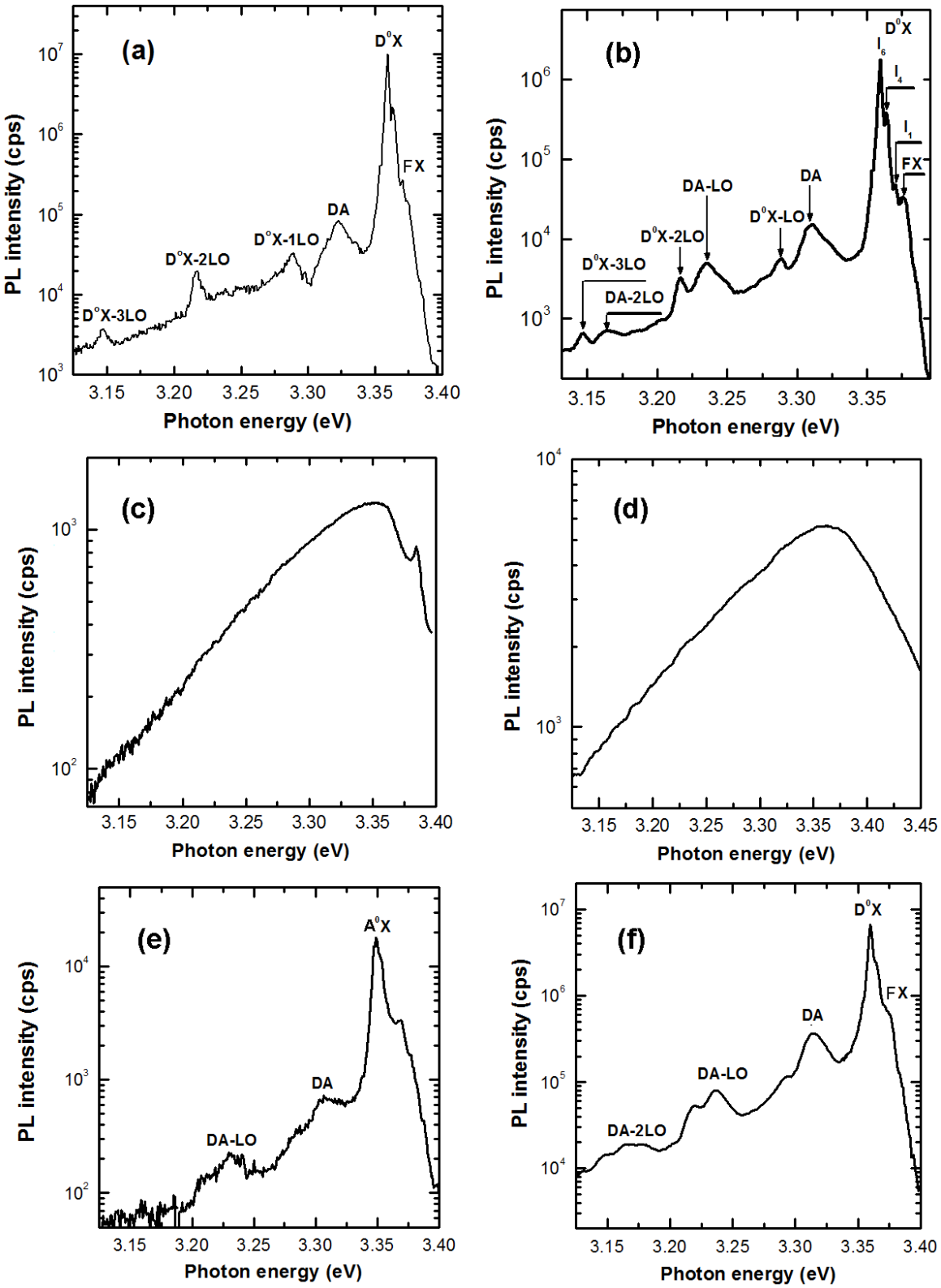

Fig. 4. Typical cw PL spectrum of the ZnO material produced by (a) MOCVD, (b) low-pressure CVD, (c) CBD, (d) ECD, (e) aerosol spray pyrolysis, and (f) thermal treatment of bulk ZnSe. The spectra are measured at T = 10 K.

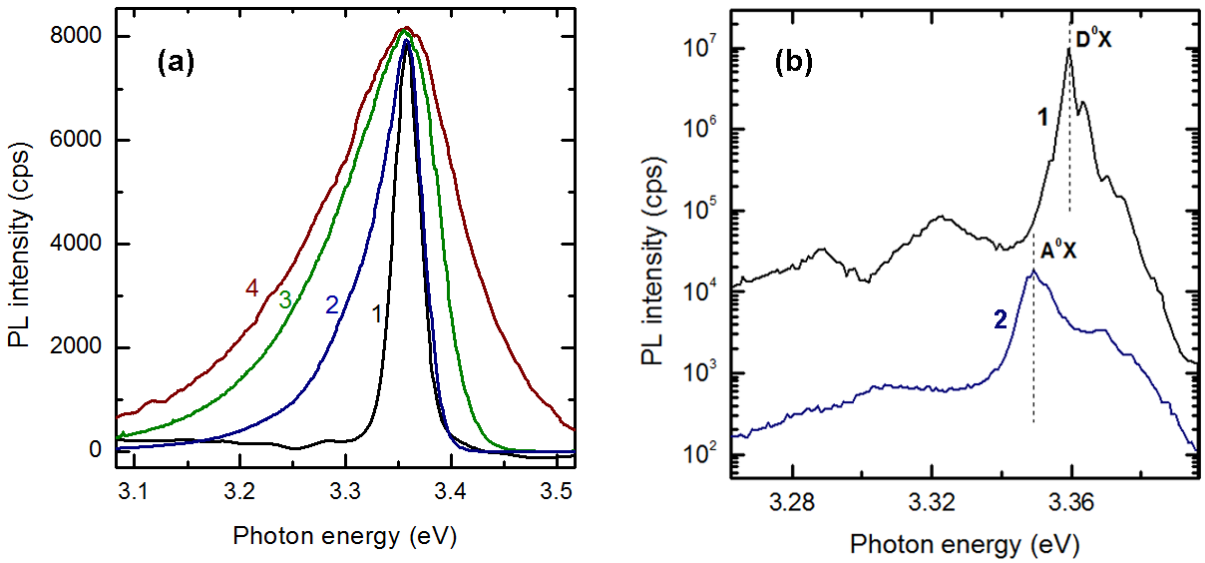

Fig. 5. (a) PL spectra measured at 10 K for ZnO films doped with Al in the ECD process (degree of doping increases from *1* to *4*). (b) PL spectra measured at 10 K for (*1*) the undoped sample and (*2*) for the N-doped sample in the aerosol spray pyrolysis process.

Analysis of PL properties suggests that the films produced by MOCVD and low-pressure CVD should be suitable for the development of lasers, while the optical quality of films prepared by CBD and ECD could be insufficiently high for sustaining stimulated emission and laser action. To verify this issue, the emission spectra of films composed of nanorod arrays with nearly identical morphology and geometrical parameters (as shown in Fig. 6), yet prepared by different methods (by low-pressure CVD and ECD in this case) were studied under pulsed optical pumping under identical conditions. In both cases, the samples have the form of arrays of nanorods with a diameter of about 300 nm and a length of 4–5 μm.

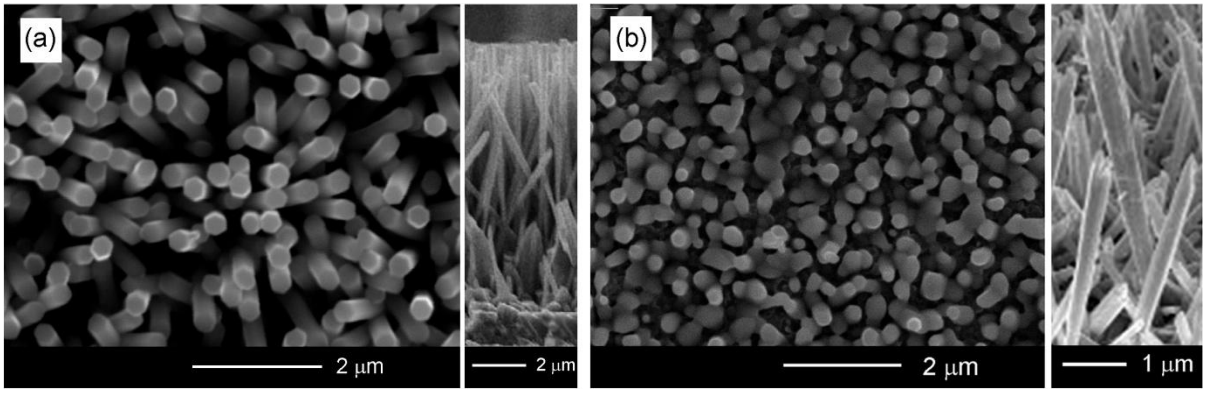

Fig. 6. Top-view and cross-section SEM images of ZnO nanorod films prepared by (a) low-pressure CVD and (b) ECD technologies.

Figure 7a presents the emission spectra of an ensemble of ZnO nanorods with morphology illustrated in Fig. 6a under excitation with a laser spot of 0.2 mm^2. The spectra are

excited by 10-ns laser pulses at a low temperature (10 K) and integrated over 200 pulses. At an excitation power of about 0.2 MW/cm^2, spontaneous emission of about 3.35–3.36 eV is observed. As the pump power increases, the luminescence broadens and undergoes a red shift with increasing intensity. When the power exceeds 0.25 MW/cm^2, additional narrow peaks emerge in the lower energy region. These peaks dramatically increase with a further increase in the pump power. A narrow linewidth (4–5 meV) and a rapid increase in the emission intensities of the peaks indicate that lasing occurs. The observed peaks represent a superposition of lasing modes from different nanorods [20]. In contrast to this, the emission spectrum of the nanorod ensemble grown by ECD with morphology illustrated in Fig. 6b does not change significantly with increasing excitation power density. No narrow emission peaks emerge in the spectrum even at an excitation power density of 3 MW/cm^2; only a broad emission band related to spontaneous emission is observed. With an increase in the excitation power density above 3 MW/cm^2, the sample is damaged without attaining laser action. Therefore, one can conclude that the optical quality of films prepared by ECD in not satisfactory for lasing.

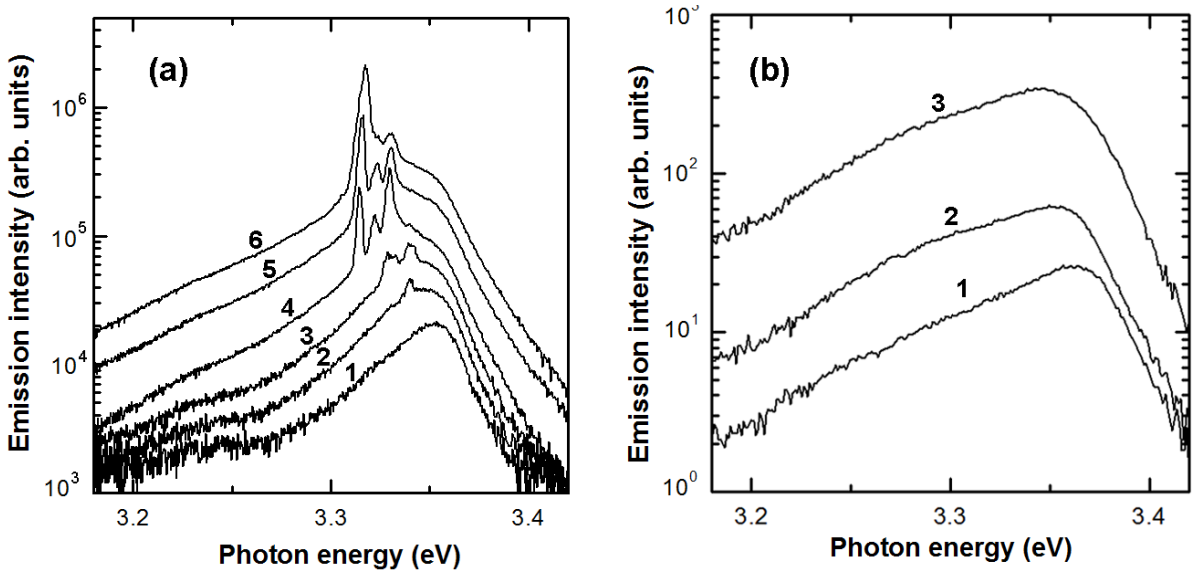

Fig. 7. (a) Lasing in an ensemble of nanorods prepared by low-pressure CVD, as measured at different excitation power densities: (*1*) 200, (*2*) 250, (*3*) 350, (*4*) 500, (*5*) 1500, and (*6*) 2750 kW/cm^2.
(b) Emission spectra of the nanorod array prepared by ECD, as measured at excitation power densities of (*1*) 200, (*2*) 500, and (*3*) 3000 kW/cm^2.

4. Conclusions

This study has shown possibilities of various technological methods to control the morphology and the optical quality of the produced nanostructured ZnO films in view of their implementation in lasers. Investigations of morphologies and emission properties under cw and high-density nanosecond pulsed excitation have shown that low-pressure CVD technologies are most suitable for producing lasing structures with regular resonators sustaining guided modes, while MOCVD, aerosol spray pyrolysis, and thermal treatment of ZnSe crystals produce irregular nanostructures with strong light scattering and high optical quality for random lasers. Wet technologies, such as CBD and ECD, provide the preparation of nanorod arrays which could play

the role of resonators for guided modes; however, procedures should be developed for improving the optical quality to achieve stimulated emission and provide an optical gain for laser action.

References

[1] U. Ozgur, Ya. I Alivov, C. Liu, A. Teke, M.A. Reshchikov, S. Dogan, V. Avrutin, S.J. Cho, and H. Morkoc, J. Appl. Phys., 98, 041301, (2005).
[2] C. Klingshirn, Phys. Stat. Sol. B, 244, 3027, (2007).
[3] H. Morkoc, and U. Ozgur, Zinc Oxide: Fundamentals, Materials and Device Technology, John Wiley & Sons, Weinheim, 2009.
[4] C. F. Klingshirn, B. K. Meyer, A. Waag, A. Hoffmann, J. Geurts, Zinc Oxide: From Fundamental Properties Towards Novel Applications, Springer, Berlin Heidelberg, 2010.
[5] X. W. Sun, and Y. Yang, Zinc Oxide Nanostructures and Their Applications, Pan Stanford Publishing, Boca Raton, 2011.
[6] Ed. C. W. Litton, D.C. Reynolds, and T.C. Collins, Zinc Oxide Materials for Electronic and Optoelectronic Device Applications, John Wiley & Sons, Chichester, 2011.
[7] Ed. C. Jagadish, and S. Pearton, Zinc Oxide Bulk, Thin Films and Nanostructures: Processing, Properties, and Applications, Elsevier, Oxford Kidlington, 2006.
[8] S. J. Pearton, GaN and ZnO-Based Materials and Devices, Springer,Berlin Heidelberg, 2012.
[9] G. -C. Yi, Semiconductor Nanostructures for Optoelectronic Devices: Processing, Characterization and Applications, Springer, Berlin Heidelberg, 2012.
[10] T. Yao and S.-K. Hong, Oxide and Nitride Semiconductors: Processing, Properties, and Applications, Springer, Berlin Heidelberg, 2009.
[11] Z. C. Feng, Handbook of Zinc Oxide and Related Materials, CRC Press, Boca Raton, 2012.
[12] Z. L. Wang, X. Y. Kong, Y. Ding, P. Gao, W.L. Hughes, R. Yang, and Y. Zhang, Adv. Funct. Mater. 14, 943, (2004).
[13] Z. L. Wang, J. Phys.: Condens. Matter, 16, R829, (2004).
[14] A. Burlacu, V. V. Ursaki, V. A. Skuratov, D. Lincot, T. Pauporte, H. Elbelghiti, E .V. Rusu, and I. M. Tiginyanu, Nanotechnology 19, 215714, (2008).
[15] A. N. Redkin, Z. I. Makovei, A. N. Gruzintsev, S. V. Dubonos, and E. E. Yakimov, Inorg. Mater. 43, 253, (2007).
[16] O. Lupan, G. A. Emelchenko, V. V. Ursaki, G. Chai, A. N. Redkin, A. N. Gruzintsev, I. M. Tiginyanu, L. Chow, L.K. Ono, B. R. Cuenya, H. Heinrich, and E.E. Yakimov, Mater. Res. Bull. 45, 1026, (2010).
[17] A. Ennaoui , M. Weber, R. Scheer, and H.J. Lewerenz, Sol. Energy Mater. Sol. Cells 54, 277, (1998).
[18] M. A. Zimmler, F. Capasso, S. Muller, and C. Ronning, Semicond. Sci. Technol. 25, 024001, (2010).
[19] R. Hauschild, and H. Kalt, Appl. Phys. Lett. 89, 123107, (2006).
[20] V. V. Ursaki, V. V. Zalamai, A. Burlacu, J. Fallert, C. Klingshirn, H. Kalt, G.A. Emelchenko, A. N. Redkin, A. N. Gruzintsev, E. V. Rusu, and I. M. Tiginyanu, Phys. D: Appl. Phys. 42, 095106, (2009).
[21] V. V. Ursaki, V. V. Zalamai, A. Burlacu, C. Klingshirn, E. Monaico, and I. M. Tiginyanu, Semicond. Sci. Technol. 24, 085017, (2009).

[22] O. Lupan, G. A. Emelchenko, V. V. Ursaki, G. Chai, A. N. Redkin, A. N. Gruzintsev, I. M. Tiginyanu, L. Chow, L. K. Ono, B. Roldan Cuenya, H. Heinrich, and E. E. Yakimov, Mater. Res. Bull. 45, 1026, (2010).
[23] B. K. Meyer, H. Alves, D. M. Hofmann, W. Kriegseis, D. Forster, F. Bertram, J. Christen, A. Hoffmann, M. Strasburg, M. Dworzak, U. Haboeck, and A.V. Rodina, Phys. Status Solidi (b) 241, 231 (2004).
[24] T. N. Morgan, Phys. Rev. 139, A343 (1965).
[25] V. V. Ursaki, I. M. Tiginyanu, V. V. Zalamai, E. V. Rusu, G. A. Emelchenko, V. M. Masalov, and E. N. Samarov, Phys. Rev. B, 70, 155204 (2004).
[26] V.V. Zalamai, V.V. Ursaki, E. Rusu, P. Arabadji, I.M. Tiginyanu, and L. Sirbu, Appl. Phys. Lett, 84, 5168, (2004).

LUMINESCENCE OF POROUS SEMICONDUCTOR MEDIA COVERED WITH METALLIC FILMS

Vitalie Postolache

National Center for Materials Study and Testing, Technical University of Moldova,
Bd. Stefan cel Mare 168, Chisinau MD-2004, Moldova
E-mail: postolache_vitalie@yahoo.com

(Received January 19, 2016)

Abstract

Porous GaP and InP layers with a pore diameter and a skeleton wall thickness of about 50 nm are prepared on bulk substrates by anodization; microgranular ZnO structures are produced by thermal treatment of ZnTe single crystals in this work. The effect of coating in the prepared samples with thin Au, Cu, Ag and ITO films on their luminescence is investigated; the results are discussed in terms of increased energy transfer between the excited electron−hole pairs and surface plasmons where the surface plasmon resonance matches the energy of photoluminescence bands.

1. Introduction

Metal inclusions in dielectric and semiconductor surfaces, particularly thin metal films, have significant effects upon many material properties. These effects are attributed to excitation of surface plasmon polaritons at the metal/dielectric or metal/semiconductor interfaces, which are waves that propagate along the surface of a conductor. There was an enormous explosion of investigations related to the role of surface plasmon polaritons in the enhanced transmission of light through periodic arrays of subwavelength holes in a metal film [1]. Plasmonic effects in metallic nanostructures are widely used in surface-enhanced Raman scattering (SERS) spectroscopy which is a plasmonics-based spectroscopic technique that combines modern laser spectroscopy with unique optical properties of metallic nanostructures, resulting in strongly increased Raman signals from molecules adsorbed on these nanostructures [2]. SERS is especially important for biological applications, such as single-molecule detection, cellular studies, gene nanoprobes, immunoassay readout, near-field scanning optical microscopy, etc.

The properties of surface plasmons can be tailored by altering the structure of a metal surface which opens large prospects for developing new types of miniaturized photonic device for applications in subwavelength optics, data storage, light generation, microscopy and bio-photonics [3]. The subwavelength applications of metal structures, which circumvent the problem of the diffraction limit of light, are based on the hybrid nature of surface plasmon polaritons, which are light waves coupled to free electron oscillations in a metal. Due to this specific nature, surface plasmon polaritons can be laterally confined below the diffraction limit which makes it possible to develop subwavelength waveguide components including interferometers, ring resonators, and other integrated optical circuits [4, 5]. Negative refraction and metamaterial

issues of plasmonics [6], plasmonic aperture antennas [7], and the large prospects of plasmonics for nanoimaging and nanospectroscopy have also been demonstrated [8].

Enhancement of light emission from nanostructured semiconductors coated with thin metallic films and from light emitting diode (LED) is an important application of plasmonic effects. It was shown that the excited surface plasmons play a key role in the enhanced blue light emission from GaN-LEDs coated with silver films, and the enhancement depends on the geometries of GaN-LED and silver film [9]. Surface plasmon enhancement of emission was observed in GaN-LED based on quantum wells (QWs) [10–13] and in CdSe quantum dots (QDs) [14]. Among other materials, enhancement of the light emission of ZnO films was observed by coupling through localized surface plasmons of Ag island films [15, 16] and Al coatings [17]. The effect of thin metal coatings on the luminescence of porous $CuInSe_2$, $CuGaSe_2$, $CuInS_2$, and $CuGaS_2$ surfaces [18, 19], as well as on TiO_2 nanotubes [20], has been investigated.

The goal of this paper is to study the plasmonic effects in nanostructured layers of GaP, InP, and ZnO covered with thin metallic films.

2. Sample preparation and experimental details

Crystalline (100)-oriented substrates of sulfur doped *n*-InP with a thickness of 500 μm and a free electron concentration of 1.3 x 10^{18} cm^{-3} were supplied by CrysTec GmbH, Germany. Before anodization, conventional photolithography was used to open windows in the photoresist covering for the top surface of the samples. Anodic etching was applied to these samples through opened rectangular windows with a breadth of 35 μm. An electrical contact was made on the backside of the anodized samples with a silver paint. The anodization of the InP substrates was carried out in 500 Ml of a 5% HCl aqueous solution at 25^{o}C in a common two-electrode cell with an applied voltage of 5 V, where the sample served as a working electrode. A platinum wire (0.5-mm diameter) mesh with a surface of 6 cm^2 was used as a counter electrode. A Keithley's Series 2400 Source Measure Unit was used as a potentiostat.

(111)-oriented *n*-GaP substrates used in this study were cut from Te-doped liquid encapsulation Czochralsky-grown ingots with a free electron concentration of 1×10^{18} cm^{-3} at 300 K. Porosity was introduced by anodic etching of samples in a 0.5M aqueous solution of sulphuric acid at a current density of 5 $mAcm^{-2}$ for 30 min using the above-mentioned conventional electrochemical cell with a Pt working electrode.

Microgranular ZnO samples were prepared on the basis of bulk Na-doped ZnTe single crystals with a free hole concentration of 3 x 10^{18} cm^{-3}. ZnTe bulk crystals were annealed at 700^{o}C in air for 1 h.

Thin Ag, Au, and Cu coatings were deposited onto nanostructured sample surfaces by means of a Cressington magnetron sputtering coater in order to study the plasmonic effects on luminescence. ITO films were deposited on the surface of porous InP by a spray pyrolysis method described elsewhere [21].

The morphology of the prepared samples was studied by microanalysis using Zeiss Sigma and TESCAN Vega TS 5130MM scanning electron microscopes (SEM). The continuous wave photoluminescence (PL) of ZnO and GaP samples was excited by the 351 nm and 488 nm lines of an Ar^+ SpectraPhysics laser, respectively, and analyzed with a double spectrometer with a FEU 106 photomultiplier ensuring a spectral resolution better than 0.5 meV. The samples were mounted on the cold station of a LTS-22-C-330 optical cryogenic system. The PL spectra were

measured at a temperature of 10 K. The PL of InP samples was excited by a LD Pumped all-solid state MLL-III-532 laser and analyzed through the same double spectrometer with a FEU 62 photomultiplier in a spectral range of 1.1–1.5 eV and with a PDA10DT InGaAs photodetector in a spectral range of 0.6–1.1 eV. The PL spectra were measured at a temperature of 10 K.

3. Results and discussion

A porous structure with pore diameters of about 50 nm and the thickness of skeleton walls comparable with the pore diameter is prepared under the above-mentioned technological conditions in InP substrates (Fig. 1a). It should be noted that a similar morphology is obtained in GaP substrates. The morphology of the prepared ZnO sample (Fig. 1b) exhibits a granular structure with mean granule dimensions of about 1 μm. X-ray diffraction (XRD) and PL analyses showed that annealing at 700^{o}C leads to a total transformation of the initial ZnTe crystals into wurzite ZnO [22].

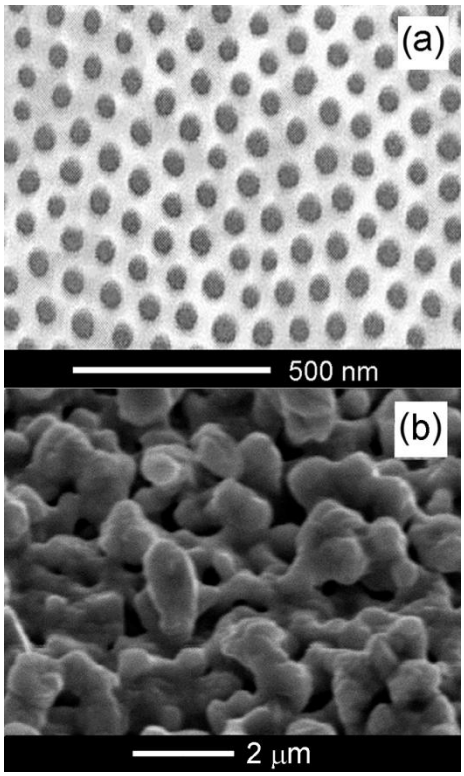

Fig. 1. (a) SEM image of a porous InP sample prepared by anodic etching and (b) morphology of the ZnO micro-granular material prepared by thermal treatment of bulk ZnTe crystals.

The PL spectrum for the porous GaP sample is dominated by a broad emission band at ~1.75 eV and a narrower emission at ~2.2 eV (Fig. 2, curve 1). The PL band at 1.75 eV is attributed to the molecular complexes Zn_{Ga}–O_P and/or Cd_{Ga}–O_P forming an isoelectronic trap in GaP [23]. An emission band at 2.2 eV observed previously in GaP doped with sulfur was assigned to electron–hole recombination at sulfur–carbon pairs [23–25]. Since our samples are doped with Te instead of S, one can suggest that the observed emission at about 2.2 eV is related to Te–C pairs.

The deposition of thin Au films enhances the PL band at 2.2 eV and slightly decreases the intensity of the 1.75-eV PL band (Fig. 2a). It was previously shown that the surface plasmon resonance frequency at Au/semiconductor interfaces is about 2.3 eV [12] and the density states of the SP mode become dramatically larger while approaching the SP frequency. This large density of states enhances the excited electron–hole energy transfer to plasmon excitation and increases the spontaneous emission rates. It is evident that the metal film deposited on the porous structure is not continuous because its thickness is lower than the pore diameter and the porous skeleton wall thickness. This means that the resonance plasmon frequency can vary in a certain range. It is known that the energy of localized surface plasmon modes depends on the form and size of metal structures [15]. One can suggest that the enhancement of luminescence at 2.2 eV is due to surface plasmons because the energy position of this PL band is close to the resonance energy of the surface plasmons at the Au/porous GaP interface. On the other hand, the decrease in the intensity of the PL band at 1.75 eV can be attributed to the absorption of light in the metal film. Note that the deposition of metal films thicker than 20 nm leads to the overall decrease in the PL intensity.

The deposition of Cu films on the surface of the porous GaP sample, conversely, enhances the PL band at 1.75 eV and attenuates the PL band at 2.2 eV (Fig. 2b). This means that the resonance energy of the surface plasmons at the Cu/porous GaP interface is closer to the position of the 1.75-eV PL band. Similar effects were observed in the luminescence of porous $CuGaSe_2$ and $CuGaS_2$ surfaces covered with thin Cu films [18, 19]. Localized surface plasmon resonance of Cu nanoparticles has been reported in this spectral range [26].

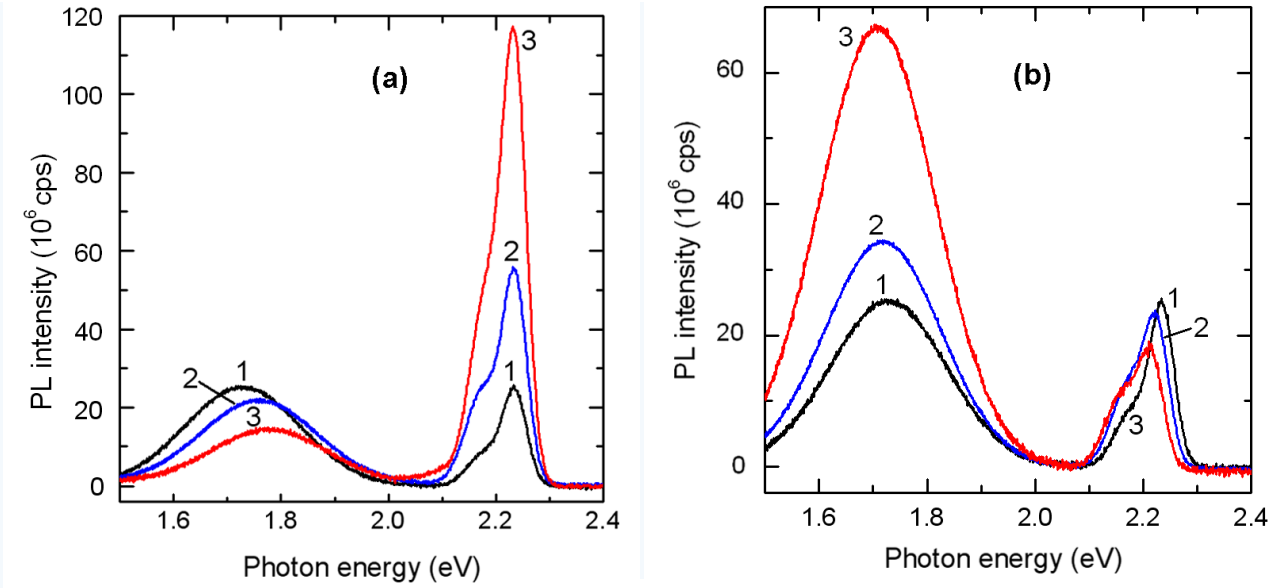

Fig. 2. Low-temperature (10 K) PL spectra of a porous GaP sample after anodization (curve 1) and after covering with Au (a) and Cu (b) films with a thickness of 10 (curve 2) and 20 nm (curve 3).

Figure 3 illustrates a similar effect of Au and Cu film coating on the luminescence of microgranular ZnO. The high optical quality of the resulting ZnO material is demonstrated by the PL spectrum, which is dominated by an emission band related to the recombination of donor bound D^0X at 3.356 eV and a band associated with donor–acceptor (DA) pair recombination at 3.31.eV [27]. The visible emission is a combination of red (about 1.8 eV) and green (about 2.4 eV) PL bands. Usually, the visible emission from ZnO is attributed to different defects, such as oxygen (V_O) and zinc vacancies (V_{Zn}) or a complex defect involving interstitial zinc (Zn_i) and interstitial oxygen (O_i) [28–30]. One can see from Fig. 3 that, similarly to the porous GaP samples, the coating of microgranular ZnO surfaces with Au films leads to an increase in the intensity of the green PL band, while the intensity of the red PL band is increased by coating with Cu. This behavior is explained in terms of plasmonic effects as described above.

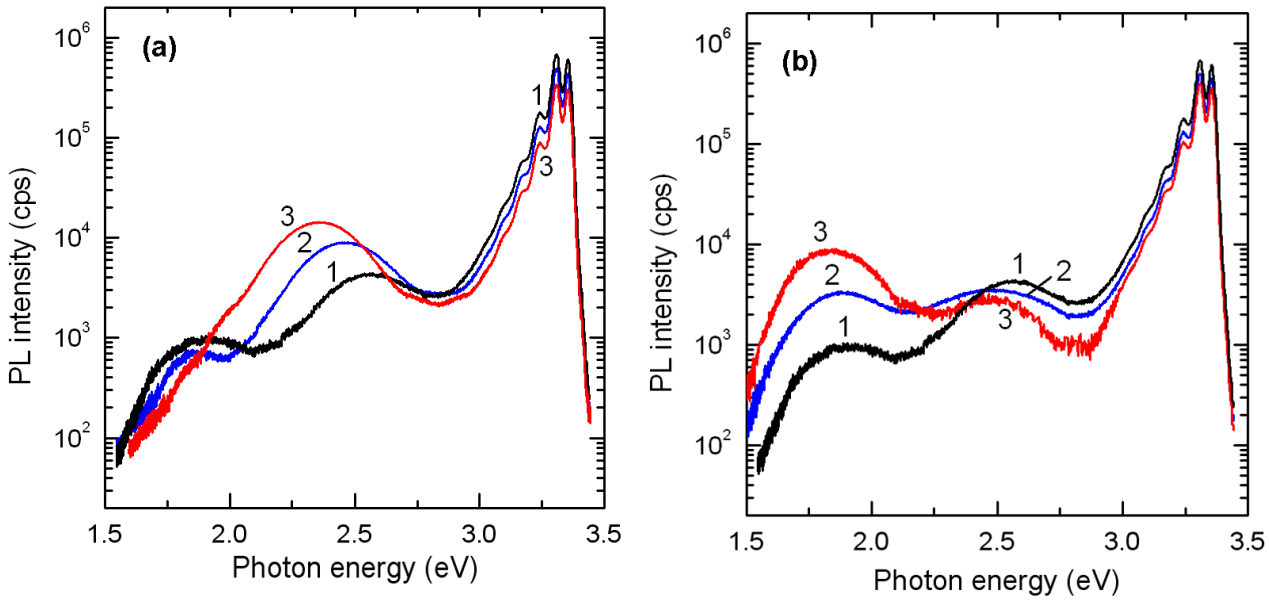

Fig. 3. Low-temperature (10 K) PL spectra of a microgranular ZnO sample without metal coating (curve 1) and coated with Au (a) and Cu (b) films with a thickness of 20 (curve 2) and 30 nm (curve 3).

\

Coating of ZnO samples with Ag films leads to a decrease in the red luminescence intensity and an increase in both the green luminescence and the near bandgap emission related to exciton and DA pair recombination (Fig. 4). A surface plasmon resonance energy at Ag/semiconductor interfaces in a range of 2.8–3.0 eV was previously reported [9, 10, 12]. Therefore, the results of this study show a broad-band effect of Ag coating on the microgranular ZnO surface. Note that an enhancement of the near band edge ultraviolet emission from ZnO films by localized surface plasmons of Ag island films were previously reported [15, 16].

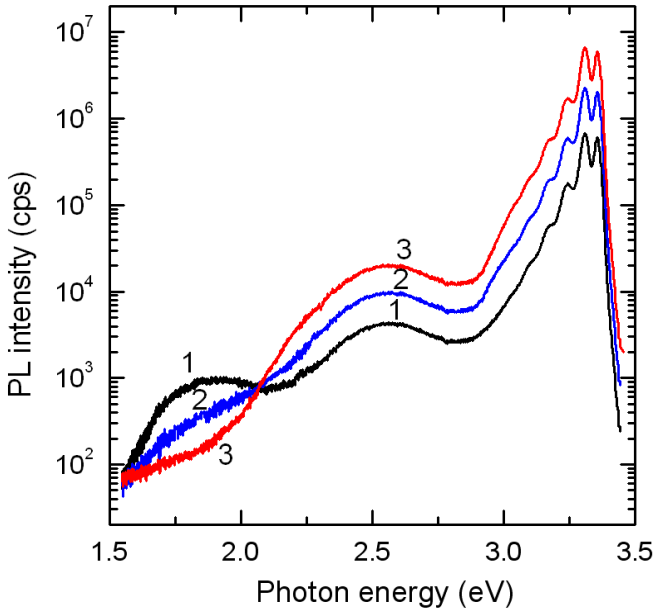

Fig. 4. Low-temperature (10 K) PL spectra of a microgranular ZnO sample without metal coating (curve 1) and coated with Ag films with a thickness of 20 (curve 2) and 30 nm (curve 3).

Finally, we will discuss the possibilities of controlling the PL intensity in porous InP layers by coating with conducting films. Due to the narrow bandgap of InP, the energy of luminescence bands in a range of 0.7–1.4 eV is far from plasmonic resonances in all the above used metals (Ag, Au, and Cu). On the other hand, previous investigations suggested that surface plasmon resonance features in the near infrared spectral range may be inherent in ITO thin films [31]. Taking this into account, we studied the effect of ITO coatings on the luminescence of porous InP layers. Figure 5 presents the PL spectrum of a porous InP layer with the morphology shown in Fig. 1a, which is dominated by an emission band related to DA pair recombination at 1.38 eV with phonon replicas and a shoulder at 1.41 eV associated with exciton recombination [32, 33]. The other two broader PL bands observed in the spectrum at 1.1 eV and 0.75 eV were previously attributed to a complex center consisting of a phosphorus vacancy and an acceptor impurity [34] and a deep center of unidentified nature [35, 36], respectively. One can see from Fig. 5 that the infrared luminescence of the porous InP sample is enhanced by the deposition of a thin ITO film and the luminescence intensity increases with an increase in the film thickness from 10 to 20 nm. Note that the enhancement of the PL intensity is observed with ITO films thicker than 5 nm. However, it is difficult to control the film thickness lower than 5 nm. The longer the PL band wavelength, the more significant the luminescence enhancement. This effect suggests that the PL enhancement is also due to surface plasmons which exhibit a wide resonance at the ITO/porous InP interface.

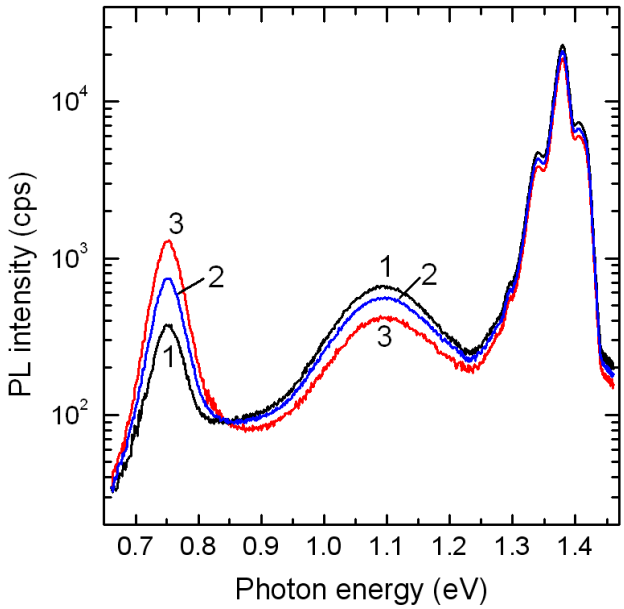

Fig. 5. Low-temperature (10 K) PL spectra of a porous InP sample after anodization (curve 1) and after covering with ITO films with a thickness of 10 (curve 2) and 20 nm (curve 3).

4. Conclusions

The results of this study have shown that it is possible to control the PL of porous GaP and InP layers and microgranular ZnO by coating with conducting films. The PL bands at 2.2–2.4 eV in porous GaP and microgranular ZnO are enhanced by coating with Au films, while the PL band at 1.75–1.80 eV is enhanced by Cu film coating. Deposition of Ag films leads to an increase in the PL intensity in a spectral range of 2.4–3.4 eV in ZnO samples, while deposition of ITO films enhances the PL of porous InP layers in a spectral range of 0.7–1.2 eV. These effects are attributed to an increase in the electron–hole energy transfer to plasmon excitations due to the matched resonance of surface plasmons with the energy of respective PL bands, which in turn leads to enhanced spontaneous emission rates.

References

[1] W. L Barnes, W. A. Murray, J. Dintinger, E. Devaux, and T. W. Ebbesen, Phys. Rev. Lett. 92, 107402, (2004).
[2] T. Vo-Dihn, F. Yan, and D. L. Stokes, Methods Mol. Biol. 300, 255, (2005).
[3] W. L. Barnes, A. Dereux, and T. W. Ebbesen, Nature 424 (6950), 824, (2003).
[4] S. I. Bozhevolnyi, V. S. Volkov, E. Devaux, J. Y. Laluet, and T. W. Ebbesen, Nature 440 (7083), 508, (2006).
[5] C.-P. Huang and Y.-Y. Zhu, Act. Passive Electron. Compon. 2007, 30946, (2007).
[6] B. Stein, J. Y. Laluet, E. Devaux, , C. Genet, and T. W. Ebbesen, Phys. Rev. Lett. 105, 266804, (2010).
[7] J. M. Yi, A. Cuche, E. Devaux, , C. Genet, and T. W. Ebbesen, ACS Photonics 1, 365, (2014).

[8] S. Kawate, Appl. Spectrosc. 67, 117, (2013).
[9] J. Zhao, K. Li, F. Kong, and D. Liu-Ge, Progr. Electromagn. Ress. 108, 293, (2010).
[10] I. Gontijo, M. Boroditsky, and E. Yablonovitch, S. Keller, U. K. Mishra, and S. P. DenBaars, Phys. Rev. B. 60, 11564, (1999).
[11] K. Okamoto, I. Niki, A. Shvartser, Y. Narukawa, T. Mukai, and A. Scherer. Nature Mater. 3, 601, (2004).
[12] K. Okamoto, I. Niki, A. Shvartser, G. Maltezos, Y. Narukawa, T. Mukai, Y. Kawakami, and A. Scherer, Phys. Stat. Sol. (a) 204, 2103, (2007).
[13] M.-K. Kwon, J.-Y. Kim, B.-H. Kim, I.-K. Park, C.-Y. Cho, C. C. Byeon, and S.-J. Park, Adv. Mater. 20, 1253, (2008).
[14] K. Okamoto, A. Scherer, and Y. Kawakami, Phys. Stat. Sol. (c) 5, 2822, (2008).
[15] P. Cheng, D. Li, Z. Yuan, P. Chen, and D. Yang, Appl. Phys. Lett. 92, 041119 (2008).
[16] P. Cheng, D. Li, X. Li, T. Liu, and D. Yang, J. Appl. Phys. 106, 063120, (2009).
[17] J. Li and H. C. Ong, Appl. Phys. Lett. 92, 121107, (2008).
[18] V. V. Ursaki, Mold. J. Phys. Sci. 12, 221, (2013).
[19] V. V. Ursaki, Mold. J. Phys. Sci. 13, 30, (2014).
[20] M. Enachi, M. Stevens-Kalceff, A. Burlacu, I. Tiginyanu, and V. Ursaki, ECS Trans. 45, 167, (2012).
[21] A. Simashkevich, D. Serban, L. Bruc, A. Coval1, V. Fedorov, E. Bobeico, and Iu. Usatii, Mold. J. Phys. Sci. 3, 334, (2004).
[22] V. Zalamai, A. Burlacu, V. Postolache, E.V. Rusu, V.V. Ursaki, and I.M. Tiginyanu, Mold. J. Phys. Sci. 9, 34, 308, (2010).
[23] A. N. Pikhtin and O. L. Lazarenkova, in Handbook of Electroluminescent Materials, ed. by D. R. Vij (Institute of Physics Publishing, Bristol, 2004), 282 p
[24] P. J. Dean, J. D. Cuthbert, and R. T. Lynch, Phys. Rev. 179, 754 (1969).
[25] K. Tomioka and S. Adachi, J. Appl. Phys. 98, 073511, (2005).
[26] G. H. Chan, J. Zhao, E. M. Hicks, G. C. Schatz, and R. P. Van Duyne, Nano Lett. *7*, 1947, (2007).
[27] V.V. Ursaki, I.M. Tiginyanu, V.V. Zalamai, V.M. Masalov, E.N. Samarov, G.A. Emelcenko, and F. Briones, Semicond. Sci. Technol. 19, 85, (2004).
[28] Ü. Özgür, Ya.I. Alivov, C. Liu, A. Teke, M.A. Reshchikov, S. Dogan, V. Avrutin, S.J. Cho, and H. Morkoç, J. Appl. Phys. 98, 041301, (2005).
[29] H.C. Ong and G.T. Du, J. Cryst. Growth 265, 471, (2004).
[30] A.B. Djurisic, Y.H. Leung, K.H. Tam, Y.F. Hsu, L. Ding, W.K. Ge, Y.C. Zhong, K.S. Wong, W.K. Chan, H.L. Tam, K.W. Cheah, W.M. Kwok, and D.L. Phillips, Nanotechnology 18, 095702, (2007).
[31] C. Rhodes, S. Franzena, J.-P. Maria, M. Losego, D. N. Leonard, B. Laughlin,G. Duscher, and S. Weibel, J. Appl. Phys. 100, 054905, (2006).
[32] A.N. Georgobiani, A.V. Mikulyonok, I.G. Stoyanova, and I.M. Tiginyanu, Phys. Stat. Sol. (a) 80, 109, (1983).
[33] F.P Korshunov, S.I. Radautsan, N.A. Sobolev, I.M. Tiginyanu, V.V. Ursaki, and E.A. Kudryavtseva, Sov. Phys. Semicond. 23, 980, (1989).
[34] Y. Yamazoe, Y. Sasoi, T. Nishino, and Y. Hamakawa, Jpn. J. Appl. Phys. 20, 347, (1981).
[35] H. Temkin, B. V. Dutt, W. A. Bonner, and V. G. Keramidas, J. Appl. Phys. 53, 7526, (1982).
[36] E. V. K. Rao, A. Sibile, and N. Duhamel, Physica B+C 116, 449, (1983).

A COMPARATIVE STUDY OF PHOTOCONDUCTIVITY DECAY IN GRANULAR AND NANOWIRE ZnO

Vitalie Postolache

National Center for Materials Study and Testing, Technical University of Moldova,
Bd. Stefan cel Mare 168, Chisinau, MD-2004 Republic of Moldova
E-mail: postolache_vitalie@yahoo.com

(Received January 19, 2016)

Abstract

A comparative analysis of transient photoconductivity in microgranular ZnO and ZnO nanowires prepared by oxidizing bulk ZnTe and ZnTe nanowires, respectively, is performed in this paper. The measurements are carried out at different temperatures in microgranular ZnO and at room temperature in the ambient air in ZnO nanowire networks. The mechanisms of photoconductivity decay are discussed taking into account the morphological features of the samples and the range of measured relaxation times.

1. Introduction

Long-duration-photoconductivity decay and persistent photoconductivity (PPC) inherent in many materials can have a significant effect on the characteristics of device structures prepared on their basis, such as UV detectors, field effect transistors, gas sensors, etc. in terms of their sensitivity, noise properties, dark level, and response speed. Different mechanisms were considered as the origin of PPC. The origin of PPC in moderately doped bulk semiconductors, such as III–V alloys, is believed to be related to atomic defect centers with unusual properties, such as defects with bistable character [1, 2], AX [3], or DX centers [4–7]. AX centers are acceptors, while DX centers are donors.

It is generally accepted that the mechanism leading to the metastable behavior of DX centers is due to the large lattice relaxation following electron capture by the DX state. It is also generally believed that the DX center should behave as the so-called negative-U center [8–10].

In highly doped compensated semiconductors, it was suggested that the microscopic inhomogeneity caused by impurity distribution is the most probable cause of the PPC phenomenon [11–15]. According to this model, the spatial separation of the photogenerated electrons and holes by macroscopic potential barriers occurs due to band bending around doping inhomogeneities; however, these potential barriers can also be formed at planar surfaces, interfaces, junctions, etc. If these potential barriers are sufficiently high in comparison with the thermal voltage kT/q, the lifetime of the electron and hole becomes very long. This mechanism with macroscopic potential barriers was also applied to explain the PPC in II–VI semiconductor alloys [16–19]. It was suggested that, in this case, the spatial separation between stored charge carriers by random local-potential fluctuations is caused by compositional fluctuations.

The origin of PPC and optical quenching of photoconductivity (PC) were also

investigated in bulk GaN layers. It was demonstrated to originate from metastable defects and explained in terms of a model combining two previously proposed schemes with electron traps playing the main role in PPC and hole traps inducing optical quenching of PC [20, 21].

Long-duration-photoconductivity decay and PPC have also been shown to be inherent in porous materials [22, 23]. Similarly to highly doped compensated semiconductors and alloys with compositional fluctuations, PPC in porous materials was suggested to be caused by potential barriers induced by random local-potential fluctuations; however, in this case, the potential fluctuations are caused by porosity.

The PPC in nanowires, for instance, ZnO and GaN nanowires characterized by a high surface-to-volume ratio, has a different nature. It is generally believed that, in this case, PPC is caused by a strong surface band bending (SBB) effect instead of a bulk trap effect [24, 25]. The significant SBB in nanowires localizes the excess carriers. As a result, strongly reduced recombination of holes with those electrons trapped at the surface considerably extends the carrier lifetime. It was shown that SBB in ZnO nanowires is strongly governed by surface adsorbed species, among which oxygen molecules play a major role [26–29]. In general, surface-induced carrier localization is proposed to be one of the main causes of PPC in nanostructures with a high surface-to-volume ratio, such as utrathin InP membranes and nanoperforated GaN membranes [30, 31].

Regardless of the nature of PPC, these phenomena can have a significant effect on the characteristics of device structures, such as UV detectors, field effect transistors, gas sensors, etc. in terms of their sensitivity, noise properties, dark level, and response speed.

The goal of this paper is to perform a comparative study of PC decay in microgranular ZnO structures and nanowires with reference to the mechanism governing the PC relaxation processes.

2. Sample preparation technique

Nanostructured ZnO samples were prepared on the basis of Na-doped bulk ZnTe single crystals with a free hole concentration of 3×10^{18} cm^{-3}. Microgranular ZnO and ZnO nanowires were prepared by two different technological routes. ZnTe bulk crystals were annealed in a temperature interval of 300 to 800 ^{o}C in air for 1 h to produce granular ZnO. The sizes of granules can be varied by changing the annealing temperature. The morphology of a granular ZnO sample with mean granule dimensions of around 1 μm obtained after thermal treatment at 700^{o}C is shown in Fig. 1a. X-ray diffraction and photoluminescence analyses demonstrated that annealing at 700^{o}C leads to a total transformation of the initial ZnTe crystals into wurzite ZnO [32], the photoluminescence spectra being dominated by the emission related to the recombination of donor bound D^0X excitons. According to the second technological route, a template of ZnTe nanowires with a mean diameter around 50 nm is produced in the first step by electrochemical treatment of ZnTe crystals as described elsewhere [32]. Anodic etching was conducted in an HNO_3 : HCl : H_2O electrolyte at a ratio of 5 : 20 : 100 at 25^{o}C with the application of 0.3-s voltage pulses at a frequency of 1 Hz and an amplitude of 5 V. The ZnTe nanowires are transformed into ZnO nanowires in the second step by thermal treatment. The morphology of the nanowires does not change during annealing at 500^{o}C (Fig. 1b), while the material is totally oxidized. The morphology and chemical composition microanalyses of the samples were conducted using a VEGA TESCAN TS 5130MM scanning electron microscope equipped with an Oxford Instruments INCA energy dispersive X-ray system.

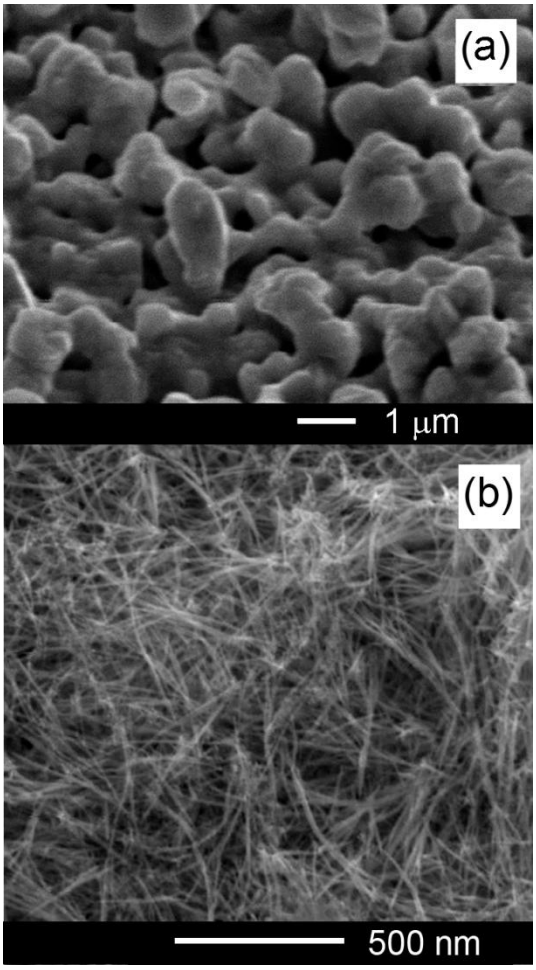

Fig. 1. Morphology of the ZnO microgranular material prepared by thermal treatment of bulk ZnTe crystals (a) and ZnO nanowires prepared from ZnTe nanowires (b).

3. Experimental details of measuring PC decay

The electrical contacts to samples for measuring PC were prepared using a conductive silver paste. Since the decay time is long enough in a network of ZnO nanowires, a 366-nm excitation beam of an Hg arc lamp was mechanically shut in the PC relaxation experiments. The experiments were performed at room temperature in ambient air.

The photoresponse from granular samples was measured with the set-up schematically shown in Fig. 2. The UV illumination was provided by a UV light-emitting diode (LED) with a peak wavelength of 370 nm powered by a G6-15 function generator. The sample was biased at 5 V. The signal from a resistor connected in series with the investigated sample was measured by a digital sampling storage C9-8 oscilloscope. The signal from the oscilloscope was introduced in an IBM computer via IEEE-488 interface for further data processing. The sample was mounted in a LTS-22-C-330 Workhorse-type optical cryogenic system to perform measurements in a

temperature interval of 100–300 K.

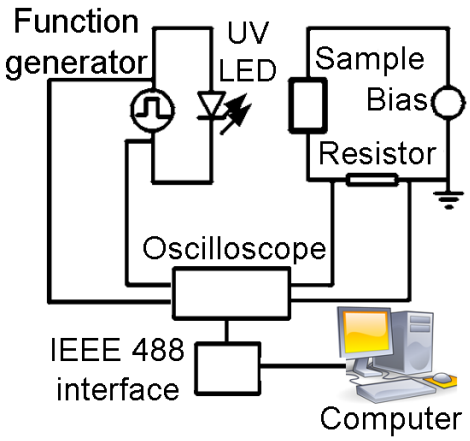

Fig. 2. Schematic diagram of the setup for measuring the PC response from ZnO nanowires.

4. PC relaxation in microgranular ZnO

The excitation square wave from the function generator is illustrated in Fig. 3a; the photoresponse of the microgranular ZnO sample is shown in Fig. 3b. It is evident from Fig. 3b that the PC relaxation is nearly symmetric with respect to PC build-up and decay. The analysis of these relaxation curves shows that the relaxation time decreases from about 200 ms at 100 K to 50 ms at 150 K with a further increase to 300 ms at 230 K. Therefore, a nonmonotonic temperature dependence on the PC relaxation time is observed.

A more detailed dependence of the relaxation time in the Arrhenius plot is presented in Fig. 4. The relaxation time was determined, for each experimental point presented in Fig. 4, from the analysis of the PC decay curve measured at the respective temperature. This relaxation time dependence resembles a typical behavior of the carrier lifetime for carrier recombination via recombination centers. In the case of carrier recombination via recombination centers, the relaxation time is constant and equals τ_p until the Fermi level intersects the defect energy level. Further, the lifetime increases exponentially with temperature up to the region of intrinsic conductivity, with a consequent exponential decrease. However, some important observations are in contradiction with this model of recombination, namely: (i) the relaxation time (~50–300 ms) is significantly higher than the carrier lifetime (~ several μs) typical for processes governed by recombination centers; (ii) there are some contradictions related to the parameters deduced from this model: according to this model, one can estimate the position of the recombination level by determining the temperature of Fermi-level intersection with the defect energy level $T_1 \approx 187$ K, the temperature of the transition to the intrinsic conductivity $T_2 \approx 230$ K, and the intersection of the extrapolated $T_1 \div T_2$ segment (Fig. 4) with the ordinate axis which gives the value of $\ln(\tau_{p0}N_c/n_0) = 8$; by extracting the value of $\ln \tau_{p0} = -3$ from this value, we obtain $\ln(N_c/n_0) = 11$; then, one can calculate the defect energy level $E_c - E_t = kT_1\ln(N_c/n_0) = 177$ meV; the second observation is that the value of T_1 and T_2 are too close to each other for the given defect energy level; (iii) the temperature of transition to intrinsic conductivity $T_2 = 230$ K is unlikely low, while this usually occurs at temperatures much higher than the room temperature in this kind of

samples [33]; (iv) there is an increase of the relaxation time with decreasing temperature from 150 to 100 K.

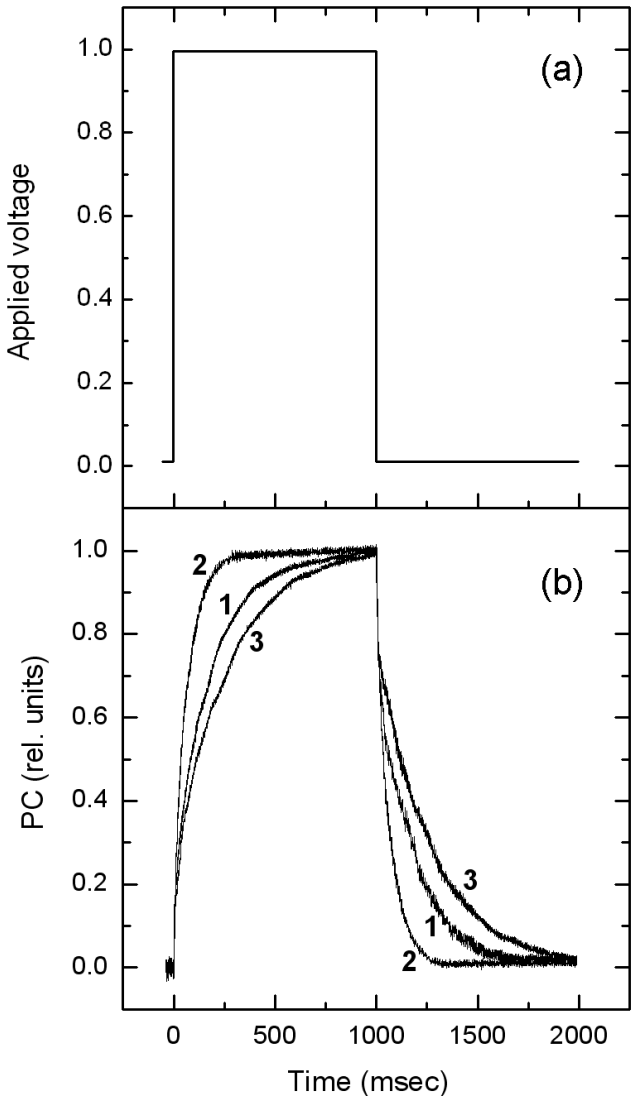

Fig. 3. Excitation pulse (a) and photoconductivity response measured from the microgranular ZnO sample at a temperature of 100 (curve 1), 150 (curve 2), and 230 K (curve 3).

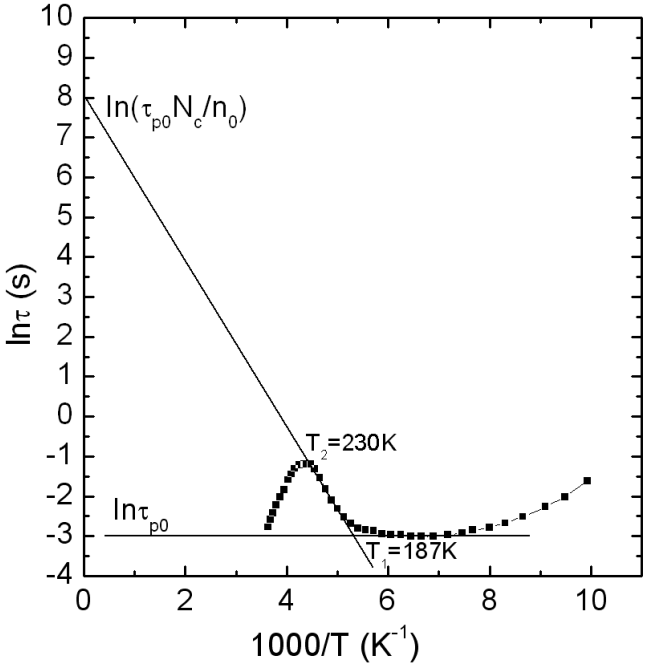

Fig. 4. Temperature dependence of the PC decay time in the microgranular ZnO sample.

The above mentioned observations indicate the implication of traps in the nonequilibrium carrier recombination processes. In the case of trap implication, the effective relaxation time is given by the expression

$$\tau' = \tau_n \left(1 + \frac{M}{N_c} e^{\frac{(E_c - E_M)}{kT}} \right), \tag{1}$$

where τ_n the lifetime of the electron, M is the trap concentration, N_c is the effective density of states in the conduction band, E_c is the energy of the conduction band bottom, and E_M is the position of the trap energy level.

Therefore, one can conclude that the charge transport in microgranular ZnO structures occurs due to percolation (interconnections) of grains and the PC relaxation is governed by bulk processes in the grains with a significant effect from trapping centers.

5. Long-duration PC decay in ZnO nanowires

The PC relaxation processes in nanowire samples has a different nature. Figure 5 shows the PC build-up and decay in a network of ZnO nanowires with the morphology illustrated in Fig. 1b. First of all, the relaxation time is two orders of magnitude longer than that for the microgranular sample. This large relaxation time cannot be explained by trapping effects of bulk centers. Models with microscopic (atomic) energy barriers at centers with large lattice relaxation, such as DX centers, have not been reported in ZnO either. On the other hand, the SBB effects are generally accepted as the origin for long relaxation times and PPC in ZnO nanowires [25–29].

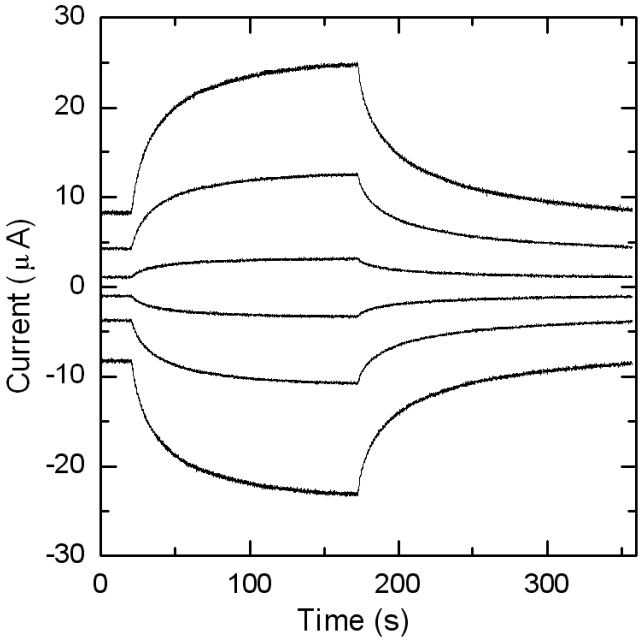

Fig. 5. Photoconductivity build-up after illumination with UV radiation power density of 250 mW/cm^2 (at 20 s) and decay after illumination removal (at 170 s) in a network of ZnO nanowires measured at room temperature (300 K) in ambient air at different applied bias (from top to bottom, the curves were obtained with an applied external bias of 5, 3, 1, –1, –3, and –5 V, respectively).

The fact that the shape of the relaxation curves is not affected by a change in the applied bias and the polarity of the bias indicates an insignificant influence of contact effects. The percolation of randomly oriented nanowires, as deduced from Fig. 1b, provides a pathway of current through the nanowire network, while the huge surface-to-volume ratio suggests the primordial importance of surface effects and that of oxygen molecules, since measurements are performed in ambient air. The photoresponse of ZnO in air is known to be governed by the adsorption (in the dark) and desorption (under UV illumination) of oxygen molecules [25]. In the dark, oxygen molecules adsorbed on the surface of ZnO nanowires capture free electrons of the *n*-type semiconductor: $O_2(g) + e^- \rightarrow O_2^-(ad)$. This produces a depletion layer near the nanowire surface, resulting in an upward band bending near the surface. Due to the large surface-to-volume ratio, the adsorption of O_2 significantly reduces the conductivity of the nanowires. UV-light illumination with a photon energy higher than E_g generates electron–hole pairs in the ZnO. Holes migrate to the surface along the potential slope created by the band bending and recombine with O_2-trapped electrons, thus releasing oxygen from the surface: $O_2^-(ad) + h+ \rightarrow O_2(g)$. The unpaired electrons are either collected at the anode or recombine with holes generated when oxygen molecules are readsorbed and ionized at the surface. Similar effects upon the PPC and optical quenching of PC from surface-induced carrier localization and strongly reduced recombination of holes with electrons trapped at the surface have been reported in GaN nanowires [24] and nanoperforated GaN membranes [31].

6. Conclusions

The results of this comparative study reveal a different nature of the transient PC in microgranular ZnO and ZnO nanowires prepared by oxidizing bulk ZnTe and ZnTe nanowires, respectively. The percolation of granules in microgranular ZnO provides a reliable current flow as in bulk materials, and the photoconductivity build-up and decay is determined by bulk defects including bulk charge carrier trapping centers, the PC relaxation time being on the order of tens or hundreds of milliseconds. The PC relaxation time in random networks of microwires is two orders of magnitude longer, being governed by surface states, SBB effects, and various adsorption–desorption processes, rather than by bulk trap effects. Most probably, oxygen molecules play a primordial role among these species.

References

[1] C. V. Reddy, A. Balakrishnan, H. Okumura, and S. Yoshida, Appl. Phys. Lett. 73, 244, (1998).
[2] C. Johnson, J. Y. Lin, H.X. Jiang, M. A. Khan, and C .J. Sun, Appl. Phys. Lett. 68, 1808, (1996).
[3] Z. Li, J.Y. Lin, H.X. Jiang, A Salvador, A. Botchkarev, and H. Morkoc, Appl. Phys. Lett. 69, 1474, (1996).
[4] D. V Lang and R. A. Logan, Phys. Rev. Lett. 39,635, (1977).
[5] D. V. Lang, R. A. Logan, and M. Jaros, Phys. Rev. B 19, 1015, (1979).
[6] J. Z. Li, J. Y. Lin, H. X. Jiang, M. A. Khan, and Q. Chen, J. Appl. Phys. 82, 1227, (1997).
[7] J.Z. Li, J.Y. Lin, H.X. Jiang, M.A. Khan, and Q. Chen, J. Vac. Sci. Technol. B15, 1117, (1997).
[8] J. Hubbard, Proc. R. Sot. London Ser. A 276,238, (1963).
[9] P. W. Anderson, Phys. Rev. Lett. 34, 953, (1975).
[10] G. D. Watkins, in Festkiirperpmbleme: Advances in Solid State Physics, edited by P. Grosse (Vieweg, Braunschweig, 1984), Vol. 24, 163 p.
[11] B. I. Shklovskii and A. L. Efros., JETP 60, 867, (1971); JETP 61, 816, (1971).
[12] M. K. Sheinkman and A. Ya. Shik, Fiz. Tekh. Poluprovodn. 10, 209 (1976) [Sov. Phys-Semicond. 10, 128 (1976)].
[13] R. R. Lowney and S. Mayo, J. Electr. Matter, vol. 21, p. 731, (1992).
[14] H. J. Queisser and D. E. Theodorou, Phys. Rev. B, vol. 33, p. 4027, (1986).
[15] V. S. Vavilov, P. C. Euthymiou, and G. E. Zardas, Phys.-Usp., vol. 42, p. 199, (1999).
[16] H. X. Jiang and J. Y. Lin, Phys. Rev. Lett. 64, 2547, (1990).
[17] H. X. Jiang and J. Y. Lin, Phys. Rev. B 40, 10025, (1989).
[18] J. Y. Lin and H. X. Jiang, Phys. Rev. B 41, 5178, (1990).
[19] H. X. Jiang, G. Brown, and J. Y. Lin, J. Appl. Phys. 69, 6701, (1991).
[20] V. Ursaki, I. M. Tiginyanu, P. C. Ricci, A. Anedda, S. Hubbard, and D. Pavlidis, J. Appl. Phys. 94, 3875, (2003).
[21] V. Popa, T. Braniste, M. A. Stevens-Kalceff, D. Gerthsen, P. Brenner, V. Postolache, V. Ursaki, and I. M. Tiginyanu, J. Nanoelectron. Optoelectron. 7, 730, (2012).
[22] M. V. Calin, V. V. Ursaki, I.M. Tiginyanu, L. Syrbu, V. P. Shontea, D. Esinenco, and S. Albu, Mold. J. Phys. Sci., vol.2, p. 62, (2003).

[23] V. Postolache, Proc. 2nd International Conference on Nanotechnologies and Biomedical Engineering, Chisinau, Republic of Moldova, April 18-20, (2013).
[24] H.-Y. Chen, R.-S. Chen, N. K. Rajan, F.-C. Chang, L.-C. Chen, K.-H. Chen, Y.-J. Yang, and M. A. Reed, Phys. Rev. B 84, 205443, (2011).
[25] C. Soci, A. Zhang, B. Xiang, S. A. Dayeh, D. P. R. Aplin, J. Park, X. Y. Bao, Y. H. Lo, and D. Wang, Nano Lett. 7, 1003 (2007).
[26] H. Kind, H. Yan, B. Messer, M. Law, and P. Yang, Adv. Mater. (Weinheim, Germany) 14, 158, (2002).
[27] Q. H. Li, Y. X. Liang, Q. Wan, and T. H. Wang, Appl. Phys. Lett. 85, 6389, (2004).
[28] S. Kumar., V. Gupta, and K. Sreenivas, Nanotechnology 16, 1167, (2005).
[29] D. Cammi and C. Ronning, Adv. Cond. Matter Phys. 2014, 184120, (2014).
[30] Ed. Monaico, V. Postolache, E. Borodin, V. V. Ursaki, O. Lupan, R. Adelung, K. Nielsch, and I. M. Tiginyanu, Semicond. Sci. Technol. 30, 035014, (2015).
[31] O. Volciuc, T. Braniste, I.Tiginyanu, M. A. Stevens-Kalceff, J.b Ebeling, T. Aschenbrenner, D. Hommel, V. Ursaki, and J. Gutowski, Appl. Phys. Lett. 103, 243113, (2013).
[32] V. Zalamai, A. Burlacu, V. Postolache, E.V. Rusu, V.V. Ursaki, and I.M. Tiginyanu, Mold. J. Phys. Sci. 9 (3–4), 308, (2010).
[33] M. Smirnov, A. P. Rambu, C. Baban, and Gh. I. Rusu, J. Adv. Res. Phys. 1, 021011, (2010).

STACKING INTERACTIONS IN THE CRYSTAL STRUCTURES OF MIXED LIGAND SQUARE-PYRAMIDAL COPPER(II) COMPLEXES WITH AROMATIC 1,10-PHENANTHROLINE OR 2,2′-BIPYRIDINE LIGANDS AND ACETYLACETONATE

Elena Melnic

Institute of Applied Physics, Academy of Sciences of Moldova,
5 Academia str. MD-2028, Chisinau, Republic of Moldova

E-mail: melnic@phys.asm.md

(Received December 01, 2016)

Abstract

Four novel mononuclear square-pyramidal complexes with composition [Cu(acac)(phen)(DMF)]BF_4 (**1**), [Cu(acac)(phen)(H_2O)]BF_4 (**2**), [Cu(acac)(phen)(NO_3)]MeOH (**3**) and [Cu(acac)(phen)Cl]MeOH (**4**), (phen = phenanthroline and acac = acetylacetonate) have been synthesized and characterized by single-crystal X-ray diffraction. The supramolecular structures of these novel complexes and related complexes found in the Cambridge Structural Database (CSD), which contain a planar [Cu(acac)(AA)] fragment, where AA denotes phen or 2,2′-bipyridine (bipy)/4,4′-dimethyl-2,2′-dipyridine (Me_2bipy), have been analyzed from in terms of stacking interactions in these systems.

1. Introduction

Noncovalent interactions of aromatic and other π-systems referred to as "π–π stacking" or "stacking interactions" and generally observed in the crystal structures are recognized as specific parallel or about parallel mutual arrangements of interacting fragments. These interactions take place in different settings; they affect the intercalation into DNA, host–guest complexations, and interactions in proteins [1]. These interactions play an important role in crystal packing [2−5], self-assembly processes [6], recognition of aromatic compounds [7−9], and regulation of selectivity in organic reactions [10]; they are significant in biological systems [11]. In the field of crystal engineering, the importance of these weak interactions for the design and control of molecular organization in the solid state has been well recognized; however, the predictability of their existence and settings in the final assembly is still challenging.

These interactions are dominated by dispersion forces with significant contributions of electrostatics and hydrogen bonding [12, 13]. Stacking interactions of organic aromatic molecules have been extensively investigated [14–17]. The most stable stacking interaction for a benzene dimer is a parallel-displaced geometry at an interaction energy of –2.73 kcal/mol [18]. In the context of understanding the fundamentals of stacking interactions, benzene and substituted benzene dimers have been studied to determine the effects of electrostatics, dispersion and charge transfer on stacking stabilization. The energies of stacking interactions of benzene with a chelate ring have been calculated [14]; the results show that chelate–benzene stacking interactions are

remarkably stronger than benzene–benzene interactions. In the arrangement of aromatic rings one can distinguish generally between a stacked arrangement, and an edge- or point-to-face, T-shaped conformation [19]. Stacking does not necessarily assume only a perfect face-to-face alignment of π-systems; more often, it can be an offset or slipped packing.

The involvement of planar chelate rings (metallacycles) of transition metals complexes in the stacking interactions have been recently recognized and described [20]. It has been shown that the geometries of stacking interactions between chelate rings [21] or between chelate rings and aromatic rings [22] are similar to stacking interactions between the aromatic rings.

Rational design of metal-organic materials with required architecture and properties is in focus of crystal engineers and materials scientists. In terms of crystal engineering, π–π stacking interactions are relatively weak and also only weakly directional. They are therefore difficult to predict and control, especially in the presence of other stronger interactions, such as strongly directional coordination and hydrogen bonds.

The ability of first-row transition metals to form complexes with ligands, such as 1,10-phenanthroline (phen), 2,2'-bipyridine (bipy) or acetylacetonate (acac), is well known. Interest in copper complexes of phen and 2,2'-bipy is stemming from their potential application as antimicrobial, antiviral, anti-inflammatory, antitumor agents, enzyme inhibitors, or chemical nucleases. From crystal engineering perspective, the square-pyramidal Cu(II) complexes with chelating aromatic ligands are attractive candidates to design extended supramolecular architectures by π–π interactions involving metallacycles [23–25].

The aromatic chelate ligands attached to copper(II) (bipy, phen and related molecules) favor the intermolecular π–π stacking interactions involving metallacycle; these interactions play an important role in sustaining extended supramolecular solid-state architectures [26]. The phen molecule coordinating to a metal ion forms a large planar system of four fused rings: two pyridine fragments, one C_6-ring and one chelate ring [27] and the smaller bipy ligand, which comprises three rings with the metal ion (two pyridine and one chelate rings) and exhibiting an increasing tendency to form stacking interactions with the π-systems of various aromatic groups [28]. The tendency for stacking interactions to occur is an important issue when using phenanthroline complexes in various fields; it facilitates the prediction of crystal structure architecture [29–31]. The preservation of robust π–π stacking motifs in crystal and even in solution has been widely explored and summarized in a number of research and review articles [19, 32–39].

For the systematical study of the geometry of the stacking interactions with participation of a chelate ring in the structures of square-pyramidal Cu(II) complexes, four novel neutral and cationic complexes containing a [Cu(acac)(phen)] fragment have been synthesized and structurally characterized by single-crystal X-ray diffraction. The statistical analysis of the geometry of stacking interaction in these novel compounds and all available literature data including the related complexes with [Cu(acac)(bipy)] and [Cu(acac)(Me_2bipy)] fragments has been carried out.

2. Results and discussion

Four novel mononuclear complexes with compositions [Cu(acac)(phen)(dmf)]BF_4 (**1**), [Cu(acac)(phen)(H_2O)]BF_4 (**2**), [Cu(acac)(phen)(NO_3)]MeOH (**3**) and [Cu(acac)(phen)Cl]MeOH (**4**) were synthesized by interaction of $Cu(BF_4)_2 \cdot H_2O$ (for **1** and **2**), $Cu(NO_3)_2 \cdot 2H_2O$ (for **3**) and $CuCl_2 \cdot 3H_2O$ (for **4**) with phen and acac. Components were dissolved in a MeOH/DMF mixture for **1** and **4** and a MeOH/THF mixture for **3** and in MeOH for **2,** MeOH = methanol;

DMF = demethylformamide; THF = tetrahydrofuran.

The crystal structures of all compounds were investigated by single-crystal X-ray diffraction. Diffraction data for **1**−**4** were recorded at room temperature on an Oxford Diffraction Xcalibur diffractometer equipped with a CCD area detector and a graphite monochromator utilizing MoK_α radiation. Final unit cell dimensions were obtained and refined on an entire data set. Structures were solved by direct methods using the SHELX-97 program package [40] and refined with the full-matrix least-squares method with anisotropic thermal parameters for the non-hydrogen atoms. All compounds crystallize in the triclinic system, space group *P*-1. In all structures, the C(sp^2)-bound H atoms were placed in calculated positions and treated using a riding model approximation with $U_{iso}(H) = 1.2U_{eq}(C)$; H atoms of the methyl groups were found and refined using AFIX 137 instruction and $U_{iso}(H) = 1.5U_{eq}(C)$, while the O-bound hydrogen atoms were found from differential Fourier maps at intermediate stages and their positions were refined using restrains. Figures were produced by Mercury [41]. X-ray data and details of the refinement for **1**−**4** are summarized in Table 1.

Crystallographic data in CIF format for **1**−**4** reported herein were deposited with the Cambridge Crystallographic Data Centre and allocated the deposition numbers **CCDC 1520778-1520781**. These data can be obtained free of charge from the Cambridge Crystallographic Data Centre via www.ccdc.cam.ac.uk/data_request/cif.

Table 1. Crystal and structure refinement data for **1**–**4**

Compound	**1**	**2**	**3**	**4**
Empirical formula	$C_{20}H_{22}N_3O_3B_1F_4Cu$	$C_{17}H_{17}N_2O_3B_1F_4Cu$	$C_{17.5}H_{17}N_3O_{5.5}Cu$	$C_{18}H_{19}N_2O_3Cl_1Cu$
Formula weight	502.75	447.67	420.88	410.34
T (K)	293(2)	293(2)	293(2)	293(2)
Crystal system	Triclinic	Triclinic	Triclinic	Triclinic
Space group	*P*-1	*P*-1	*P*-1	*P*-1
Z	2	2	2	2
a, Å	9.8080(7)	8.3319(7)	8.6096(9)	8.9974(7)
b, Å	11.2159(8)	11.0211(10)	10.2314(7)	9.2215(7)
c, Å	12.0344(8)	12.1245(13)	12.1027(13)	12.0605(10)
α, (º)	62.796(7)	65.264(9)	105.200(7)	102.498(7)
β, (º)	73.679(6)	78.974(8)	104.230(9)	97.666(7)
γ, (º)	72.459(6)	68.614(8)	108.009(7)	106.561(7)
V, $Å^3$	1106.5(2)	940.6(2)	914.2(2)	915.84(13)
D_{calc} (g cm^{-3})	1.509	1.581	1.529	1.488
μ(mm^{-1})	1.047	1.220	1.231	1.357
F(000)	514	454	432	422
Reflections collected/unique	7405/4921	6325/ 4184	5021/3211	5356/3386
Reflections with $I > 2\sigma(I)$	3044	2660	2193	2357
Data/restraints/parameters	4921 / 0 / 293	4184 / 3 / 261	3211 / 13 / 257	3386 / 0 / 231
GOF on F^2	1.000	0.999	0.999	1.001
R_1, wR_2 [$I > 2\sigma(I)$]	0.0681, 0.1322	0.0631, 0.1415	0.0617, 0.1419	0.0548, 0.0996
R_1, wR_2 (all data)	0.1140, 0.1700	0.1097, 0.1805	0.0975, 0.1628	0.0892, 0.1157
$\Delta\rho_{max}$, $\Delta\rho_{min}$, (e·$Å^{-3}$)	0.696, -0.503	0.397, -0.316	0.744, -0.347	0.369, -0.442

The structures of all compounds reveal square pyramidal 4+1 copper (II) N_2O_3 environment in **1**, **2**, **4** and N_2O_2Cl in **3**, where the equatorial planes are fixed by the chelate acac and phen ligands, which form six- and five-membered metallacycles, respectively (Fig. 1). Axial position is occupied by oxygen atom of DMF in **1**, H_2O in **2**, NO_3 in **3** and chlorine atom in **4**. Complexes **1** and **2** are cationic and comprise BF_4^- counteranions in the structure, while complexes **3** and **4** are neutral methanol solvates. In **1**, **2** and **3** the distances in equatorial plane are in the range Cu–O 1.890–1.919 Å, Cu–N 2.004–2.015 Å, and $Cu–O_{(axial)}$= 2.340–2.366 Å, while in **4** these distances are Cu–O 1.919–1.923 Å, Cu–N 2.016–2.031 Å, and $Cu–Cl_{(axial)}$ = 2.529 Å. In crystal **1** two mononuclear units related by a center of symmetry exhibit extended π–π stacking interactions involving both metallacycles and chelate phen ligands, which overlap in a face-to-face manner with an interplanar separation 3.316 Å and centroid···centroid distances of 3.783, 3.629, and 3.601 Å for acac metallacycle···phenyl moiety of phen, acac metallacycle···pyridine moiety of phen and phen metallacycle···phen metallacycle pairs, respectively (Fig. 1a). The distance between the copper atoms within the supramolecular dimers is 5.267 Å.

The molecular packing in crystal structure **2** reveals the intermolecular π–π stacking interactions between the center symmetry related complexes with interplanar separation of 3.390 Å and the distance between centroids of phen metallacycle and pyridine moiety of the phen ligand of 3.580 Å. The acac is not involved in stacking and dimer formation. These dimers are further stacked with the neighbor one by another side of the phen ligand with the shortest distance between centroids of the overlapped ring of 3.469 Å and interplanar spacing of 3.285 Å (Fig. 1b). These interactions result in a well-defined and easily recognized extended 1-D supramolecular motif along the crystallographic *c* axis.

In neutral complexes **3** and **4** the centre symmetric dimer is formed due to stacking interaction of exclusively acac metallacycles which lie in parallel planes with separations of 3.478 and 3.637 Å and centroid···centroid distances of 3.444 Å and 3.591 Å, respectively. As in the case of **1** and **2**, these dimers further interact through staking interactions involving phen ligands by overlaping of the phenyl and pyridine moieties. Interplanar phen···phen separations of 3.176 and 3.331 Å, distances between centroids within the dimer are 3.697 and 3.797 Å, for **3,** and **4**, respectively (Figs. 1c, 1d). The crystal structures of **3** and **4** revealed again the infinite supramolecular motifs along the [011] crystallographic direction.

The structures of studied complexes revealed that the [Cu(acac)(phen)] fragment is involved in stacking interactions involving metallacycles; these interaction represents the reliable supramolecular synthon suitable to generate a robust supramolecular motif. To investigate the reliability of this supramolecular synthon, all the available reported structures containing the planar [Cu(acac)(phen)] fragment and related [Cu(acac)(bipy)] or [Cu(acac)(Me_2bipy)] were analyzed in terms of stacking interactions in these systems using Cambridge Structural Database (CSD) (version 5.37, 2016).

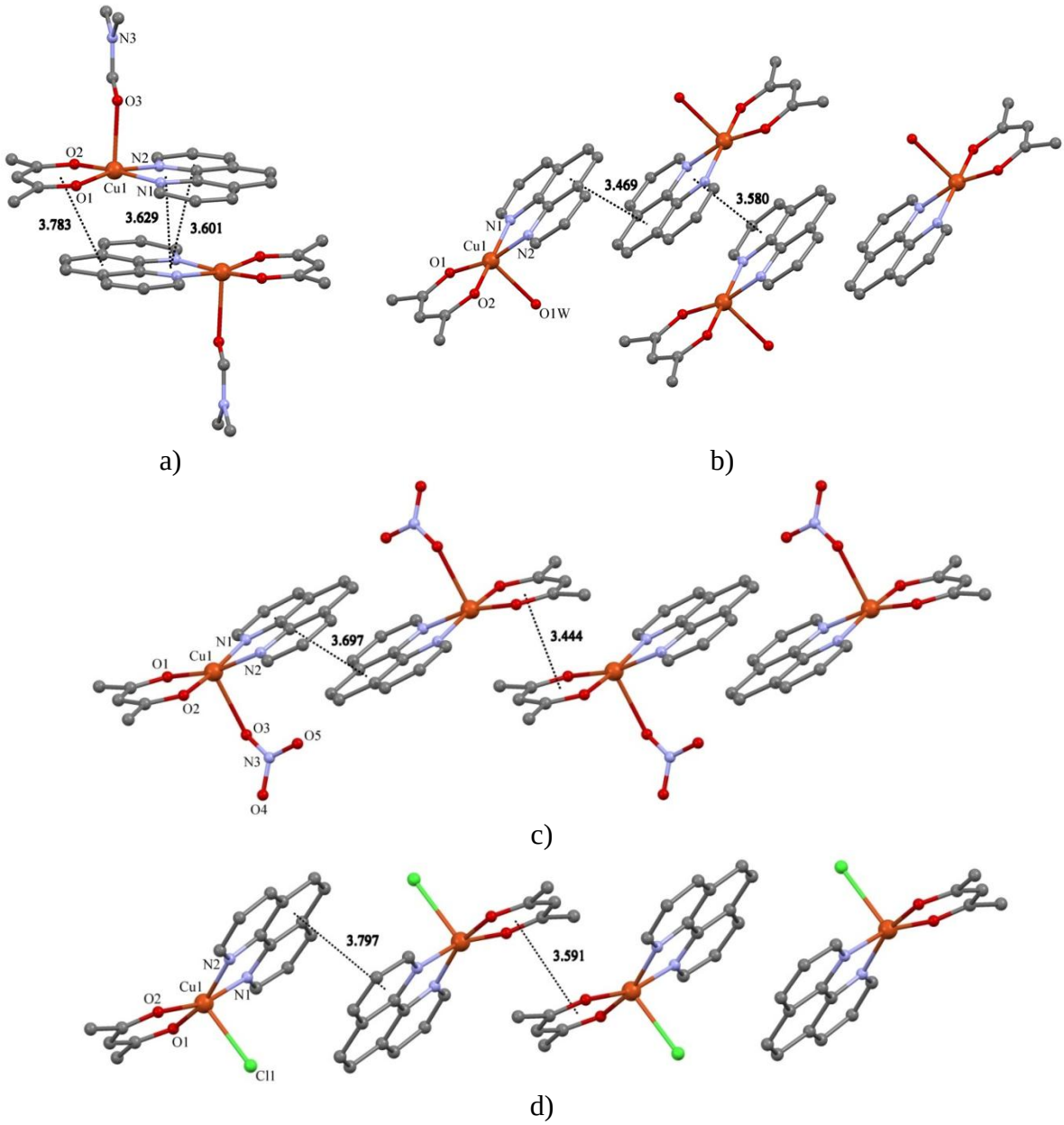

Fig. 1. Stacking interactions in cationic (a) [Cu(acac)(phen)(DMF)]BF_4 (**1**), (b) [Cu(acac)(phen)(H_2O)]BF_4 (**2**) and neutral (c) [Cu(acac)(phen)(NO_3)]MeOH (**3**), and (d) [Cu(acac)(phen)Cl]MeOH (**4**) complexes.

3. Searching methods

The quest in CSD revealed 29 original hits for the [Cu(acac)(phen)] fragment, 19 original hits for the [Cu(acac)(bipy)] fragment, and 5 original hits for the [Cu(acac)(Me_2bipy)] fragment. The structures for which atomic coordinates were not available or structures containing non-pyramidal complexes, or co-crystals containing another planar complex (in total 7 hits) were excluded from further consideration. Thus, 49 structures including four reported above

complexes were analyzed. To find intermolecular stacking interactions between [Cu(acac)(AA)] fragments, where AA denotes phen or 2,2′-bipyridine (bipy)/4,4′-dimethyl-2,2′-dipyridine (Me_2bipy) aromatic molecule, at least one of three searching criterions should be satisfied: the first criterion assumes that the distance between centroids of ligand aromatic rings of the neighboring [Cu(acac)(AA)] is below 4.6 Å [19]; the second criteria assumes that the distance between centers of aromatic ring and chelate ring (metallacycles) is shorter than 4.3 Å; and the third criterion is that the distance between centroids of the chelate rings (metallacycles) is below 4.2 Å. (Tables 2, 3). Only one from 49 analyzed structures did not reveal stacking interactions, while 98% of the analyzed structures revealed stacking interactions.

4. Stacking interactions of [Cu(acac)(phen)] fragments

The phenanthroline molecule coordinating to a copper ion forms a large planar system of four fused rings: two pyridine rings, one C_6-ring (*phenyl ring*) and one chelate ring. Using the above mentioned criteria, 30 structures with 123 interactions between complexes were found including the four novel structures reported above. In all structures, two complexes are oriented in "head-to–tail" manner (Fig. 2); however, they show many different overlap geometries resulting in different Cu···Cu intermolecular distances within the dimer formed by stacking interactions.

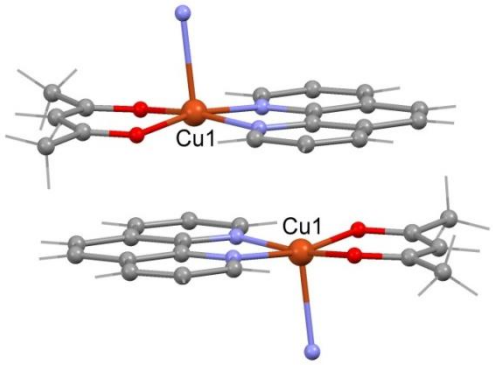

Fig. 2. Head-to-tail orientation of the [Cu(acac)(phen)] fragments.

Based on the preliminary analysis of possible interacting geometries, six types of mutual arrangement of fragments in the stacking were identified (Fig. 3). The group of structures with overlap type I is the most numerous and includes 17 structures and 85 interactions (Table 2).

The intermolecular distances between the centroids of any ring in the dimer: $d_{Py\text{-}Py}$, $d_{Ph\text{-}Py}$, $d_{Py\text{-}M}$, $d_{ac\text{-}Py}$, $d_{Ph\text{-}Ph}$, $d_{Ph\text{-}M}$, $d_{Ph\text{-}ac}$, $d_{ac\text{-}M}$, and $d_{\ ac\text{-}ac}$ were measured. Distances $d_{Py\text{-}Py}$, $d_{Ph\text{-}Py}$, $d_{Py\text{-}M}$, and $d_{ac\text{-}Py}$ are the intermolecular separations between the centroids of two pyridine fragments, one pyridine fragment and C_6-ring, one pyridine fragment, two chelate rings and two C_6-rings, respectively. The values $d_{Ph\text{-}M}$ and $d_{Ph\text{-}ac}$ are distances between the centroids of C_6 and chelate rings (metallacycle); however, $d_{ac\text{-}M}$ and $d_{ac\text{-}ac}$ are the distances between two chelate rings (metallacycles), respectively (Table 2). In the structures with relatively short Cu···Cu distance (3.562–5.604 Å) in the stacking, an overlap takes place according to types **I** (17 hits) and **VI** (4 hits)**.** Type **I** shows the most extended overlap area and includes both metallacycles and phen rings (Figs. 3a, 3f) [23, 25, 42–45], and for type **VI** the only acac metallacycles are overlapped [46, 47] and result in the shortest centroid···centroid distances of 3.200–3.591 Å. The overlap

according to type **II** with the Cu···Cu distance in a range of 5.732–6.713 Å was found in **6** structures and involves phen metallacycles and penyl C_6 moiety, as well as pyridine···pyridine moiety of phen ligands, in stacking (Fig. 2b). Overlap types **III** (7 hits) and **IV** (7 hits) are somewhat similar; only the rings of phen ligands participate in the overlap: phenyl···pyridine and pyridine···pyridine overlap takes place in **III**, and phenyl···phenyl and phenyl···pyridine in **IV** (Figs. 3c, 3d) [44, 46–51]. The Cu···Cu distances are in a range of 8.344–9.270 Å. Metallacycles are not involved in the overlapping for type **III** and **IV**. Only two hits were found for type **V** overlap with a small overlapping area (Fig. 2e) and Cu···Cu distances of 6.591 and 6.627 Å [48, 49]. Only in one crystal structure (Ref.code KEBYOG) [46] no π–π stacking interaction was found between the complexes. A histogram of hit distribution over the different types of [Cu(acac)(phen)] overlap in the stacking is shown in Fig. 4.

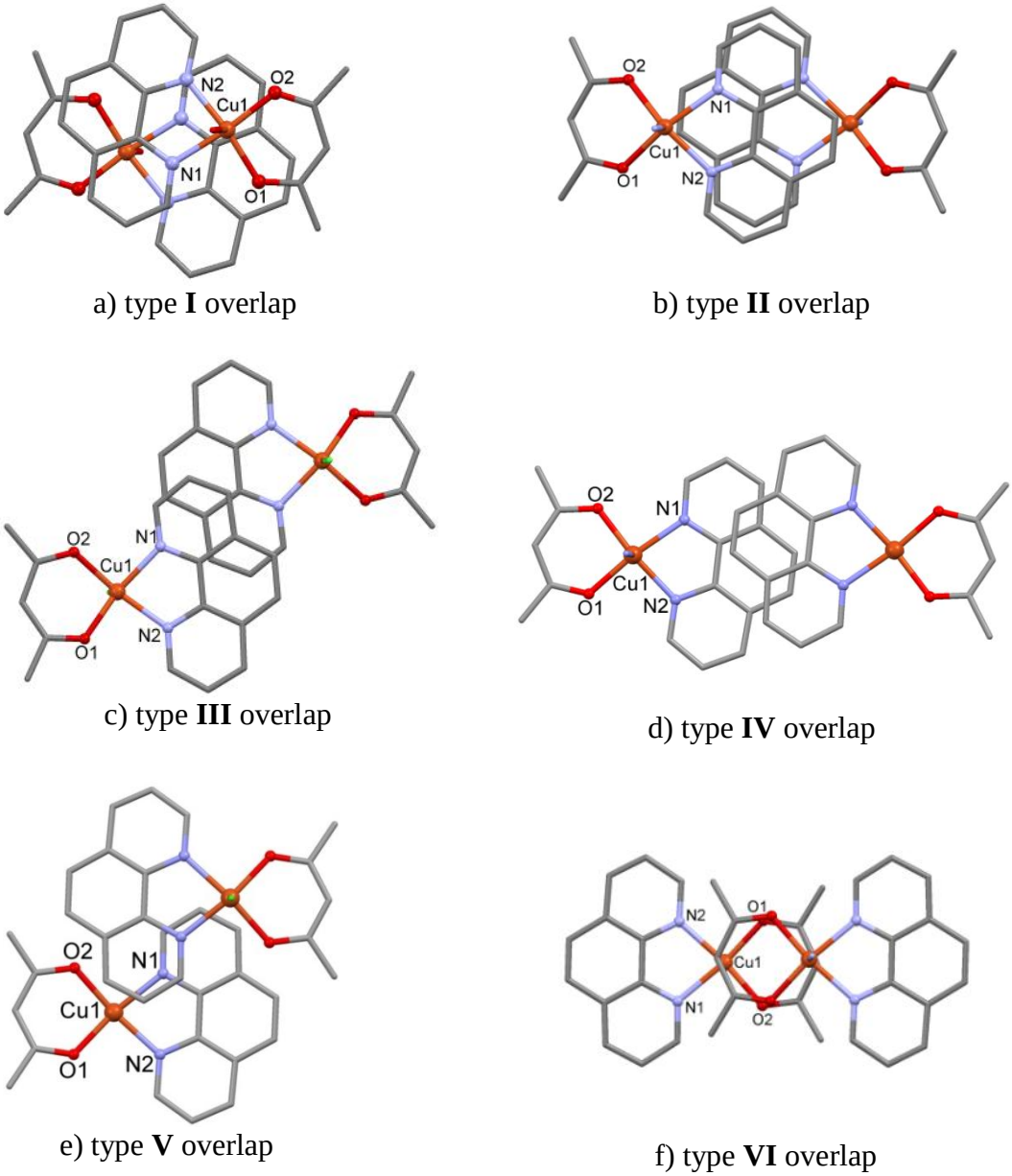

a) type **I** overlap

b) type **II** overlap

c) type **III** overlap

d) type **IV** overlap

e) type **V** overlap

f) type **VI** overlap

Fig. 3. The different types of [Cu(acac)(phen)] fragment overlap in stacking; view perpendicular to the plane of the overlapping fragments.

Table 2. Parameters of stacking interactions in the structures of complexes with the [Cu(acac)(phen)] fragment

Composition, Space group	overl ap type	Centroid–centroid distances (Å)										*P-to-P* distance or angle (Å/°)*	Cu—Cu distance (Å)	Reference, refcode in CSD
		$d_{Py\text{-}Py}$	$d_{Ph\text{-}Py}$	$d_{Ph\text{-}Ph}$	$d_{Py\text{-}M}$	$d_{Ph\text{-}M}$	$d_{ac\text{-}Ph}$	$d_{ac\text{-}Py}$	$d_{ac\text{-}M}$	$d_{ac\text{-}ac}$	$d_{M\text{-}M}$			
[Cu(acac)(hfac)(phen)], *P*-1	I, IV	3.820	3.983	3.475	3.884	3.967	3.671	—	—	—	3.465	3.361/3.417	5.178/8.677	[44] ACFCUA
[Cu(acac)(phen)(OH_2)][hfac]·H_2O, *P*-1	I, III	3.970/ 3.594	3.994	—	3.675	4.151	3.760	—	—	—	3.698	3.352/3.344	5.324/8.344	[44] ACFCUB
[Cu(acac)(phen)(H_2O)]ClO_4, *P*-1	I, IV	—	3.951	3.729	—	—	—	3.709	3.594	—	—	3.350/3.439	3.744/9.168	[44] ACIFIC
[{Cu(acac)(phen)}$_2${Ni(CN)$_4$}]·H_2O, *P*-1	I, IV	3.978	3.735	4.025	3.646	4.151	3.827	—	—	—	3.865	3.329/3.372	5.604/9.153	[25] DOZSER
[{Cu-(acac)(phen)}$_2$(μ-bpp)](ClO_4)$_2$·$6H_2O$, $P4_2/n$	I, IV	—	3.950	3.639	3.944	—	3.973	3.646	—	—	4.160	3.350/3.428	4.810/8.990	[24] FAZZIQ
[Cu(acac)(phen)Cl], *P*-1	III, V	3.843/ 3.744	3.763	—	3.923	—	—	—	—	—	—	3.443/3.234	8.520/6.591	[48] FOWJEH
[Cu(acac)(phen)(NCS)], *P*-1	II	3.523	3.937	4.235	3.983	3.561	—	—	—	—	—	3.480	6.668	[23] JAJSOD
[{Cu(acac)(phen)(NCS)}$_2${($ClHg)_2$(NCS)$_2$}], *P*-1	I	—	—	—	—	—	3.752	3.469	3.809		4.058	3.347	3.825	[23] JAJTAQ
[{Cu(acac)(phen)(NCS)}$_2$ $Hg(SCN)_2$], *C*2/*c*	II	3.710	3.740	4.203	—	3.625	—	—	—	—	—	3.522	6.713	[23] JAJTEU
[{Cu(acac)(phen)}$_2$ ($\mu_{1,1}$-N_3)](ClO_4)}·$2H_2O$, *P*-1	IV,VI	—	3.653	4.080	—	—	—	—	—	3.430	—	3.193/3.459	8.956/5.167	[46] KEBYIA
[Cu(acac)(phen)(H_2O)]NO_3} (NO_3)·H_2O, *P*-1	II	3.549	4.046	4.406	3.884	3.530	—	—	—	—	—	3.484	6.203	[52] KUZWAD
[Cu(acac)(phen)Br], *P*-1	III, V	3.986/ 3.754	3.900	—	3.928	—	—	—	—	—	—	3.533/3.297	8.745/6.627	[49] LIVNOU
[Cu(acac)(phen)]BPh_4, *P*-1	I	—	—	—	—	—	3.593	3.859	3.582	—	—	3.437	3.562	[42] NEKBUC
[Cu(acac)(phen)(dmso)]BPh_4, *P*-1	I	—	—	—	3.671	—	3.644	4.046	—	—	—	3.279	4.902	[42] NEKCEN
[Cu(acac)(phen)(dmf)]BPh_4, $P2_1/c$	I	—	—	—	—	—	3.688	3.589	3.659	—	—	3.377	3.815	[42] NEKCIR
[Cu(acac)(phen)(acetone)]BPh_4, *P*-1	I	—	—	—	3.683	—	3.636	4.004	—	—	—	3.273	4.853	[42] NEKCOX
[Cu(acac)(phen)(CH_3CN)] (CH_3CN) BPh_4, *P*-1	II	3.797	3.867	—	3.403	3.927	—	—	—	—	—	3.256	6.153	[42] NEKCUD
[Cu(acac)(phen)](CH_3NO_2) BPh_4, *P*-1	II	3.678	4.052	—	3.477	3.748	4.181	—	—	—	—	3.308	5.732	[42] NEKDAK
[Cu(acac)(phen)(py)]BPh_4, *P*-1	I	—	—	—	—	—	3.631	3.568	3.941	—	—	3.370	4.134	[42] NEKFAM
[Cu(acac)(phen)(hmpa)]BPh_4, *C*2/*c*	II	3.782	3.767	—	3.518	3.782	—	—	—	—	—	3.389	6.365	[42] NEKFEQ
[Cu(acac)(phen)(NO_3)]·H_2O, *C*2/*c*	I, III	3.745	3.668	—	3.942	3.842	3.754	—	—	—	3.585	3.375/3.364	5.463/8.886	[50] OCOKOG
[Cu(acac)(phen)$_2$Ag(CN)$_2$](ClO_4), *P*-1	I	3.700	—	—	3.792	3.914	3.736	—	—	—	—	3.385	5.372	[43] RELSEH
[Cu(acac)(phen)$_2$Au(CN)$_2$](ClO_4), *P*-1	I	3.644	—	—	3.854	—	3.656	3.757	—	—	—	0.54	4.695	[43] RELSIL
[{Cu(acac)(phen)}$_2${Au(CN)$_2$}] (ClO_4)·0.5CH_3CN, *P*-1	I	—	3.974	—	—	—	—	3.690	3.596	—	—	3.323/0.64	3.693/8.47	[43] RELSOR
[Cu(acac)(phen)(C_2N_3)]·H_2O, *P*-1	III, VI	—	3.781	4.245	—	—	—	—	—	3.200	—	3.418/3.255	9.270/5.011	[47] SUXRUZ
[Cu(acac)(phen)(ClO_4)][Cu(acac) (phen)(CH_3CN)]ClO_4, $P2_1/c$	III	4.082	3.837	—	—	—	—	—	—	—	—	3.657	8.437	[51] YOTXOU
[Cu(acac)(phen)(DMF)]BF_4, *P*-1	I	3.905	—	—	3.601	4.086	3.783	—	—	—	3.629	3.316	5.267	Compound **1**
[Cu(acac)(phen)(H_2O)]BF_4, *P*-1	I, IV	3.938	—	3.460	3.580	4.060	4.043	—	—	—	3.790	3.390/3.285	5.609/9.252	Compound **2**
[Cu(acac)(phen)(NO_3)]MeOH, *P*-1	IV, VI	—	3.697	4.025	—	—	—	—	—	3.444	—	3.176/3.478	9.095/5.190	Compound **3**
[Cu(acac)(phen)Cl]MeOH, *P*-1	III, VI	3.812	3.797	—	—	—	—	—	—	3.591	—	3.331/3.637	8.620/5.641	Compound **4**

* interplanar distance or dihedral angle between about parallel planes.

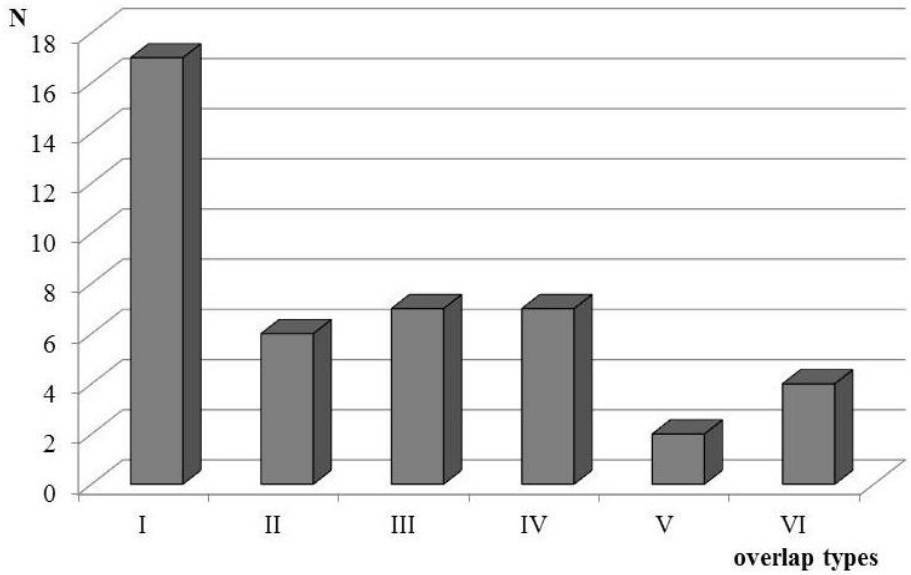

Fig. 4. Histogram of hit distribution over the different types of [Cu(acac)(phen)] overlap in the stacking

Histogram 4 and Table 2 show that metallacycles are involved in stacking interactions in 29 from 30 analyzed structures (96.7%) (overlap types **I**, **II**, **V,** and **VI**).

5. Stacking interactions of [Cu(acac)(bipy)] or [Cu(acac)(Me$_2$bipy)] fragments

A similar analysis was conducted for the related complexes containing planar [Cu(acac)(bipy)] or [Cu(acac)(Me$_2$bipy)] fragments with less extended aromatic systems. The quest in CSD revealed 18 crystal structures of square-pyramidal complexes: 15 with [Cu(acac)(bipy)] and 3 with [Cu(acac)(Me$_2$bipy)] fragments. Analysis of search results showed that bipy/Me$_2$bipy copper(II) complexes can have two different orientations, namely, head-to-tail and "head-to-head" (Fig. 5).

Based on the analysis of possible interacting geometries of [Cu(acac)(bipy)] or [Cu(acac)(Me$_2$bipy)] fragments, six types of mutual arrangement of fragments in the stacking were identified (Fig. 6). Fourteen structures have a head-to-tail orientation and overlap in four modes (Figs. 6a, 6b, 6e, 6f); four structures are oriented head-to-head (Figs. 6c, 6d) [23, 25, 42, 43, 49, 53]. The intermolecular distances between the centroids of any ring in the dimmer—$d_{Py\text{-}Py}$, $d_{Py\text{-}M}$, $d_{ac\text{-}py}$, $d_{ac\text{-}ac}$, $d_{ac\text{-}M}$, $d_{M\text{-}M}$—were analyzed. Distances $d_{Py\text{-}Py}$,$d_{Py\text{-}M}$ and $d_{ac\text{-}Py}$ are the intermolecular separations between the centroids of two pyridine fragments, one pyridine fragment and chelate ring, respectively. Separations $d_{ac\text{-}ac,}$ $d_{ac\text{-}M,}$ and $d_{M\text{-}M}$ are distances between the centroids of two chelate rings, respectively (Table 3). The group of structures with the overlap of type **I**, which is similar to that found for the [Cu(acac)(phen)] fragment (Fig. 2a), is the most numerous and includes 9 structures and 24 interactions (Table 3). In the structures with a relatively short Cu···Cu distance (3.570–5.475 Å) in the stacking, the overlap takes place according to types **I** (9 hits), **III** (3 hits), **IV** (1 hit), and **VI** (3 hits). Type **I** shows the most extended overlap area and includes both metallacycles and bipy/Me$_2$bipy rings (Figs. 6a, 6f) [23, 25,42, 43, 46]; for type **VI,** only acac metallacycles overlap [46, 53, 55] and result in the shortest centroid···centroid distances of 3.310–3.495 Å. The overlap in accordance with type **II** with the

Cu···Cu distance in a range of 7.410–7.820 Å was found in five structures and involves only the pyridine···pyridine moiety of bipy/Me_2bipy ligands in stacking (Fig. 6b) [23, 25, 43, 53].

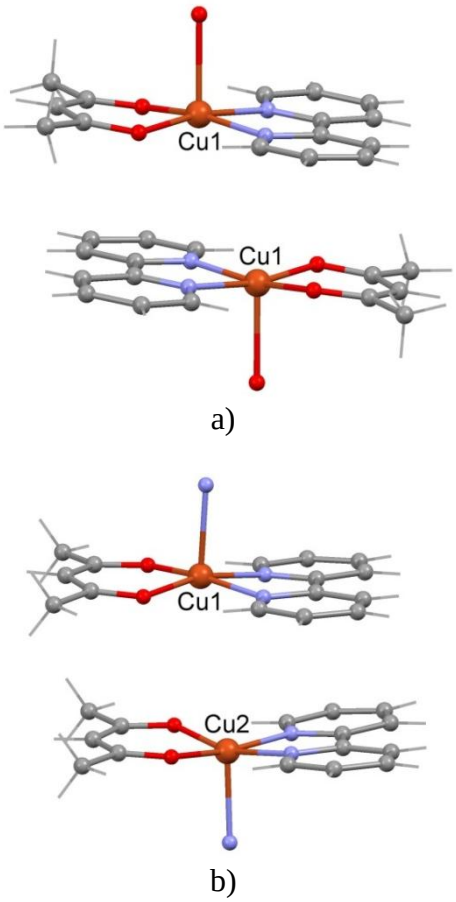

Fig. 5. Orientations of the [Cu(acac)(bipy)] or [Cu(acac)(Me_2bipy)] fragments:
(a) head-to-tail and (b) head-to-head orientation

Overlap types **III** (3 hits) and **IV** (1 hit) are similar; both exhibit a head-to-head orientation; however, in contrast to overlap type **III,** overlap **IV** revealed a perfect face-to-face alignment and a non-parallel mutual stacking arrangement without offset (Figs. 6c, 6d) [23, 25, 49, 53]. The Cu···Cu distances are in a range of 3.920–4.699 Å.

Only one hit was found for type **V** overlap with a small overlapping area involving only the pyridine···pyridine moiety of bipy in stacking with Cu···Cu distances of 8.860 Å (Fig. 6e) [54]. A histogram of hit distribution over the different types of [Cu(acac)(bipy)] or [Cu(acac)(Me_2bipy)] overlap in the stacking is shown in Fig. 7).

a) type **I** overlap

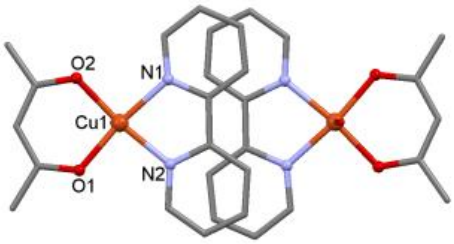

b) type **II** overlap

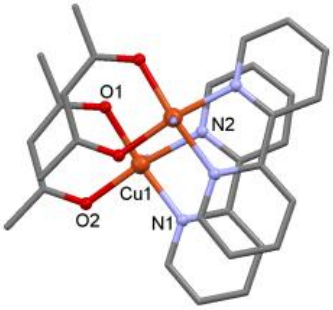

c) type **III** overlap

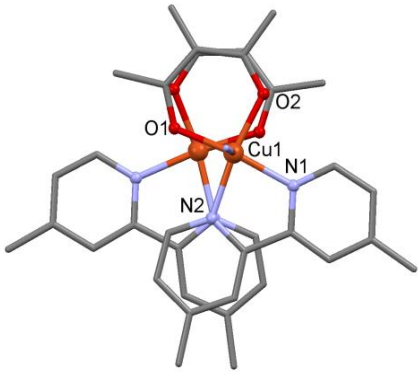

d) type **IV** overlap

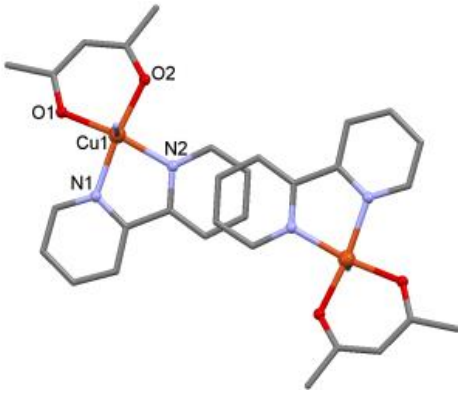

e) type **V** overlap

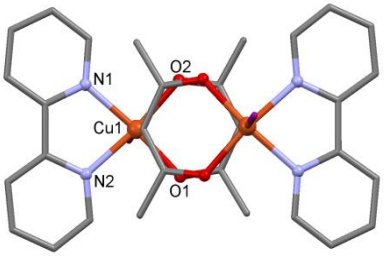

f) type **VI** overlap

Fig. 6. The different types of overlap of [Cu(acac)(bipy)] or [Cu(acac)(Me_2bipy)] fragments in stacking; view perpendicular to the plane of the overlapping fragments.

Table 3. Parameters of stacking interactions in the structures of complexes with [Cu(acac)(bipy)] or [Cu(acac)(Me_2bipy)] fragments

Composition, Space group	overlap type	Centroid–centroid distances (Å)						P-to-P distance or angle (Å/°)*	Cu–Cu distance (Å)	Reference, refcode in CSD
		$d_{Py\text{-}Py}$	$d_{ac\text{-}py}$	$d_{ac\text{-}ac}$	$d_{ac\text{-}M}$	$d_{Py\text{-}M}$	$d_{M\text{-}M}$			
[{Cu(acac)(bipy)}$_2${Ni(CN)$_4$}], *P*-1	III	3.776	–	4.001	–	3.575	3.909	3.25	4.246	[25] DOZSIV
[Cu(acac)(bipy)(H_2O)]2[Ni(CN)$_4$], $P2_1/c$	II	3.653	4.216	–	3.808	–	3.928	3.420/3.405	3.950/7.410	[25] DOZSOB
[(Cu(acac)(Me_2bipy)]$_2$[Ni(mnt)$_2$], *P*-1	I	–	3.826	–	3.620	–	–	3.484	3.753	[25] DOZSUH
[Cu(acac)(bipy)Cl][Cu(acac)(bipy)(H_2O]Cl·H_2O, *P*-1	II, VI	3.829	–	3.310	–	–	–	3.064/2.95	7.617/5.105	[53] EBEDOG
[Cu(acac)(bipy)Br]H_2O, *P*-1	III	3.888	–	4.159	3.721	3.992	4.171	2.95	4.620	[53] EBEDUM
[Cu(acac)(Me_2bipy)(NCS)], *C*2/*c*	II, IV	3.825/ 3.591	–	3.325	–	4.053	–	3.494/2.2	7.547/3.920	[23] JAJSIX
[{Cu(acac)(Me_2bipy)(NCS)}$_2$Hg(SCN)$_2$], *P*-1	I, II	3.999	3.770	–	3.777	–	–	1.71/3.659	3.792/7.820	[23] JAJSUJ
[{Cu(acac)(bipy)}$_2$($\mu_{1,1}$-N_3)]$_3$(ClO_4)$_3$}·3.75H_2O, *P*-1	I, VI	3.713	–	3.354	–	3.691	3.465	3.156/1.51	5.191/5.275	[46] KEBYUM
[Cu(acac)(bipy)(H_2O)]NO_3}·H_2O, $P2_1/n$	III	–	–	–	3.551	–	–	2.04	4.699	[49] LIVNIO
[Cu(acac)(bipy)]BPh_4, *P*-1	I	–	4.125	–	3.500	–	–	3.538	3.570	[42] NEKCAJ
[Cu(acac)(bipy)(dmso)]BPh_4, *P*-1	I	–	3.682	–	3.995	–	3.726	3.243	4.192	[42] NEKDEO
[Cu(acac)(bipy)(dmf)](dmf) BPh_4, *P*-1	I	3.946	–	–	–	3.791	3.443	3.244	4.796	[42] NEKDIS
[Cu(acac)(bipy)(CH_3OH)] BPh_4, *P*-1	I	–	3.693	–	3.618		3.948	3.260	3.656	[42] NEKDOY
[Cu(acac)(bipy)(py)]BPh_4, *P*-1	I	–	3.487	–	–	4.102	–	3.264	4.588	[42] NEKDUE
[Cu(acac)(bipy)(py)]$_2$[Fe(CN)$_5$(NO)], *P*-1	V	3.798	–	–	–	–	–	3.477	8.860	[54] QAXHEC
[{Cu(acac)(bipy)}$_2$}{Ag(CN)$_2$}](ClO_4)·0.5CH_3CN, *P*-1	I	–	3.966	–	3.809	–	–	3.461	3.961	[43] RELROQ
[{Cu(acac)(bipy)}$_2$}{Au(CN)$_2$}](ClO_4)·0.5CH_3CN, *P*-1	II	3.766	–	–	–	–	–	0.39	7.516	[43] RELSAD
[Cu(acac)(bipy)I], *P*-1	VI	–	–	3.495	–	–	–	3.489	5.475	[55] VIKQUD

*interplanar distance or dihedral angle between about parallel planes.

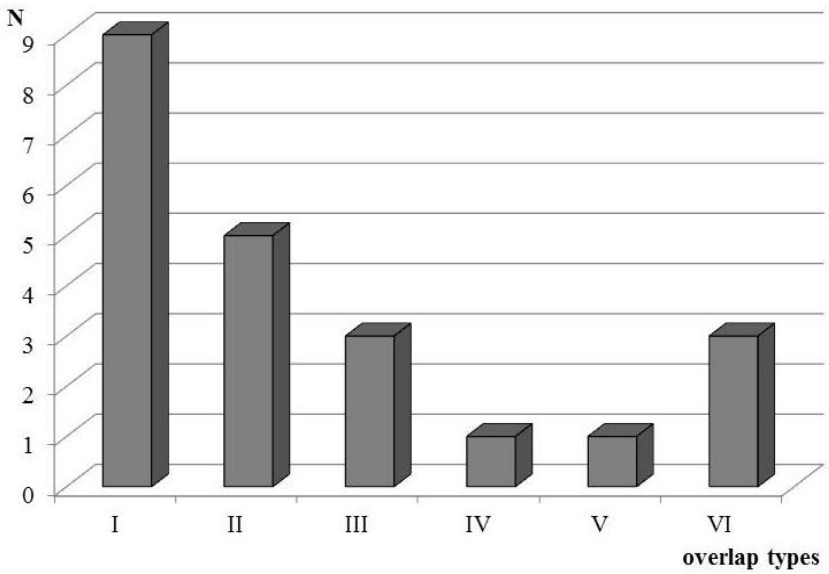

Fig. 7. Histogram of hit distribution over the different types of [Cu(acac)(bipy)] or [Cu(acac)(Me_2bipy)] overlap in the stacking.

The histogram in Fig. 7 and Table 3 show that metallacycles are not involved in stacking interactions (overlap types **II** and **V**) in only 3 from 18 analyzed structures (17%).

6. Conclusions

Analysis of the original results and literature data on square-pyramidal complexes of copper(II) containing a planar or about planar [Cu(acac)(AA)] fragment has revealed that the π–π stacking interaction between these fragments is the dominant intermolecular interaction in the structure of these complexes regardless of their cationic or neutral nature. Most often, metallacycles are involved in this interaction. Typically, an offset or slipped facial arrangement of the π-systems is observed. A head-to-head orientation of stacked fragments and a perfect face-to-face alignment of π-systems are rare. Stacking interactions between [Cu(acac)(AA)] fragments represent a reliable supramolecular synthon suitable to generate a robust supramolecular motif in the crystal structure.

Acknowledgments. Financial support was provided by State Program of R. Moldova 16.00353.50.05A

References

[1] Ch. A. Hunter and J. K. M. Sanders, J. Am. Chem. Soc. 120, 5525, (1990).
[2] B. B. Averkiev, A. A. Korlyukov, M. Y. Antipin, A. B. Sheremetev, and T. V. Timofeeva, Cryst. Growth Des. 14**,** 5418, (2014).
[3] K. Ohno, T. Sugaya, M. Kato, N. Matsumoto, R. Fukano, Y. Ogino, S. Kaizaki, T. Fujihara,

and A. Nagasawa, Cryst. Growth Des. 14, 3675, (2014).
[4] H. Moon, Q. P. Xuan, D. Kim, Y. Kim, J. W. Park, C. H. Lee, H.-J. Kim, A. Kawamata, S. Y. Park, and K. H. Ahn, Cryst. Growth Des. 14, 6613, (2014).
[5] C. An, S. Zhou, and M. Baumgarten, Cryst. Growth Des. 15, 1934, (2015).
[6] (a) D. B. Amabilino and J. F. Stoddart, Chem. Rev. 95, 2725 (1995); (b) C. G. Claessens and J. F. Stoddart, J. Phys. Org. Chem. 10, 254, (1997).
[7] R. W. Jiang, W. C. Ye, K. Y. Woo, J. Du, C. T. Che, P. P. H. But, and T. C. W. Mak, J. Mol. Struct. 642, 77, (2002).
[8] S. J. Carlson, T. Lu, and R.L. Luck, Inorg. Chem. Commun. 6, 455, (2003).
[9] R. P. Sharma, A. Saini, S. Singh, P. Venugopalan, and W. T. A. Harrison, J. Fluorine Chem. 131, 456, (2010).
[10] B. W. Gung and J. C. Amicangelo, J. Org. Chem. 71, 926, (2006).
[11] M. Elstner, P. Hobza, T. Frauenheim, S. Suhai, and E. Kaxiras, J. Chem. Phys. 114, 5149, (2001).
[12] O. Bludsky, M. Rubes, P. Soldan, and P. Nachtigall, J. Chem. Phys. 128, 114102, (2008).
[13] K. F. Konidaris, A. C. Tsipis, G. E. Kostakis, and ChemPlusChem 77, 354, (2012).
[14] (a) L. M. Salonen, M. Ellermann, and F. Diederich, Angew. Chem. Int. Ed. 50, 4808, (2011); (b) L. M. Salonen, M. Ellermann, and F. Diederich, Angew. Chem. 123, 4908, (2011).
[15] M. Rapacioli, F. Spiegelman, D. Talbi, T. Mineva, A. Goursot, T. Heine, and G. Seifert, J. Chem. Phys. 130, 244304, (2009).
[16] (a) J. W. G. Bloom and S. E. Wheeler, Angew. Chem. Int. Ed. 50, 7847 (2011); (b) J. W. G. Bloom and S. E. Wheeler, Angew. Chem. Int. Ed. 123, 7993, (2011).
[17] E. C. Lee, D. Kim, P. Jurecka, P. Tarakeshwar, P. Hobza, and K. S. Kim, J. Phys. Chem., 111, 3446, (2007).
[18] D. B. Ninković, G. V. Janjić, D. Ž. Veljković, D. N. Sredojević, and S. D. Zarić, ChemPhysChem 12, 3511, (2011).
[19] C. Janiak, J. Chem. Soc. Dalton. Trans. 21, 3885, (2000).
[20] Z. D. Tomić, S. B. Novaković, and S. D. Zarić, Eur. J. Inorg. Chem. 11, 2215, (2004).
[21] Z. D. Tomić, S. B. Novaković, and S. D. Zarić, Cryst. Growth Des. 10, 3901, (2010).
[22] T. Sugimori, H. Masuda, N. Ohata, K. Koiwai, A. Odani, and O.Yamauchi, Inorg. Chem. 36, 576, (1997).
[23] A. M. Madalan, V. Ch. Kravtsov, D. Pajic, K. Zadro, Yu. A. Simonov, N. Stanica, L. Ouahab, J. Lipkowski, and M. Andruh, Inorg. Chim. Acta, 357**,** 4151, (2004).
[24] A. M. Madalan, V. Ch. Kravtsov, Yu. A. Simonov, V. Voronkova, L. Korobchenko, N. Avarvari, and M. Andruh, Cryst. Growth Des. 5, 45, (2005).
[25] A. M. Madalan, M. Andruh, N. Avarvari, and M. Fourmigué, Synth. React. Inorg. Met.-Org. Chem. 37, 757, (2007).
[26] H. W. Roesky and M. Andruh, Coord. Chem. Rev., 236, 91, (2003).
[27] D. Bulkley, C. A. Innis, G. Blaha, and T. A. Steitz, Proc. Natl. Acad. Sci. U. S. A., 107, 17158, (2010).
[28] S. Grimme, Angew. Chem. Int. Ed. 47, 3430, (2008).
[29] (a) G. Filippini and A. Gavezotti, Acta Crystallogr., Sect. B, 49, 868 (1993); (b) A. Gavezotti and G. Filippini, J. Am. Chem. Soc. 118, 7153, (1996).
[30] (a) S. Kitagawa and M. Kondo, Bull. Chem. Soc. Jpn. 71, 1739 (1998); (b) G. Guilera and J. W. Steed, Chem. Commun., 1563, (1999); (c) C. Janiak, Angew. Chem., Int. Ed. Engl. 36, 1431, (1997).
[31] K. A. Hirsch, S. R. Wilson, and J. S. Moore, Chem. Eur. J. 3, 765, (1997).

[32] S. E. Wheeler, J. Am. Chem. Soc. 133, 10262, (2011).
[33] G. Janjić, J. Andrić, A. Kaporž, D. Bugarčić, and S. D. Zarić, CrystEngComm 12, 3773, (2010).
[34] B.-H. Ye, M.-L. Tong, and X.-M. Chen, Coord. Chem. Rev. 249, 545, (2005).
[35] G.V. Janjić, P.V. Petrović, D.B. Ninkovic, and S. D. Zarić, J. Mol. Model., 17, 2083 (2011).
[36] E. Melnic, E. B. Coropceanu, O. V. Kulikova, A. V. Siminel, D. Anderson, H. J. Rivera-Jacquez, A. E. Masunov, M. S. Fonari, and V. Ch. Kravtsov, J. Phys. Chem. C 118, 30087 (2014).
[37] E. Melnic, E. B. Coropceanu, A. Forni, E. Cariati, O. V. Kulikova, A. V. Siminel, V. Ch. Kravtsov, and M. S. Fonari, Cryst. Growth Des. 16, 6275, (2016).
[38] P. V. Petrović, G.V. Janjić, and S. D. Zarić, Cryst. Growth Des. 14, 3880, (2014).
[39] S. S. Massoud, R. Tribolet, and H. Sigel, Eur. J. Biochem. 187, 387, (1990).
[40] G. M. Sheldrick,. Acta Crystallogr. A64, 112, (2008).
[41] C. F. Macrae, P. R. Edgington, P. McCabe, E. Pidcock, G. P. Shields, R. Taylor, M. Towler, and J. van de Streek, J. Appl. Crystallogr. 39, 453, (2006).
[42] R. Horikoshi, Y. Funasako, T. Yajima, T. Mochida, Y. Kobayashi, and H. Kageyama, Polyhedron 50, 66, (2013).
[43] A. M. Madalan, N. Avarvari, and M. Andruh, Cryst.Growth Des. 6, 1671, (2006).
[44] N. A. Bailey, D. E. Fenton, M. V. Franklin, and M. Hall, J. Chem. Soc. Dalton Trans. 984, (1980).
[45] A. M. Madalan, C. Ruiz-Perez, E. Melnic, V. Kravtsov, and M. Andruh, Rev. Roum. Chim. 50, 11, (2005).
[46] A. M. Madalan, M. Noltemeyer, M. Neculai, H. W. Roesky, M. Schmidtmann, A. Muller, Y. Journaux, and M. Andruh, Inorg. Chim. Acta 359, 459, (2006).
[47] H. Janani, A. R. Rezvani, F. Rostami-Charati, M. Makha, and B. W. Skelton, Acta Crystallogr., Sect. E: Struct. Rep. Online 66, m1062, (2010).
[48] Y. S. Wong, Ch. H. Ng, and S. W. Ng, Acta Crystallogr., Sect. E: Struct. Rep. Online 65, m934, (2009).
[49] O. O. E. Onawumi, O. O. P. Faboya, O. A. Odunola, T. K. Prasad, and M. V. Rajasekharan, Polyhedron 27, 113, (2008).
[50] A. Paulovicova, U. El-Ayaan, and Y. Fukuda, Inorg. Chim. Acta 321, 56, (2001).
[51] C.-C. Su, S.-P. Wu, C.-Y. Wu, and T.-Y. Chang, Polyhedron 14, 267, (1995).
[52] S. I. Troyanov, A. N. Grigor'ev, and A. A. Drozdov, L. I. Martynenko, Russ. J. Inorg. Chem. 37, 107, (1992).
[53] O. O. E. Onawumi, O. A. Odunola, E. Suresh, and P. Paul, Inorg. Chem. Commun. 14, 1626, (2011).
[54] H.-Z. Kou, E.-Q. Gao, D.-Z. Liao, P. Cheng, Z.-H. Jiang, S.-P. Yan, G.-L. Wang, X.-K. Yao, H.-G. Wang, and J.-P. Tuchagues, Acta Chem. Scand. 53, 542, (1999).
[55] L. Diniz, S. Carvalho, R. H. U. Borges, and B. L. Rodrigues, Acta Crystallogr., Sect. C: Cryst. Struct. Commun. 69, 1010, (2013).

SYNCHRONIZATION AND OPTICAL COMMUNICATIONS BY THE CHAOS MODULATION TECHNIQUE USING QUANTUM DOT LASERS WITH T-TYPE OPTICAL FEEDBACK

N. Ciobanu[1,2], S. S. Rusu[2,3], and V. Z. Tronciu[3]

[1]Department of Human Physiology and Biophysics, State University of Medicine and Pharmacy "NicolaeTestemitanu", Chisinau, Republic of Moldova
[2]Institute of Applied Physics, Academy of Sciences of Moldova, Chisinau, Republic of Moldova
[3]Department of Physics, Technical University of Moldova, Chisinau, Republic of Moldova
E-mail:cnellu@gmail.com

(Received October 25, 2016)

Abstract

We investigate the synchronization and optical communication processes using quantum dots lasers under the influence of external T-type optical feedback. The dynamical behavior of a single mode laser is studied in terms of the Bloch equation model. Appropriate conditions for chaotic behavior and synchronizations are fond. Under these conditions, the chaos modulation technique is applied for encoding and decoding a digital message in a chaos-based communication.

1. Introduction

In recent years, significant attention has been given to the study of nanoscale lasers and devices [1–3]. The main future of these devices is the possibility of obtaining high emission properties for small volume lasers and finally using these devices for integrated optical circuits. A substantial decrease in the cavity size of a nanoscale laser changes the stability properties, where an enhancement of spontaneous emission can be observed. These characteristics play an important role for increasing the communication speed and efficiency of information transmission, where the security is essential.

In particular, for increasing the degree of security of data transmission, a chaos-based communication technique was proposed [4–7]. The chaos modulation techniques require encoding the message in the amplitude of the chaotic output and keeping the amplitude of message small enough in order to avoid message recognition. A possibility of encoding the message in the chaotic output of single mode semiconductor lasers with external feedback was proposed in [8, 9]. The influence of external optical feedback and cavity parameters on the synchronization and message encoding is discussed. Other methods of message encoding within a chaotic carrier were elaborated in electronic circuits [10–12].

To describe the dynamics of a laser system with high spontaneous emission rates, one can use standard methods based on rate equation approach [13–15]. However, for lasers with larger numbers of quantum dots in the active region, the Bloch equation model seems to be more

suitable and realistic [16]. Thus, in this paper, we present a study of the dynamics of a quantum dot laser under the influence of T-type feedback in terms of the Bloch equation model. A possible application of these devices for encoding and decoding digital messages in the chaos based communication technique is discussed. The influence of laser feedback parameters on the dynamics of the system is studied. The paper is organized as follows. A brief description of the setup and of the Bloch equation model is presented in Section 2. The synchronization of a master–slave laser system and encoding/decoding of a digital message using the chaotic modulation technique is discussed in Section 3. Finally, the conclusions are given in Section 4.

2. Model and equations

Figure 1 shows the setup considered for investigations of synchronization and optical communications by using the chaos modulation technique of quantum dots lasers. In our model, the feedback has a T-type structure. ϕ and ψ represent the accumulated optical phases of the laser fields reflected from mirrors R_1 and R_2, respectively. τ_1 and τ_2 are the delay time introduced by the first and second branches, respectively.

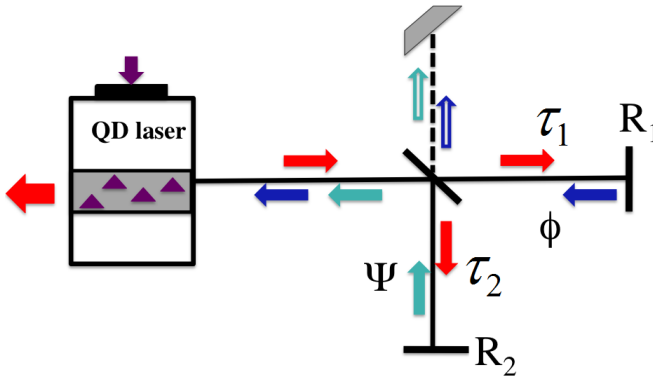

Fig. 1. Setup of a quantum dot laser under the influence of double T-type feedback.

The dynamics of the system is described by the Bloch equation model [16] where photon decay rate and polarization decay are taken into account. The system of equation containing equations for complex field amplitude E, polarization P, and inversion D for master "m" and slave "s" is given by

$$\frac{dE_{m,s}}{dt} = -\kappa E_{m,s} + 2Z^{QD}\Gamma g P_{m,s} + \frac{Z^{QD}\Gamma\beta}{\tau_{eff}E^{*}_{m,s}}\left(\frac{D_{m,s}+1}{2}\right)^2 + \Gamma_1 E_{m,s}(t-\tau_1)e^{i\phi} + \Gamma_2 E_{m,s}(t-\tau_2)e^{i\Psi} + kE_s, \tag{1}$$

$$\frac{dP_{m,s}}{dt} = -\gamma P_{m,s} + gD_{m,s}E_{m,s}, \tag{2}$$

$$\frac{dD_{m,s}}{dt} = -4gE_{m,s}P_{m,s} + \frac{d_0 - D_{m,s}}{T_1} + \frac{1}{\tau_{eff}}\left(\frac{D_{m,s}+1}{2}\right)^2. \quad (3)$$

The photon decay rate is designated as *K*, while the polarization decay parameter corresponds to γ. τ_{eff} is the effective rate of spontaneous emission and given by Purcell factor F_P and the spontaneous emission rate τ_{sp}, i.e., $\tau_{eff} = F_P/\tau_{sp}$. g and β represent the coupling and spontaneous emission factors. The β factor describes the percentage of spontaneously emitted photons, which are emitted inside a resonant cavity wave mode. The number of quantum dots in the active region of the laser is designated as Z^{QD}. Confinement factor Γ represents the fraction of quantum dots within the mode volume that contribute to laser emission. It is a measure of the fraction of the active region that amplifies a given mode; for a single-mode laser regime, Γ is a constant parameter. Finally, inversion lifetime T_1 and pump strength d_0 depend on the carrier density.

The terms that contain Γ_1 and Γ_2 parameters of equation (1) characterize the optical feedback that comes from T-type branches where Γ_1 and Γ_2 are the feedback strengths in respective branches. For the following numerical calculations the following dimensionless parameter values are used: $F_P = 1$, $\Gamma = 0.01$, $\beta = 1$, $Z^{QD} = 1000$, $d_0 = 0.95$, $K = 300$, $\tau_{sp} = 0.001$, $T_1 = 0.01$, $g = 48.9$, and $\gamma = 100$. Other parameter values, i.e., $\tau_1 = 0.2$ ns and $\tau_2 = 0.5$ ns, correspond to the round-trip times in the external branches. These parameters are considered identical for both master and slave lasers in the chaos modulation technique and used for the calculated results shown in all figures of the paper.

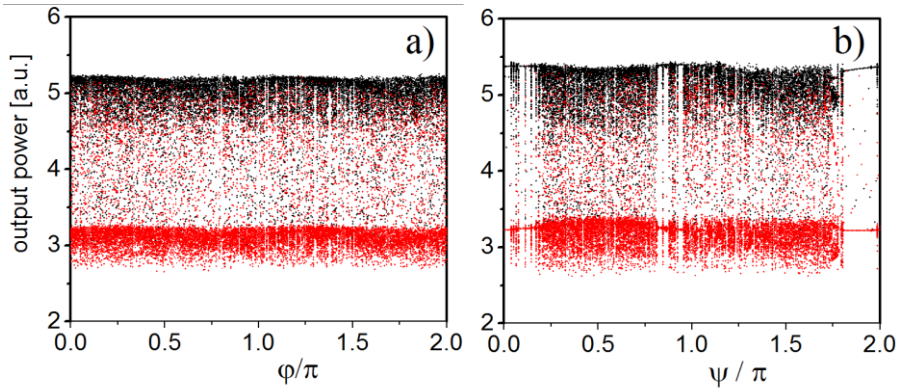

Fig. 2. Bifurcation diagrams for (a) $\Gamma_1 = 7$ ns^{-1}, $\Gamma_2 = 15$ ns^{-1}, $\psi = 0.5\pi$ and (b) $\Gamma_1 = 10$ ns^{-1}, $\Gamma_2 = 20$ ns^{-1}, $\phi = 0.5\pi$. Black (red) points show the maximum (minimum) of the output power.

First we consider the numerical bifurcation diagrams shown in Fig. 2, where the feedback phases of first ϕ and second external cavity branches ψ are the bifurcation parameters. One can observe in Fig. 2a that, at $\Gamma_1 = 7$ ns^{-1}, $\Gamma_2 = 15$ ns^{-1}, and $\psi = 0.5\pi$ and in the case of ϕ being bifurcation parameter, the system exhibits a chaotic behavior for all values of phase ϕ. When the

feedback parameters are increased to $\Gamma_1 = 10\ \text{ns}^{-1}$, $\Gamma_2 = 20\ \text{ns}^{-1}$, and $\phi = 0.5\pi$ as shown in Fig. 2b, a small region of continuous wave regime appears. On the other hand, in comparison with a single feedback (so-called conventional optical feedback) the presence of double sections results in more complex oscillations within wide regions of phases. In what follows, we are interested in the master–slave laser configuration and in the evolution of synchronization properties of this system. It is well known that the synchronization mechanism between two systems (master and slave) can be analyzed by measuring cross-correlation coefficient $C = \langle P_{\text{master}} P_{\text{slave}} \rangle \left(\left| \langle P_{\text{master}} \rangle \langle P_{\text{slave}} \rangle \right| \right)^{-1}$. The synchronization of two unidirectionally coupled master and slave lasers was studied numerically. The operation conditions are chosen such that the chaotic behavior persists for any values of external phases ϕ and ψ. Figure 3 shows the time evolution of emitted power for master (P_{master}) and slave (P_{slave}) lasers when the synchronization process is implemented.

One can observe a chaotic behavior where both time traces remain almost similar. The process of synchronization is the first indication that the chaos based communication can be applied for this system.

Below, we plot synchronization diagrams for different values of coupling coefficient. The emitted power of the master laser versus the slave for various values of the coupling parameter k is shown in Fig. 4. If the coupling parameter is equal to zero, as shown in Fig. 4a, the trajectories of the master and slave lasers depart from each other and the synchronization map represents a cloud of points showing the lack of correlation between outputs. Increasing the coupling parameter to $k = 20\ \text{ns}^{-1}$, a good synchronization process can be observed (see Fig. 4d). Thus, we have shown that two quantum dot lasers in the chaotic regime can be synchronized.

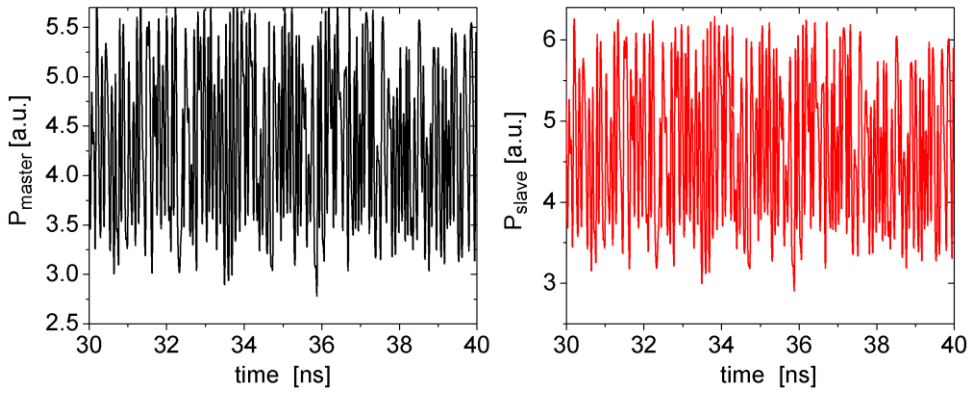

Fig. 3. Synchronization process of master (left) and slave (right) lasers for $k = 20\ \text{ns}^{-1}$.
Otherparameters: $\phi = 1.6$, $\psi = 0.8$, $\Gamma_1 = 20\ \text{ns}^{-1}$, $\Gamma_2 = 30\ \text{ns}^{-1}$.

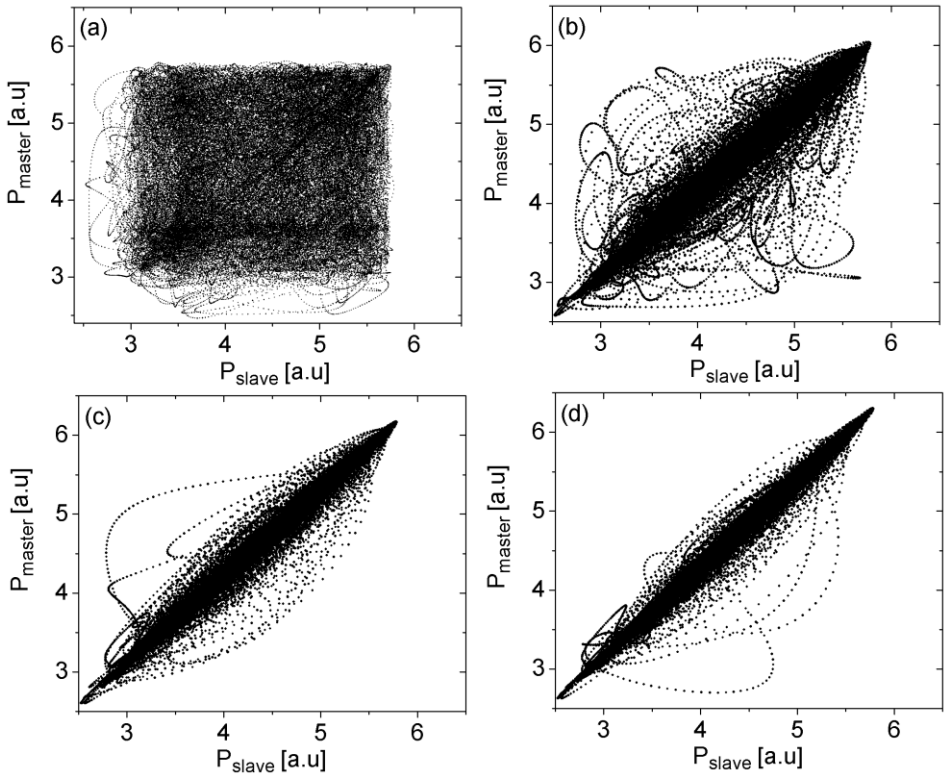

Fig. 4. Synchronization diagrams for different values of coupling parameter: (a) $k = 0$ ns^{-1}, (b) $k = 10$ ns^{-1}, (c) $k = 15$ ns^{-1}, and (d) $k = 20$ ns^{-1}.

Next, we discuss a model for transmission of an encoded message in the chaotic profile in the setup of two identical quantum dot lasers as shown in Fig. 5. The message is encoded in the chaotic amplitude of the master laser field and transmitted to the receiver, i.e., the slave laser. At the receiver, the message can be decoded depending on the degree of synchronization between the sender and the receiver.

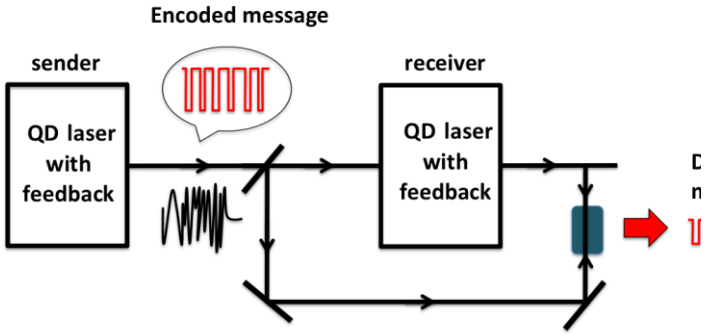

Fig. 5. Setup for chaos synchronization and message encoding and decoding using master–slave quantum dot lasers with feedback.

The chaotic output of a sender (master laser) can be used as a carrier in which a digital message is encoded. Normally, the amplitude of the encode message is much smaller than the wave front of the chaotic carrier; therefore, it is very complicated to extract the message from the chaotic carrier. The decoding operation is based on the fact that coupled chaotic master–slave lasers can be synchronized if appropriate conditions are given. To decode the message, the transmitted signal should be coupled to the receiver in another chaotic system, i.e., a slave laser that is identical to the sender.

The scenario and appropriate conditions for message encoding by the chaos modulation technique using compact lasers under the influence double-feedback configuration are represented in Fig. 6. The digital message before encoding is represented in the top panel (Fig. 6a). Panel (b) shows the output power of the master laser and (c) is the message encapsulated in the chaotic profile of the master laser that is transmitted to the receiver (slave laser). Finally, the recovered message after filtering is plotted in the bottom panel. The dotted curve corresponds to the encoded message, while the solid line corresponds to the recovered message. Thus, the received message corresponds to the encoded one.

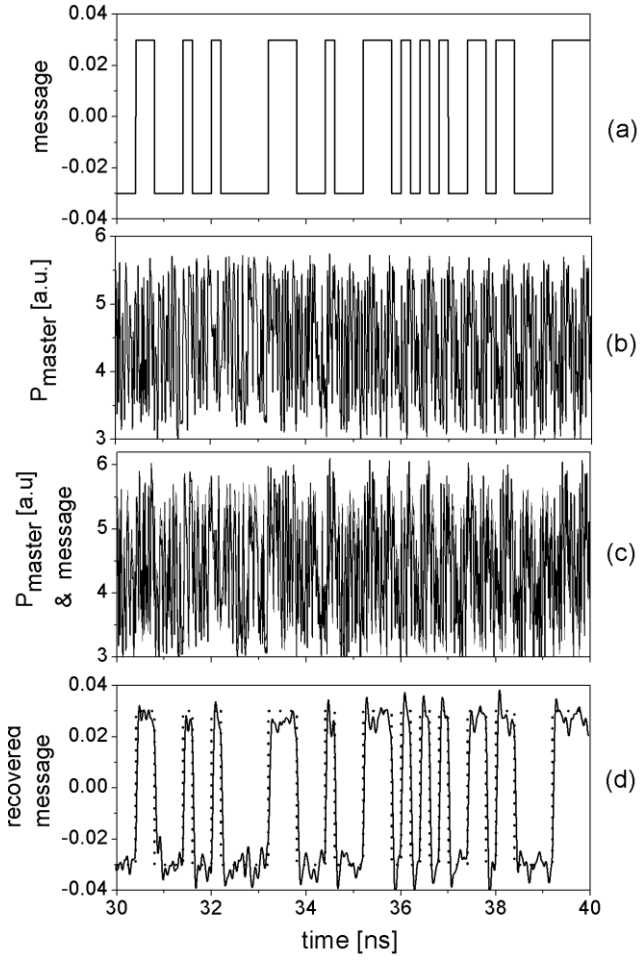

Fig. 6. Encoding and decoding of a digital message using the chaotic modulation technique for a master–slave laser system: (a) encoded message profile; (b) output power of the laser without message; (c) transmitted message encapsulated in the laser message; and (d) decoded and recovered message after filtering (solid line) and input message (dotted line). All parameters are the same as in Fig. 3.

3. Conclusions

In this paper, we have studied the dynamics of a quantum dot laser system under the influence of double-feedback of cavities. This study has been conducted in terms of the Bloch equation model. The synchronization of lasers and the bifurcation diagram are appropriate for different parameters of the external feedback. We have found the condition for which master–slave lasers exhibit chaotic behaviors appropriate to chaos based communications. A technique of transmission of anencoded message in this chaotic regime has been discussed. We believe that our work provides a good basis for future studies of various techniques for chaos based communications using compact quantum dot lasers with feedback from external cavities.

Acknowledgments. This work was supported by project STCU - 5993 and 14.02.116F. VZT acknowledges the support from the Alexander von Humboldt Foundation and from CIM–Returning Experts Programme.

References

[1] N. Gregersen, T. Suhr, M. Lorke, and J. Mork, Appl. Phys. Lett. 100, 131107, (2012).
[2] M. Lorke, T.Suhr, N. Gregersen, and J. Mork, Phys. Rev. B 87, 205310, (2013).
[3] N. Majer, K. Ludge, and E. Scholl, Phys. Rev. B 82, 235301, (2010).
[4] S. Donati and C. R. Mirasso, Eds., IEEE J. Quantum Electron.38 (9), 1138, (2002).
[5] S. Sivaprakasam and K. A. Shore, Opt. Lett.24 (7), 466, (1999).
[6] A. Bogris, D. F. Kanakidis, A. Argyris, and D. Syvridis, IEEE J. Quantum Electron.40 (9), 1326, (2004).
[7] F.Y. Lin and M.C. Tsai, Opt. Express, 15 (2), 302, (2007).
[8] C.R. Mirasso, P. Colet, and P. Garcia-Fernandez, IEEE Photon. Technol. Lett., 8 (2) 299, (1996).
[9] V.Z. Tronciu, C. Mirasso, P. Colet, M. Hamacher, M. Benedetti, V. Vercesi, and V. Annovazzi-Lodi, IEEE J. Quantum Electron.46 (12), 1840, (2010).
[10] K.M. Cuomo and A.V. Oppenheim, Phys. Rev. Lett. 71, 6548, (1993).
[11] K.M. Cuomo, A.V. Oppenheim, and S. H. Strogatz, IEEE Trans. Circuits Syst.40, 626633, (1993).
[12] I. Fischer, Y. Liu, and P. Davis, Phys. Rev. A 62, 011801(R), (2000).
[13] B. Globisch, C. Otto, E. Scholl, and K. Ludge, Phys. Rev. E 86, 046201, (2012).
[14] W.W. Chow and S.W. Koch, IEEE J. Quantum Electron. 41, 495, (2005).
[15] V.Z. Tronciu, Y. Ermakov, P. Colet, and C.R. Mirasso, Opt. Comm., 281, 4747, (2008).
[16] R. Aust, T. Kaul, Cun-ZhengNing, B. Lingnau, and K. Ludge, Opt. Quantum Electron. 48, 109, (2016).

DYNAMICS OF A SEMICONDUCTOR LASER UNDER THE INFLUENCE OF MULTI-SECTION FEEDBACK: APPLICATIONS TO CHAOS-BASED COMMUNICATIONS

S. S. Rusu[1,2] and V. Z. Tronciu[2]

[1] Institute of Applied Physics, Academy of Sciences of Moldova, Chisinau, Moldova
[2]Department of Physics, Technical University of Moldova, Chisinau, Republic of Moldova
E-mail: tronciu@mail.utm.md

(Received October 20, 2016)

Abstract

This paper reports the numerical results of the dynamical behavior of a novel integrated semiconductor laser subject to multiple optical feedback loops. Due to the influence of the feedback, under appropriate conditions, the system exhibits a strong chaotic behavior suitable for chaos-based communications. We demonstrate the effect of the relevant device parameters on the laser dynamics and show that the properties of the external cavity and its position in the device have a considerable influence on the chaotic behavior of the laser. The synchronization of two unidirectionally coupled lasers is studied numerically. Finally, we find appropriate conditions for message encoding by a chaos modulation technique using compact lasers under the influence of multiple-feedback loops.

1. Introduction

In the last decade, the phenomena of destabilization and chaos of laser emission by external cavities have been the subject of considerable attention, with the studies mainly motivated by the prospect of the applications to chaos-based communication (CBC) systems. Semiconductor lasers subjected to the influence of optical feedback from a distant mirror have been extensively investigated for the past two decades and different dynamical behaviors have been characterized, including periodic and quasi-periodic pulsations, low-frequency fluctuations, coherent collapse, optical turbulence, and chaos (for more details, see [1]). It is well known that the chaotic waveform is suitable for CBC. Thus, the chaotic communications have become an option to improve privacy and security in date transmission, especially after the recent field demonstration of the metropolitan fiber networks of Athens [2]. In optical CBCs, the chaotic waveform is generated by using semiconductor lasers with either all-optical or electro-optical feedback loops [3–10]. Configurations using Fabry–Perot resonators providing the optical feedback, the so-called frequency selective feedback, have also been considered [11–13]. Several message encoding schemes have been proposed in the literature [14, 15]. Here, we include the message as a modulation in the amplitude of the chaotic carrier (chaos modulation) [3, 11, 12]. The message can be decoded at the receiver by comparing its input with message with its output. The main aim of recent technological progress has been the production of structures with stable properties and the possibility of their application in different areas. The distributed feedback

(DFB) lasers with external feedback from multi sections might be a key element for devices used in the CBC system. Note that the communication method based on chaos would bring great benefits to secure data transmitted in communication networks.

In this paper, we consider an integrated compact device composed of a semiconductor laser subject to the feedback from multiple cavities with the aim of generating a complex chaotic waveform suitable for applications in CBCs. The obtained results show that, under appropriate conditions, DFB lasers with multiple external feedbacks exhibit a chaotic behavior appropriate for CBCs. An advantage of the proposed system compared with that of conventional optical feedback is that the chaotic behavior occurs for short lengths of cavities, which makes more compact device. The paper is structured as follows. We start in Section 2 by describing the laser setup and we introduce an appropriate model to describe the system dynamics. Section 3 presents a study of the dynamics of a laser under the influence of multi cavity feedback. The suitable conditions for the chaotic evolution of the output power system due to the influence of feedback are determined. The synchronization properties of two such devices and the chaos modulation encryption method are also demonstrated. Finally, conclusions are given in Section 4.

2. Laser model and equations

Figure 1a shows the structure of the DFB laser under the influence of feedback from equally distributed external cavities. We consider a single-mode continuous-wave (CW) laser coupled to longitudinal multi-cavities. The first mirror is located at distance L from the laser facet, and the distance between mirrors is taken also L. We consider five external mirrors. At the same time, Fig. 1b shows a sketch of possible experimental implementations of the setup from Fig. 1a with a CW laser with two air gaps, similar to that of [11]. The DFB section is coupled to two phase sections, two optically transparent straight waveguides, and two air gaps. The phase sections were introduced to control the feedback phases of the external cavities by adjusting the small bias current of them. For more details on the fabrication technique, see [11]. Thus, our present investigation has two aims. First, we want to sort out how the dynamics of the laser, especially the chaotic properties of the device, can be tailored by appropriately designing the external cavities similar to that in Fig. 1a. Second, we want to apply chaos modulation technique to a suited experimental structure as in Fig. 1b.

The system dynamics is analyzed in terms of the extended Lang–Kobayashi model [16] for the complex amplitude of electric field E and density of carriers; we consider the approximation of a single loop and neglect the multi-reflections within the cavities:

$$\frac{dE}{d\tau}=\frac{1}{2}(1+i\alpha)\left[\frac{g(N-N_0)}{1+\varepsilon|E|^2}-\frac{1}{\tau_p}\right]E+\sum_{n=1}^{5}\gamma_n\exp\left(-i\sum_{k=1}^{n}\varphi_k\right)E(\tau-n\tau_L)\,, \tag{1}$$

$$\frac{dN}{dt}=\frac{I}{e}-\frac{1}{\tau_e}N-\frac{g\left(N-N_0\right)}{1+\varepsilon|E|^2}|E|^2\,, \tag{2}$$

where γ_n (n = 1–5) are the feedback strengths governed by the reflectivity's R_n. Other parameters are as follows: Henry factor of α = 5, differential gain coefficient of $g = 1.5\cdot10^{-5}$ ps^{-1}, and saturation of the gain coefficient of $\varepsilon = 5\cdot10^{-7}$. The lifetime of photons and carriers are $\tau_p = 3\cdot10^{-3}$ ps and τ_e = 2 ns, respectively. These parameter values are used for the calculated results that are shown in all figures of the paper.

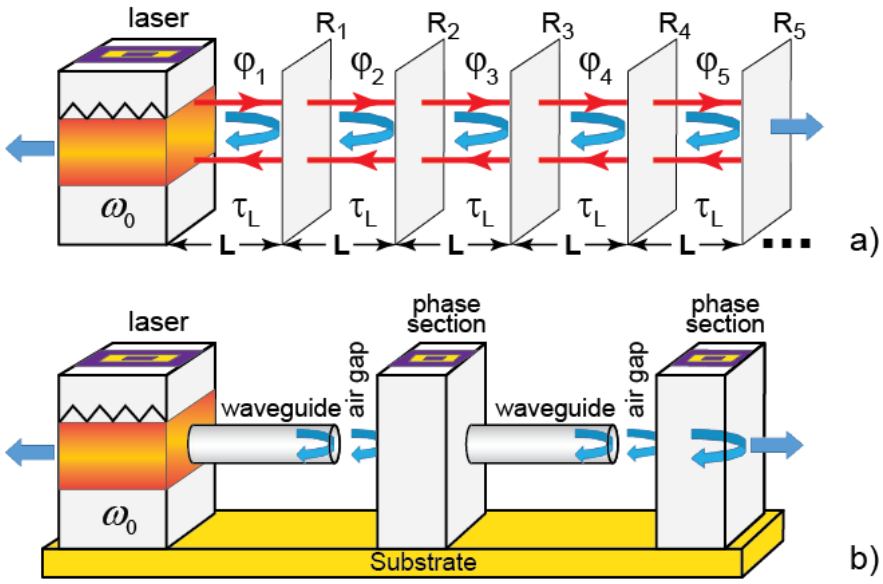

Fig. 1. (a) Sketch of a setup for chaos synchronization and message encoding using semiconductor lasers under the influence of multiple cavity feedback and (b) view of practical implementation of the proposed integrated device with double air gaps. The length of the air gap sections is 5 μm, similar to that of a single air gap device used in [11]. The reflection between air gaps and both waveguide and phase sections is ~30%. The setup is not in scale.

3. Results and discussion

We begin by considering a more general case of optical feedback originated from multi section cavities shown in Fig. 1a. We examined the dynamics of a semiconductor laser with optical feedback from multi section cavities using equations (1)–(2). It is well known that, for small feedback strength, a laser shows either CW or pulsating operations non-applicable in CBC systems. Chaotic behavior appears as the feedback strength is increased enough. Thus, an increase in feedback strength leads to the appearance of chaotic behavior in the system. Figure 2 shows numerical calculations of the time evolution of output power and phase portrait and the power spectrum of the semiconductor laser under the influence of optical feedback from multi cavity in the chaotic regime appropriate for chaos based communications for different feedback strength. Thus, feedback strength γ ($\gamma = \gamma_1 = \gamma_2 = \gamma_3 = \gamma_4 = \gamma_5$) and phase φ ($\varphi = \varphi_1 = \varphi_2 = \varphi_3 = \varphi_4 = \varphi_5$) are considered as main bifurcation parameters. The feedback strengths are governed by the cavity reflectivity's. It is shown in Fig. 2a that, for $\gamma = 10$ ns^{-1} the output power describes a quasi-chaotic behavior and the phase portrait is a distorted limit cycle. In the power spectrum, a few harmonics are dominant. For $\gamma = 15$ ns^{-1} the time evolution of output power and the phase portrait become more complicated and new harmonics appear in the power spectra as shown in Fig. 2b. Thus, an increase in the level of optical feedback strength triggers certain trajectories to chaos. One can see in Fig. 2c that the oscillations of the output

power become more complicated and chaotic behavior appears and the phase portrait is a strange attractor. Thus, due to the influence of multiple feedbacks, the laser behavior has been found to be chaotic for a large range of parameters and laser bias currents.

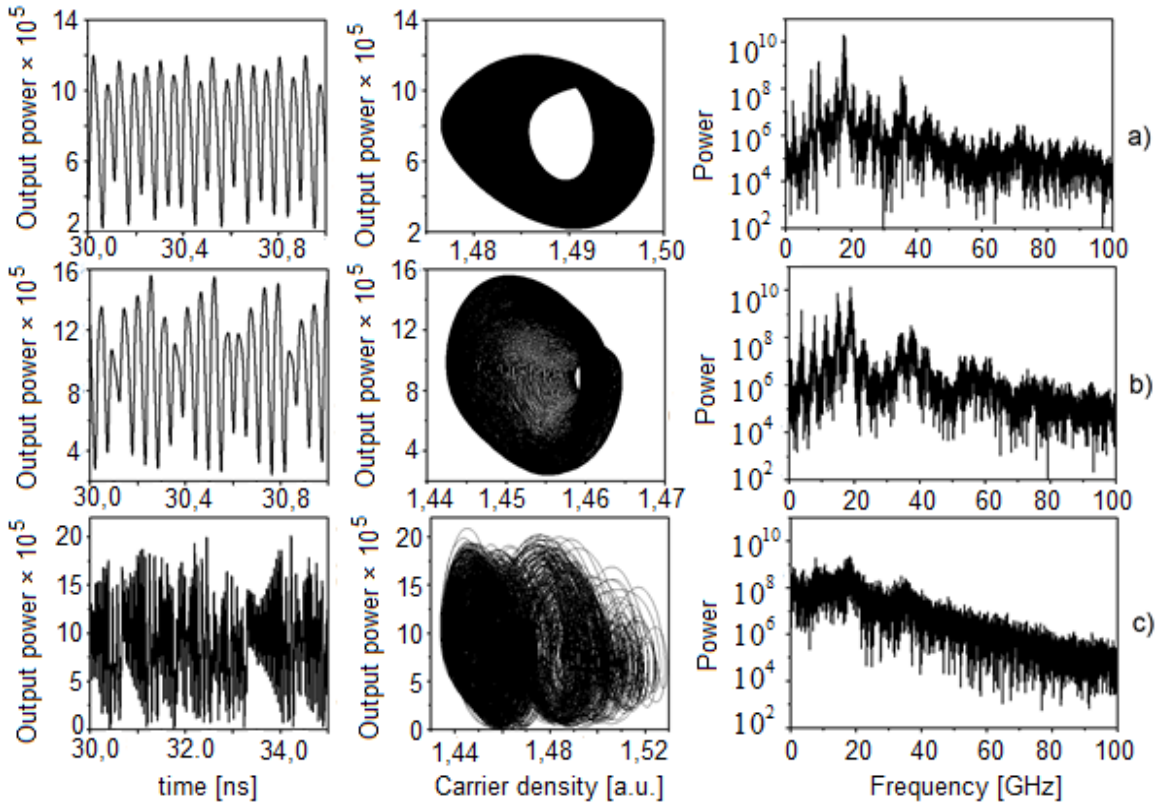

Fig. 2. Pulse trace of output power (left), phase portrait (center), and power spectrum (right) of a semiconductor laser under the influence of optical feedback from multi cavity for the chaotic behavior: (a) $\gamma = 10$ ns^{-1} – quasi-chaos, $\gamma = 15$ ns^{-1} – chaos, and $\gamma = 20$ ns^{-1} – strong-chaos.

Next, we examine the laser dynamics in terms of bifurcation diagrams. A typical calculation of bifurcation is shown in Fig 3a, where the feedback strength is the bifurcation parameter. One can see an evident strong chaotic behavior for $\gamma > 14$. If we increase the injected current, the CW operation is observed (see Fig. 3). Then the laser begins to produce pulsations (*P*) through a Hopf bifurcation (*H*) marked by a circle in Fig. 3a. One can observe the appearance of a low-amplitude chaotic behavior for low feedback strengths followed by the CW operation and a scenario compatible with the quasi-periodic route to chaos. As the feedback strength further increases, a second scenario compatible with the quasi-periodic route to chaos appears. For large values of the feedback strength, the system displays a chaotic behavior. If φ is considered as a bifurcation parameter, the chaotic behavior is present for all values of phase φ (see Fig. 3). Thus,

the proposed setup can generate the fully chaotic pulse traces suitable for chaos based communications.

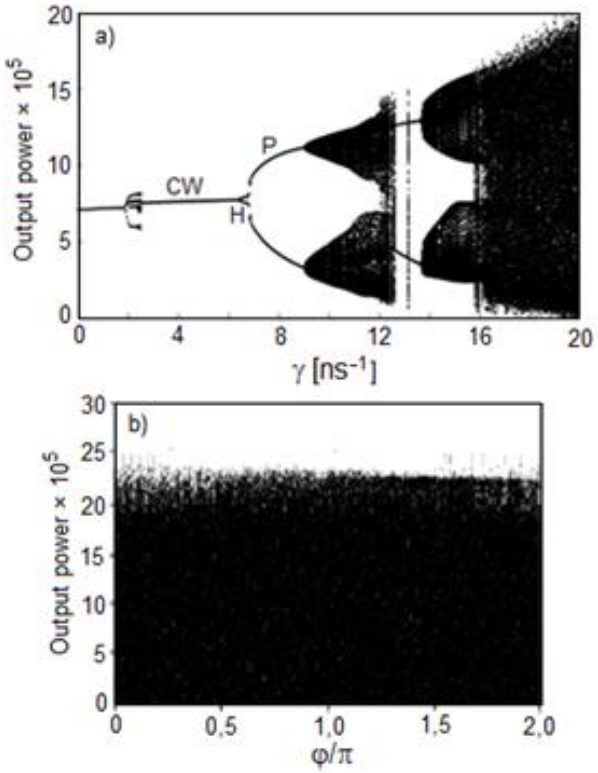

Fig. 3. Bifurcation diagram for (a) γ being a bifurcation parameter and phase $\varphi = \pi/2$ and (b) φ bifurcation parameter and $\gamma = 20$ ns^{-1}.

It is well known that the autocorrelation time is related to the complexity of the generated chaos. Figure 4 shows the calculated autocorrelation time [17] of a semiconductor laser under the influence of optical feedback from multi cavity in two parameters plane phase. The white region corresponds to CW or periodic regimes. The red region shows the strong chaos regime with autocorrelation time $\tau_c < 100$ ps. It can be clearly seen how the autocorrelation time changes and, in particular, how the autocorrelation time becomes much shorter for specific feedback strength and phases providing more secure conditions for chaos-based communications. Thus, as the feedback strength increases, the autocorrelation time decreases, being an indication that the laser dynamics becomes more chaotic.

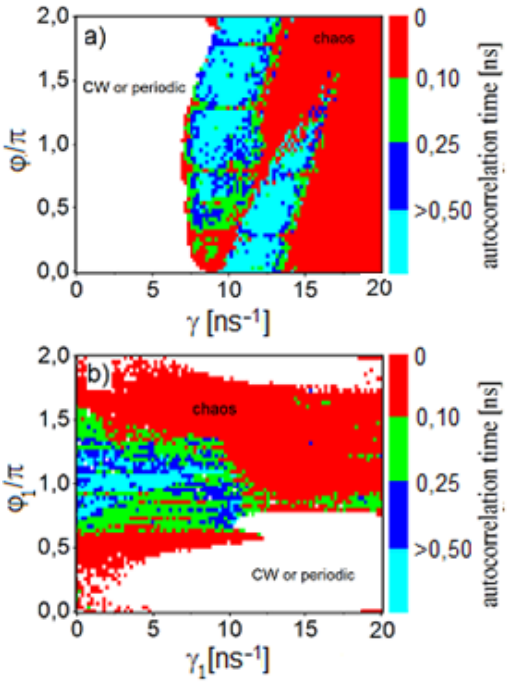

Fig. 4. Autocorrelation time in the plane of different parameters: (a) plane ($\varphi - \gamma$) and (b) plane ($\varphi_1 - \gamma_1$) for $\varphi_2 = \pi/2$, $\varphi_3 = \pi/4$, $\varphi_4 = \pi$, $\varphi_5 = 3\pi/2$, and $\gamma_2 = 5$, $\gamma_3 = 10$, $\gamma_4 = 15$, $\gamma_5 = 20$.

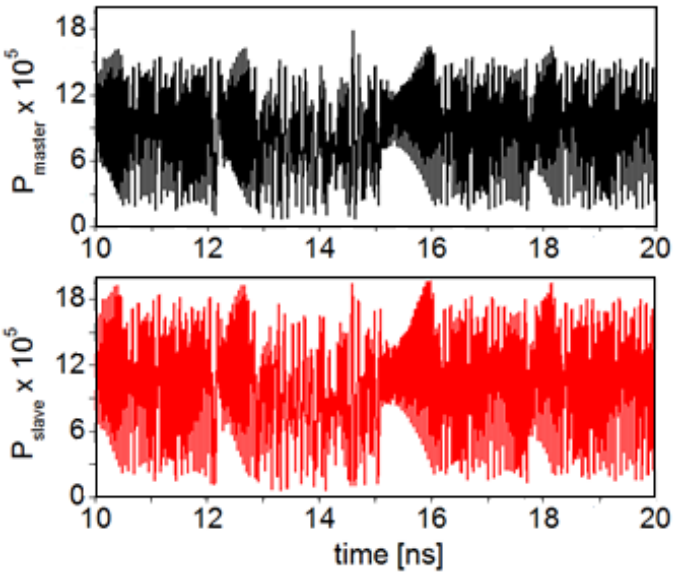

Fig. 5. Synchronization process of two lasers for $k = 90$. Pulse traces of master (top) and slave (bottom) lasers showing a chaotic behavior. Other parameters: $\gamma = 15$ ns^{-1}, $\varphi = 3\pi/4$.

So far, we have discussed different aspects of the transmitter laser dynamics under the influence of multiple feedbacks. In what follows, we focus on the transmitter–receiver configuration, evaluate the synchronization properties, and make use of these integrated devices for message encoding and decoding in CBCs. In the chaos modulation technique, the message is encoded as a small amplitude modulation of the emitted field of the master [11]. At the receiver system, the message is decoded by making the difference between the input of the receiver with its output, which is ideally synchronized to the carrier. Thus, in what follows, we numerically analyze the synchronization properties of two lasers connected in unidirectional direction. It is well known that the synchronization can be quantified by measuring the cross-correlation coefficient. Figure 5 shows the chaotic behavior of master (top) and slave (bottom) lasers in the process of synchronization under the influence of optical feedback from multi cavity. It can be clearly seen that the two time traces remain similar to each other.

Figure 6 shows the emitted power of the slave laser versus the power of the master (synchronization diagram) for feedback strength $\gamma = 15$ ns^{-1} and different levels of coupling parameter k. If the coupling parameter is equal to zero, as shown in Fig. 6a, the trajectories of the master and slave lasers depart from each other and the synchronization map is a cloud of points showing the lack of correlation between outputs. With an increase in the coupling parameter to $k = 50$ ns^{-1}, the synchronization map shows a week synchronization process (see Fig. 6b). By increasing the coupling to $k = 75$ ns^{-1}, the synchronization improves. With a further increase in coupling to 90 ns^{-1}, the synchronization becomes clear and cross correlation coefficient approaches unity (see Fig. 6d).

Figure 7 shows the map of synchronization quality in the plane of different parameters for coupling coefficient fixed to $k = 90$ ns^{-1}. Figure 7a displays the value of the correlation function in the parameter space ($\varphi - \gamma$). High degree of synchronization is characterized by green color. It can be clearly seen that the region of high correlation coefficients is wide. This conclusion is confirmed also by Fig. 7b, where the region with a low cross correlation coefficient is very narrow and present only for certain phases. However, note that the higher cross correlation region includes also the CW and self-pulsation regimes. Thus, in order to choose an appropriate initial point for message encoding in the chaos modulation technique, we have to select a certain point operating in the chaotic regime from Fig. 5.

Further on, we study the transmission–reception configuration of two lasers shown in Fig. 1b connected in unidirectional configuration [11]. We examine the encrypting and decrypting of a digital message in the chaos modulation technique. Figure 8 illustrates the process of transmission of a 10 Gb/s digital signal. Panel (a) shows the shape of the incident signal, i.e., the one that should be sent. Panels (b) and (c) show the output power of the master laser without a message and with it, respectively. Panel (d) shows the decoded message, as indicated in [11], and filtered by an appropriate low-pass filter [18]. This figure shows that, for the case where the parameters of both lasers coincide, the message is fully recovered. Thus, we have theoretically shown that the chaotic modulation method can be implemented in a setup of lasers under the influence of multiple optical feedbacks.

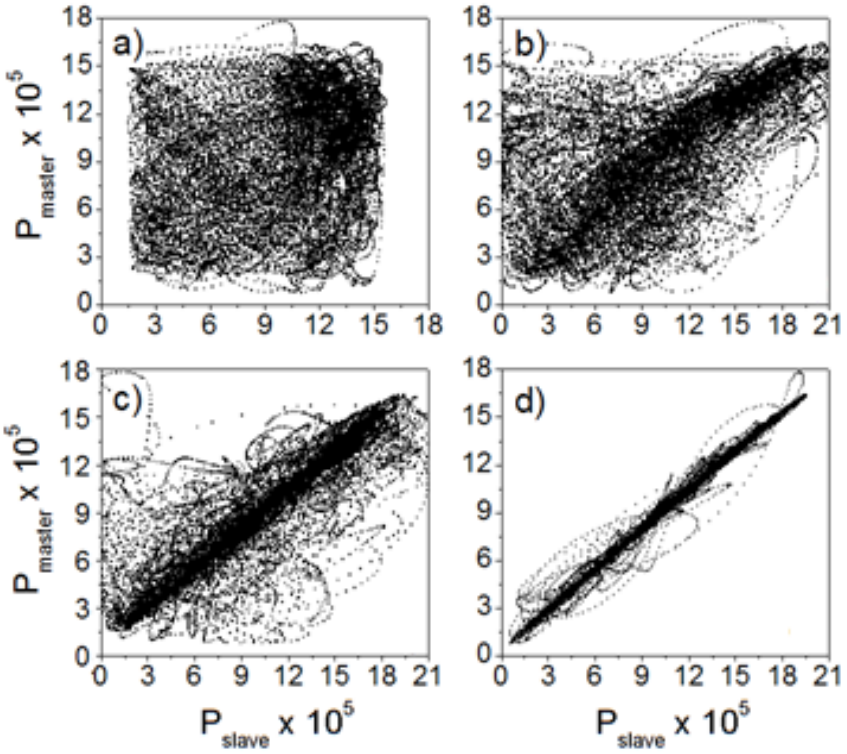

Fig. 6. Synchronization diagrams for different levels of the coupling parameter: (a) $k = 0$ ns^{-1}, (b) $k = 50$ ns^{-1}, (c) $k = 75$ ns^{-1}, and (d) $k = 90$ ns^{-1}. Other parameters: $\varphi = 3\pi/4$, $\gamma = 15$ ns^{-1}.

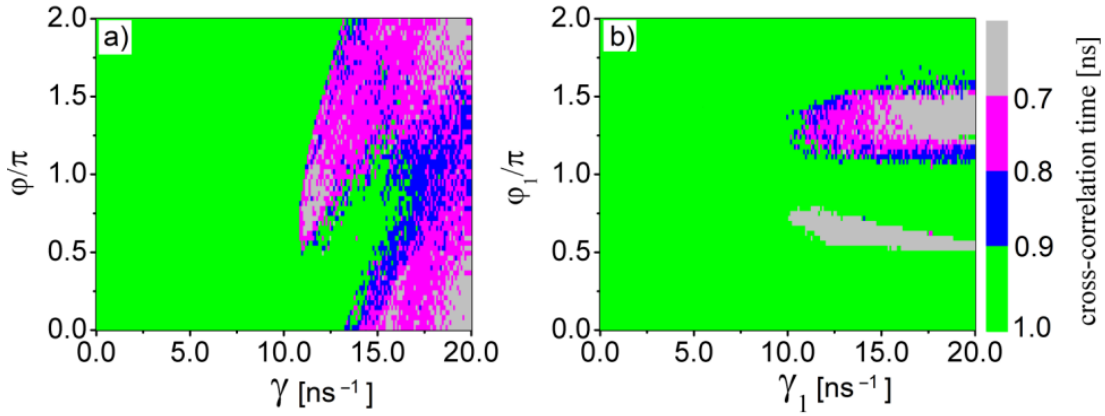

Fig. 7. Cross-correlation time in the plane: a) $(\varphi - \gamma)$, b) $(\varphi_1 - \gamma_1)$ for $\varphi_2 = \pi/2$, $\varphi_3 = \pi/4$, $\varphi_4 = \pi$, $\varphi_5 = 3\pi/2$, and $\gamma_2 = 5$ ns^{-1}, $\gamma_3 =$ ns^{-1}, $\gamma_4 = 15$ ns^{-1}, $\gamma_5 = 20$ ns^{-1}.

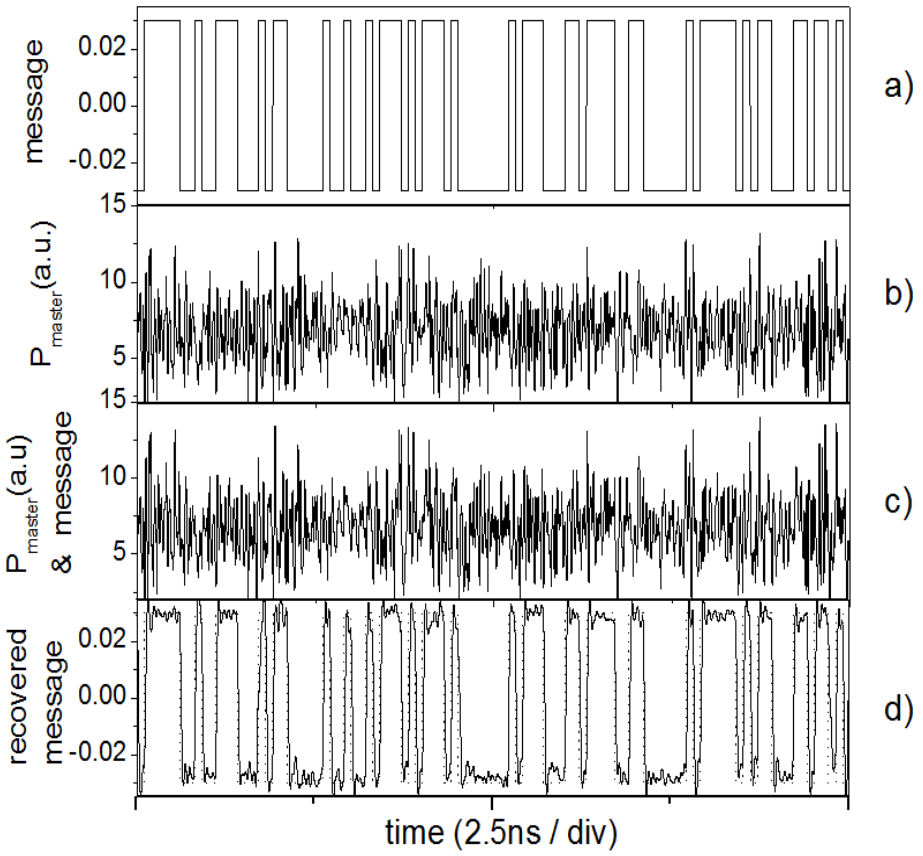

Fig. 8. Numerical results of encoding and decoding of a 10 Gbit/s digital message using chaos modulation technique in the master and slave lasers configurations shown in Figure 1b). a) Encoded message. b) Output of the master laser without message. c) Transmitted signal (with message) d) Decoded message and recovered message after filtering (solid line) and input message (dotted line). Other parameters: length of waveguide – 5 mm, length of airgap 5 μm, length of phase section 200 μm, $\varphi = \pi/2$, $k = 50$ ns^{-1}.

4. Conclusions

In terms of the Lang–Kobayashi equations, the dynamics of a single mode semiconductor laser with optical feedback that comes from multi cavities has been investigated. A novel setup for the realization of multiple feedbacks has been proposed. The presence of several external cavities results in a more complex system oscillations keeping the device compact. Thus, an advantage of the proposed system compared with that of conventional optical feedback is that a chaotic behavior appropriate for CBC occurs for short lengths of cavities. We have shown that two of these devices with identical parameters can be synchronized when operating in a chaotic regime in a master–slave configuration. It has been shown that, for the parameter values where synchronization with higher cross correlation is achieved, it is possible to encode a higher bit rate message in the carrier using the chaos modulation technique. Finally, the message can be

appropriately recovered. We believe that our work provides a good basis for future studies and, in particular, provides some pointers for more detailed investigations of compact lasers with feedback from external multi-section cavities and their applications for CBC.

Acknowledgments. The authors acknowledge the support of projects STCU -5993, 14.02.116F and the technical support from A. Sanduta. VZT acknowledges the support from the Alexander von Humboldt Foundation and from CIM–Returning Experts Programme.

References

[1] B. Krauskopf, and D. Lenstra, (Eds.): Fundamental Issues of Nonlinear Laser Dynamics. AIP Conf. Proc. 548, (2000).
[2] A. Argyris, D. Syvridis, L. Larger, V. Annovazzi-Lodi, P. Colet, I. Fischer, J. García-Ojalvo, C. R. Mirasso, L. Pesquera, and A. L. Shore, Nature 438, 343, (2005).
[3] C. R. Mirasso, P. Colet, and P. Garcia-Fernandez, IEEE Photon. Technol. Lett. 8, 299, (1996).
[4] V. Annovazzi-Lodi, S. Donati, and A. Scire, IEEE J. Quantum Electron. 32, 953, (1996).
[5] S. Sivaprakasam, and K. A. Shore, Opt. Lett. 24, 466, (1999).
[6] I. Fischer, Y. Liu, and P. Davis, Phys. Rev. A 62, 011801(1), (2000).
[7] A. Bogris, D. F. Kanakidis,. A. Argyris, and D. Syvridis, IEEE J. Quantum Electron. 40, 1326,(2004).
[8] S. Tang, and J. M. Liu, Opt. Lett. 26, 596, (2001).
[9] N. Gastaud, S. Poinsot, L. Larger, J. M. Merolla, M. Hanna, J. P. Goedgebuer, and E. Malassenet, Electron. Lett. 40, 898, (2004).
[10] F. Y. Lin,. and M. C. Tsai, Opt. Express 15, 302, (2007).
[11] V. Z. Tronciu, C. Mirasso, P. Colet, M. Hamacher, M. Benedetti, V. Vercesi, and V. Annovazzi-Lodi, IEEE J. Quantum Electron. 46, 1840, (2010).
[12] V. Z. Tronciu, C. Mirasso, and P. Colet, J. Phys. B: At. Mol. Opt. Phys. 41, 155401, (2008).
[13] V. Z. Tronciu, I.V. Ermakov, P. Colet, and C. Mirasso, Opt. Commun. 281, 4747, (2008).
[14] J. Ohtsubo, IEEE J. Quantum Electron. 38, 1141, (2002).
[15] G.D. VanWiggeren, and R. Roy Science 279, 1198, (1998).
[16] R. Lang, and K. Kobayashi, IEEE J. Quantum Electron. 16, 347, (1980).
[17] T. Perez, M. Radziunas, H.-J. Wünsche, C.R. Mirasso, and F. Henneberger, IEEE Photonics Technol. Lett. 18, 2135, (2006).
[18] A. Sanchez-Diaz, C. Mirasso, P. Colet, and P. Garcia-Fernandez, IEEE J. Quantum Electron. 35, 292, (1999).

COMPARISON OF CLASSICAL NUCLEATION THEORY AND MODERN THEORY OF PHASE TRANSITION IN THE CASE OF ELECTROCHEMICAL NUCLEATION

S. A. Baranov[1,2,3]

[1]*Institute of Applied Physics, Academy of Sciences of Moldova, str. Academiei 5, Chisinau, MD-2028 Republic of Moldova*
E-mail: oialt@mail.ru baranov@phys.asm.md kanarovskii@gmail.com
[2]*Departament de Genie Physique, Ecole Polytechnique de Montreal, C.P. 6079, succ. Centre-ville, Montreal H3C 3A7, (Quebec) Canada*
E-mail: sabaranov48@gmail.com
[3]*Shevchenko Transnistria State University, str. 25 Oktyabrya 128, Tiraspol, Republic of Moldova*
E-mail: sabaranov07@mail.ru

(Received November 11, 2016)

Abstract

Electrodeposition of nanostructures has been considered in terms of the classical Gibbs and the Cahn–Hilliard–Hillert theories. Agreement between the Cahn–Hilliard–Hillert and Gibbs theories has been obtained. Therefore, there is no contradiction between the Cahn–Hilliard–Hillert and Gibbs theories.

1. Introduction

Electrochemical nucleation is usually described in terms of the classical Gibbs theory, which provides a simple expression for the critical radius of growing nanoparticles [1–11]:

$$r_c = K(\gamma/\mu), \quad (1)$$

where σ is the specific surface energy, μ is the change in volume energy during a phase transition (e.g., nucleation), and K is the particle shape factor.

The kinetics of electrochemical reactions is determined by the energy barrier magnitude [5–9]. It is known that the steady flow rate of formation of the most probable nuclei is defined as follows [3–9]:

$$J \sim \exp\{-\Delta E_c / kT\}. \quad (2)$$

The dimensionless parameter [1–11]

$$G=\Delta E_c / kT,(3), \quad (2a)$$

which is referred to as the Gibbs number, describes, in particular, the equilibrium electrochemical nucleation.

Below, we will discuss methods for calculating ΔE_c, which is the free energy change ΔG in the process of nucleation, in terms of the Gibbs model and the model of the modern theory of phase transitions.

2. Classical Gibbs nucleation theory

Energy ΔE_c in the classical Gibbs nucleation theory (for a three-dimensional case) was obtained by assuming that the nucleus is a sphere of radius r [1–9]:

$$G_3 = G_{3P} - G_{3V} = 4\pi r^2 \gamma_3 - (4/3)\pi r^3 \mu_3 \tag{4}$$

The size of the critical radius of nucleation r_c is determined in (1):

$$r_c = 2\gamma/\mu \ .$$

Critical nucleus radius corresponding to maximum G_3 is as follows:

$$\Delta G_3 = (16\pi/3)(\gamma_3^{\ 3}/\mu_3^{\ 2}) \tag{5}$$

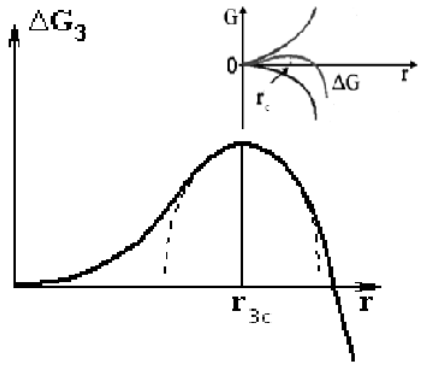

Fig. 1. Qualitative kind of free energy barrier. The cross-over of the bulk and surface terms combined with their opposing signs lead to the formation of a free energy barrier.

For a two-dimensional case, we obtain

$$G_2 = 2\pi r\ \gamma_2 - \pi r^2 \mu_2 \ ;$$

$$r_{2c} = k_2\ \gamma_2 \Big/ \mu_2 \ ,$$

where k_2=1;

$$\Delta G_2 = G_{2P}/2 = \pi(\gamma_2^{\ 2}/\mu_2) \tag{6}$$

The generalization can be obtained for a multidimensional system:

$$r_{nc} = (n-1)(\gamma_n / \mu_n) \ , \tag{7}$$

and

$$\Delta G_n = G_{nP} / n \tag{8}$$

According to (7), in a the one-dimensional case,

$$r_{1c} = 0 \tag{9}$$

because $k_1 = 0$.

This finding is consistent with the general theory. In terms of the droplet model, for convex surfaces, one can obtain the following expression:

$$k(i) \sim \frac{S'(r)r}{V'(r)} \tag{10}$$

To calculate energy barrier ΔG, it is necessary to know the surface energy and particle shape factor $k(i)$:

$$\Delta G_i \sim G_P / [k(i)+1] \tag{11}$$

Energy barrier ΔG can be assumed to be proportional to cathode overpotential η_k (see, e.g., [10, 11]). This dependence can be presented as follows:

$$\Delta G_n \sim 1/(\mu_n)^{n-1} \sim 1/(\eta_k)^{n-1} . \tag{12}$$

It was experimentally studied for the case of n = 2 and 3, which follows from Eqs. (8)–(12) (see, e.g., [11]).

Other general findings are given below. Here, we note that, if the short-range interaction covers the following focal areas, then radius r_{nc} increases to infinity, while the energy barrier vanishes.

It was found that, for spinodal disintegration, the radius r_{nc} increases indefinitely, while the energy barrier decreases.

3. Ginsburg–Landau–Abrikosov theory and Cahn–Hilliard theory applied to nucleation

The Ginsburg–Landau–Abrikosov theory uses free energy (Hamiltonian) in form [12–15]

$$H(\Sigma) = \alpha (\nabla\Sigma)^2 + A\,\Sigma^2 + C\,\Sigma^4 + \dots \ , \tag{13}$$

where order parameter Σ is a generalized spinor (linear term is omitted).

Function $H(\Sigma)$ extreme condition allows deriving a differential equation. This equation was obtained in [14, 15]:

$$\theta''(\rho) + ((L-1)/\rho)\,\theta'(\rho) - F[(a, \rho), \cos\{\theta(\rho)\}, \sin\{\theta(\rho)\}] = 0, \tag{14}$$

$$1/a = (\alpha / A)^{1/2} ,$$

where L determines the space dimensionality of spinor (nD-dimensionality), and $F[(a, \rho), \cos\{\theta(\rho)\}, \sin\{\theta(\rho)\}]$ is a polynomial (analytical function) that can be defined in each case.

Application of Eq (14) to a 2D problem was thoroughly considered in [15]. Below, we consider a 1D case (L = 1), which corresponds to the Cahn–Hilliard–Hillert theory.

The resulting equation has the form

$$\theta''(\rho) = (a/2)\sin\{2\theta(\rho)\} , \quad (15)$$

which is similar to previously reported equations [16–22] and according to which it is possible to obtain the solution [15]:

$$\cos\{\theta(\rho)\} = -\text{th}\{a\rho)\} , \quad (16)$$

Fig. 2. Schematic representation of the solution in the form of a domain wall of energy vectors.

The size of the domain wall is an important parameter determining the nucleating seed size:

$$\delta_{LL} = 1/a = (\alpha / A)^{1/2} \quad (17)$$

Assuming that the domain wall size determines the critical radius of a (nucleating) nanoparticle, the difference between Eqs. (1) and (17) should be noted.

It can be shown that the energy of the domain wall is also different from the classical formulas given by Eqs (5) and (8):

$$E_{LL} = (\alpha A)^{1/2} \quad (18)$$

Agreement between the Ginsburg–Landau–Abrikosov (Cahn–Hilliard–Hillert) theories and the classical Gibbs nucleation theory is discussed below.

4. Unification of the theories and conclusions

The simplest assumption regarding the relationship between the surface tension and the nanoparticle radius can be expressed as follows:

$$\gamma_{eff} \approx \gamma / r_{rel} , \tag{19}$$

$$\text{and} \quad r_{rel} = r_c / \Delta_{in} ,$$

where Δ_{in} is the thickness of the surface layer of the nanoparticle and $r_{rel} = r_c / \Delta_{in} > 1$ is a parameter of length characterizing the nanoparticle size in terms of Δ_{in}.

If $r_{rel} < 1$, then the Gibbs theory is not applicable. However, it can be applied in accordance with the Cahn–Hilliard–Hillert theory. In this case, a formula similar to (1) (or (7) without taking into account the k_n factor) can be written as follows:

$$r_c \approx \gamma_{eff} / \mu \approx \Delta_{in}\gamma / r_c\mu \tag{20}$$

It is not difficult to transit to the formulas in the form of (17) from the Cahn–Hilliard–Hillert theory:

$$r^{(KXX)}{}_c \approx \left(\Delta_{in}\gamma / \mu \right)^{1/2} , \tag{21}$$

if

$$K \to \Delta_{in}\sigma_{in} \equiv \Delta_{in}\gamma; \quad \mu \to G_{KXX} . \tag{22}$$

Thus, there is a correspondence between the Cahn–Hilliard–Hillert and Gibbs theories.

It is of interest to show that there is no contradiction between the formulas for the activation energy in the Cahn–Hilliard–Hillert and Gibbs theories.

In fact, the order of accuracy for activation energy is determined by the energy (barrier) necessary for merging particles, which is a product of the particle chemical potential (–μ) and the defect size (linear case implied) and can be estimated via Eq. (21).

Finally, it is not difficult to arrive at the following formula:

$$\Delta G \sim (\Delta_{in}\gamma\mu)^{1/2} \tag{23}$$

Therefore, there is no contradiction between the Cahn–Hilliard–Hillert and Gibbs theories.

References

[1] J. W. Gibbs, Graphical methods in the thermodynamics of fluids, Collected Works, Vol. 1, Yale Univ. Press, New Haven, 1928.
[2] Ja. I. Frenkel, J. Chem. Phys. 7, 200, (1939).
[3] Ja. I. Frenkel, Kinetic Theory of Liquids, Dover Publications, Inc., New York, 1955.
[4] J. B. Zeldovich, Acta Physicochim. URSS 18, 1, (1943).
[5] Yu. D. Gamburg and G. Zangari, Theory and Practice of Metal Electrodeposition, Springer, New York, 2011.
[6] M. Volmer and A. Weber, Z. Phys. Chem. (Leipzig) 119, 277, (1926).
[7] C. Z. Wagner, Electrochem. 65, 58,1 (1961).
[8] M. A. Anisimov, Critical Phenomena in Liquids and Crystals, Philadelphia, Gordon & Breach, 1991.
[9] F. F. Abraham, Homogeneous Nucleation Theory, Academic Press, New York and London, 1974.
[10] T. Erdey-Gruz and M.Z. Volmer, Phys. Chem. 157 A, 165, (1931).
[11] K. J. Vetter, Electrochemical Kinetics, Theoretical Aspects, Academic Press, New York, 1967.
[12] L. D. Landau, On the Theory of Phase Transitions 1, Phys. Zs. Sowjet 11, 26, (1937).
[13] L. D. Landau, On the Theory of Phase Transitions 2, Phys. Zs. Sowjet 11, 545, (1937).
[14] Shang-keng Ma, Modern Theory of Critical Phenomena, Ed. W.A. Benjamin, Massachusetts Inc. Advanced Book Program Reading, 1976.
[15] S. A. Baranov, Handbook of Nanoelectrochemistry: Electrochemical Synthesis Methods, Properties and Characterization Techniques, Springer, Switzerland, 1057, 2015.
[16] J. W. Cahn and J.E. Hilliard, J. Chem Phys. 28 (2), 258, (1958).
[17] J. W. Cahn and J.E. Hilliard, J. Chem Phys. 30 (5), 1121, (1959).
[18] J. W. Cahn and J.E. Hilliard, J. Chem Phys. 30 (5), 688, (1959).
[19] J. W. Cahn, Trans. Met. Soc. AIME 242, 166, (1968).
[20] J. W. Cahn and F.C. Larche, Acta Met. 30, 51, (1982).
[21] M. Hillert, Metall. Trans. 6A, 1, 5, (1975).
[22] A. G. Khachaturyan, Theory of Structural Transformations in Solids, Wiley, New York, 1983.

ON THE 90TH ANNIVERSARY OF ACADEMICIAN SERGIU RADAUTSAN

1926—1998

The role of Academician Sergiu Radautsan in the history of physics in Moldova, semiconductor physics to be exact, is hard to be overestimated.

S. Radautsan was born on 17 June 1926, to a family of teachers Ion and Nina Radautsan. His father was a teacher of French and spoke 9 languages, his mother was a Conservatoire graduate. His education started in Cishinau (B.P. Hasdeu high school, then Moldova State University, faculty of physics). An important and significant fact was his doctoral course in Chisinau first, under the guidance of Prof. M.V. Kot, the Head of the Experimental Physics Department in the 1950s, who initiated a research into the physics and chemistry of semiconductor materials at the State University. A bit later, future academician left for St. Petersburg (Leningrad at that time), to continue his PhD course at the A.I. Ioffe Physical-technical Institute (LFTI). There, under the guidance of Prof. N.A. Goryunova he came to investigate semiconductor materials with intrinsic defects and defended his PhD thesis

"Investigation of solid-solutions on the base of indium-arsenide".

Returning to Chisinau in 1959 after obtaining the PhD degree at LFTI, he set up the Laboratory of Semiconductor Compounds, the Head of which he was for the rest of his life. In 1964, after the organization of the Institute of Applied Physics, the laboratory became a part of the Institute and is now bearing his name: Laboratory of Physics of Semiconductors "Sergiu Radauțan". For many years the principal direction of this laboratory was the synthesis and study of multicomponent semiconductor compounds. From these moments one can say that in the Moldovan semiconductor physics a new period began– the Radautsan period. Now the collaborators of this lab deal with: elaboration of the technology of obtaining of ternary and multinary compounds. Experimental and theoretical studies of the physics and physical chemistry of the obtained compounds as well as of the magnetic, optical and luminescent properties; experimental and theoretical studies in the field of obtaining thin semiconductor films; elaboration of multifunctional electronic, optoelectronic and photonic devices on their basis, elaboration of advanced technologies.

From 1961 till his last days he was a prolific researcher at the Institute of Applied Physics of the Academy of Sciences of Moldova. In 2016, the Institute in collaboration with Moldova State University organized the 8^{th} International Conference on Materials Science and Condensed Matter Physics dedicated to the 70^{th} anniversary of foundation of first research institutions of the ASM, the 55^{th} anniversary of the inauguration of the Academy of Sciences of Moldova, the 70^{th} anniversary of Moldova State University and the 90^{th} anniversary of academician S. Radautsan**.** He also was the initiator of the foundation of Polytechnic Institute in Chisinau (Technical University nowadays) whose first rector he was in 1964—1973. On 17 June 2016, the Technical University organized a Conference to commemorate its first rector: „In memoriam: Academician Sergiu Radautsan – 90^{th} anniversary".

In 1969 a self-financed Microelectronics Laboratory was set up at the Polytechnic Institute. The laboratory worked directly with the LFTI, with the laboratory headed by Academician Zhores Alferov, a Nobel laureate. The studies carried out in micro- and optoelectronics, in the technology of the design and manufacture of semiconductor lasers, as well as in several other areas were highly appreciated internationally. The high level of the research into semiconductors was influenced also by the fact that some of the outstanding experts from all over the Soviet Union, among them Nina Goryunova and Dmitry Nasledov, used to come to Chisinau to deliver lectures on most advanced topics.

Academician Radautsan, together with his disciples and colleagues, developed a technology of obtaining many various ternary semiconducting compounds, that have a wide range of optical, electrical and radiative properties, which is important from both theoretical and practical purposes. He and his team found a new class of ternary compounds of spinel type like $CdCr_2S_4$ that have the properties of magnetic semiconductors. His scientific results are reflected in over 900 publications. Among them books: Арсенид и фосфид кадмия (1976, in collaboration); Полупроводники системы ZnS-In_2S_3 (1980, in collaboration); Магнитные полупроводники на основе селенхромита меди (1984, in collaboration); Многокомпонентные халькогениды $A^{II}B_2^{III}C_4^{VI}$ (1990, Ed.); Scientific and technological achievements related to the development of European cities (1997, Co-Ed.); etc. (List of his publications can be found on: http://www.radautan.info/). He had 120 patents to his credit. He

was the supervisor and scientific consultant of 60 doctors and 12 doctors habilitate. Academician Radautsan was an active participant of over 200 national and international scientific gatherings in different countries. He was Invited professor at the Universities (respective faculties) in Europe, Asia, the USA and Canada.

When the Republic of Moldova became a sovereign state, Academician Radautsan was elected vice-president of the Academy of Sciences of Moldova, then an Honorary Member of the Romanian Academy of Sciences, of the Russian Academy of Engineering Sciences, of the International "K. Tsiolkovsky" Astronautics Academy, of the Central European Academy of Sciences and Arts. He was Doctor Honoris Causa of the West University (Timisoara, Romania), Transylvania University (Brasov, Romania), Al. I. Cuza University (Iasi, Romania), the Technical University (former Polytechnic) and the Academy of Economic Studies (both Chisinau, Moldova).

He was also the initiator of several important scientific events. For instance: the 8th International Conference on Ternary and Multinary Compounds (ICTMC-8) in 1990; the biennial Summer Conferences on Ternary and Multinary Semiconductors. Those latter science workshops were attracting specialists from the whole Soviet Union. They contributed a lot to the development of physics in Moldova. On an initiative of Acad. Radautsan, Chisinau had the honor to host a NATO Advanced Workshop on "Scientific and Technological Achievements Related to Big Cities". That workshop gathered experts from Europe, the USA, newly independent states from the former USSR. The workshop took place in 1996, just a month before Acad. Radautsan's 70th birthday. Unfortunately it was the last scientific event organized by him.

The honors were all well-deserved. Academician Sergiu Radautsan became one of the Moldovans well-known abroad; he was deeply respected by his Western colleagues, and not only scientists. On the other hand, the period of transition to the market economy proved to be hard for many areas of life, including science and research in Moldova. Even in that difficult period Academician Radautsan was trying, very often succeeding, to find opportunities to support Moldovan science and maintain its potential. The first Rector of the Polytechnic Institute was fully aware of the necessity to integrate the research at specialized centers and universities with teaching. He was pulling efforts to draw the attention of the governance to the importance of scientific research and of good education. The lifelong achievements of Academician Sergiu Radautsan were recognized by the State. He was the holder of the title the Emeritus Person, of the Order of the Republic, the highest distinction in Moldova, as well as of other honorific awards. In 1983 and 1998 he was named State Prize Laureate, the second time posthumous. Academician Sergiu Radautsan was a well-known physicist, a person of character and charisma, an administrator of a high level.

The obituary "In memory of Sergeĭ Ivanovich Radautsan" was signed by famous scientists: Alferov, Z.I., Gulyaev, Y.V., Keldysh, L.M., Kuznetsov, F.A., Prokhorov, A.M., Perel, V.I., Veselago, V.G., Gurevich, A.G., Prochukhan, V.D., Ivanov-Omskii, V.I. and published in *Semiconductors*, Volume 32, Issue 11, November 1998, pp.1253-1254.

Dr. Olga Iliaşenco,
Acad. Leonid Culiuc,
Institute of Applied Physics,
Academy of Sciences of Moldova,

ON THE OCCASION OF THE 85TH ANNIVERSARY OF ACADEMICIAN DUMITRU GITSU

13.01.1931–23.11.2008

Scientists who have dedicated their lives to research and education rarely are the focus of attention of mass media or the public at large even when they are alive and do their duty with honor. We only hear about them on the occasion of commemorations, although their contribution to society development is extremely valuable. Those who have entered the world of the righteous are called to our minds even more rarely. Academician Dumitru Gitsu is one of them. In 2016 the late scholar physicist would have turned 85 years old. He was totally dedicated to science during his life and may be thought of as having an outstanding personality. It is not for nothing that in ancient times they said that science and art make a man of integrity! He certainly was one of the personalities who have founded research in physics and engineering in Moldova in terms of content and institutional aspects. He left behind a valuable scientific work, which still is the issue of the day in the development of research and remains in the international circuit; a good many researchers continue to develop some of the ideas launched by acad. D. Gitsu.

He was born on January 13, 1931 in village Drepcauti, Briceni district, R.Moldova. After graduating from Kishinev State University (now State University of Moldova) in 1954, he worked as a teacher at the State Universities of Balti and Tiraspol, then at Kishinev State University. In the late 1950s, he did postgraduate studies at the Pedagogical University in

Leningrad (now St. Petersburg); in 1961 he successfully defended his candidate' dissertation in physics and mathematics entitled “Anisotropy of galvanomagnetic properties of bismuth single crystals and its alloys”.

Academician Dumitru Gitsu belonged to the lucky post-war generation of physicists who benefited from excellent conditions of study in research centers in Moscow, Leningrad, Novosibirsk, Kiev, etc. In those centers of excellence, there was formed a class of highly skilled specialists involved in a severe international scientific competition resulting in discoveries in the field of modern physics. They alive wrote the history of contemporary science in the second half of the twentieth century.

In 1961–2008, Dumitru Gitsu worked at the Academy of Sciences of Moldova; at the Institute of Applied Physics, he held the following positions: junior research assistant, founder and head of the Laboratory for physics of semimetals, and deputy director. After that, he was general scientific secretary of the Presidium of the Academy of Sciences of Moldova, scientific coordinator of the Department of Physics and Mathematics, director of the Center "International Laboratory of Superconductivity and Solid State Electronics," director of the Specialized Bureau in the field of solid state electronics, and founder and director of the Institute of Electronic Engineering and Industrial Technologies (now Institute of Electronic Engineering and Nanotechnologies). This institute is named after acad. Gitsu, and rightly so, because he was like Master Manole, who walled his wife up at the Curtea de Arges Monastery and lived for the sake of science within the walls of the Institute for many decades.

Lifelong, acad. Gitsu worked with the conviction "that “Quiconque ne sait pas souffrir, n'a point un grand cœur. Il faut, par votre patience et votre courage, lasser la cruelle fortune, qui se plaît à nous persécuter”(Fr. Fenelon).

Being fully endowed with a genius of researcher and a huge capacity for work, acad. Gitsu enormously succeeded for more than 50 years of his creative activities in science. Scientific interests of acad. Gitsu involved a variety of fields, such as physics and technology of semimetals and semiconductors, physics and technology of anisotropic materials, physics of low-dimensional systems, and engineering of electronic and medical devices. Physicist Dumitru Gitsu has left a deep furrow in science: together with his disciples, he has developed a phenomenological and microscopic theory of galvanothermomagnetic processes in bismuth type semimetals, experimentally discovered the phenomenon of magnetic flux quantization in submicron bismuth wires, and, on the basis of promoted research, developed and implemented a number of transducers, sensors, and devices for various purposes. He has founded a scientific school in physics of semimetals and narrow band semiconductors.

In addition, acad. Gistru has gone down in the history of science owing to some bridges of cooperation established with several research centers in a variety of countries in the world. The research activities have been hoarded in a vast scientific work: more than 500 scientific papers (mostly in prestigious international scientific journals) and 2 monographs have been published; about 25 patents have been obtained. Acad. Dumitru Gitsu was a true man of creative work which, in the words of Lucian Blaga, is like "to gather dew-drops from the grass and sweat of nightingales who worked all night singing."

Being a wise teacher of new generations of physicists, he has trained over 35 doctors of science, six of which have become doctors hability. It is this intellectual potential of acad. Gitsu that was used to found and develop a scientific school of excellence and organize a research center for studying the transport phenomena and electrophysical properties in solid state, which is recognized and appreciated worldwide. As part of this center, multiple international collaborations have been developed and crystallized into a large number of international projects.

Goethe said, "We learn only from those whom we love." Acad. Dumitru Gitsu was loved by all those with whom he worked. In particular, acad. Gitsu was involved in vast activities on institutional development of the Academy of Sciences of Moldova proficiently combining the scientific and teaching activities with management.

He was the initiator of organization of a Center for design and technology in the field of solid state electronics at the Academy of Sciences. On the basis of this Center, the Center for automation and metrology, the Center for the construction of biological equipment, and the Tehmed Center were organized. Acad. Gitsu was the initiator of organization of the Cryogenic Center, which was used as a base for the beginning of systematic experimental low-temperature research in Chisinau. His latest activities on institutional organization in the Academy of Sciences was the foundation of the Institute of Electronic Engineering and Industrial Technologies in 2006; it was organized through the fusion of three scientific centers—International Laboratory of Superconductivity and Solid-State Electronics, Specialized Bureau in the field of solid state electronics, and Tehmed. Acad. Gitsu spent his life in the real and virtual walls of this institute.

In the 1990s, after the collapse of the USSR, acad. Gitsu understood the essence of changes in the region and prepared a Concept of organizing a science and technology park based on research institutes and the TOPAZ plant with broad participation of universities. In those times, it was a bold forward-looking project, perhaps an attempt to break the monotonous flow of time. Unfortunately, the decision makers of those times did not give the green light to the elaborated project, which, in fact, was meant to preserve and strengthen the connecting link between the world of research and the real sector. As a result, we lost about 12 years and returned to the organization of similar structures only in 2007 after the adoption of the law on science and technology parks and innovation incubators.

His significant contribution to science and research organization has been recognized by awards and honorary titles at the national level. In 1976, D. Gitsu was elected an associate member; in 1984, full member of the Academy of Sciences of Moldova. He was decorated with an "Order of the Republic" and honored with other state awards. He was awarded the title of Emeritus in science and became a laureate of the State Prize in Science and Technology. In this context, let us mention some international titles and honorary distinctions of acad. Dumitru Gitsu, such as honorary member of the Russian Academy of Cosmonautics named after Tsiolkovsky, member of the International Academy of Thermoelectricity, and Doctor Honoris Causa of three Universities in Romania and Moldova. He was a member of the International Editorial Board of the journal "Thermoelectricity."

Physicist academician Dumitru Gitsu died on November 23, 2008. He always expressed great confidence towards his colleagues. He rightfully believed that only true scholars and honest people can accomplish things that will endure over time. Genuine scientist, kind-hearted man Dumitru Ghiţu will remain in scientific Annals, in the history of research in the country, and also in the memory of those who worked with him and received his generous advice in every situation; he was a true guide and friend. Let us remember this great man of the nation with gratitude, while keeping his memory alive.

Academician V. Kantser
Academician I. Tighineanu
Associate member A. Sidorenko

CONTENTS

Bulk Materials

V. M. Thanh, D. P. Kozlenko, D. Sangaa, S. E. Kichanov, E. V. Lukin, L. H. Khiem, L. Nyam-Ochir, O. Gerelmaa, B. N. Savenko
THE NEUTRON DIFFRACTION STUDIES OF A CRYSTAL STRUCTURE OF $NaFe(W_xMo_{1-x}O_4)_2$ (x = 0.5; 0.75) AT LOW TEMPERATURE…….119

L. Prodan
SYNTHESIS, CRYSTAL STRUCTURE, AND MAGNETIC PROPERTIES OF $MnCr_2S_4$ SPINEL… 125

D. Croitori
GROWTH OF FeTe SINGLE CRYSTALS AND INVESTIGATION OF THEIR STRUCTURE AND MAGNETIC PROPERTIES……...130

D. Meglei and S. Alekseeva
EXPERIMENTAL AND THEORETICAL TEMPERATURE DEPENDENCES OF THE KINETIC COEFFICIENTS OF $Pb_{0.82}Sn_{0.18}Te$……134

Nanostructures and Nanomaterials

O. Lupan, V. Postica, V. Cretu, T. Pauporte, and R. Adelung
SERIES AND PARALLEL CONNECTION OF INDIVIDUAL Pd-MODIFIED ZnO NANOWIRES FOR GAS SENSING APPLICATIONS…….139

V. V. Sergentu, V. Prilepov, V. Zalamai, and P. Gashin
WATER AS A NANOSTRUCTURED MATERIAL……..150

E. Rusu, V. Postolache, N. Curmei, and V. Ursaki
A COMPARATIVE STUDY OF PHOTOCONDUCTIVITY DECAY IN ZnO-BASED MSM STRUCTURES AND NANOWIRES……158

A. Burlacu
CONTROL OF MORPHOLOGY AND LUMINESCENSE OF NANOSTRUCTURED ZnO LAYERS FOR LASING APPLICATIONS…….164

V. Postolache
LUMINESCENCE OF POROUS SEMICONDUCTOR MEDIA COVERED WITH METALLIC FILMS…….176

V. Postolache
A COMPARATIVE STUDY OF PHOTOCONDUCTIVITY DECAY IN GRANULAR AND NANOWIRE ZnO……...184

Materials Crystal Structure

E. Melnic
STACKING INTERACTIONS IN THE CRYSTAL STRUCTURES OF MIXED LIGAND SQUARE-PYRAMIDAL COPPER(II) COMPLEXES WITH AROMATIC 1,10-PHENANTHROLINE OR 2,2´-BIPYRIDINE LIGANDS AND ACETYLACETONATE……..193

Technologies and Device Physics

N. Ciobanu, S. S. Rusu, and V. Z. Tronciu
SYNCHRONIZATION AND OPTICAL COMMUNICATIONS BY THE CHAOS MODULATION TECHNIQUE USING QUANTUM DOT LASERS WITH T-TYPE OPTICAL FEEDBACK……...208

S. S. Rusu[1,2] and V. Z. Tronciu[2]
DYNAMICS OF A SEMICONDUCTOR LASER UNDER THE INFLUENCE OF MULTI-SECTION FEEDBACK: APPLICATIONS TO CHAOS-BASED COMMUNICATIONS…….215

S. A. Baranov
COMPARISON OF CLASSICAL NUCLEATION THEORY AND MODERN THEORY OF PHASE TRANSITION IN THE CASE OF ELECTROCHEMICAL NUCLEATION…….225

Events and Personalia

ON THE 90TH ANNIVERSARY OF ACADEMICIAN SERGIU RADAUTSAN…….231

ON THE OCCASION OF THE 85TH ANNIVERSARY OF ACADEMICIAN DUMITRU GITSU…….234